

**UNIVERSITÀ DEGLI STUDI DI NAPOLI  
FEDERICO II**



**DOTTORATO DI RICERCA IN  
FISICA**

Ciclo **XXXIII**

Coordinatore: prof. Salvatore Capozziello

**Vector Field Patterning of Light: Methods  
and Applications**

Settore Scientifico Disciplinare FIS/03

**Dottorando**

**PEGAH DARVEHI**

**Tutori**

**PROF. LORENZO MARRUCCI**

Anni **2018/2021**

# Acknowledgements

At the end of my doctoral project, I would like to take this opportunity to thank all of the people who helped me conduct my research. First of all, I would like to thank my supervisor, **prof. Lorenzo Marrucci**, who accepted me into the group and for his valuable suggestions and feedback on my work. I would like to thank **prof. Bruno Piccirillo** for letting me work with him in his lab on his interesting research topic. I would also like to thank all my colleagues in SLAM group. Especially, I thank **Raouf Barboza**, from whom I received a lot of support and help to understand the theory behind my work. I also thank Amin Babazadeh for the support and suggestions on my work and Veronica Vicuna for her help in my experimental activities in the lab. I wish to thank **Mr. Guido Celentano** for his patience, kindness, and helping me in official bureaucracies. Finally, I thank all my friends and family who supported me during these years.

# Abstract

Light (electromagnetic field in general) is a main form of energy in nature. Thanks to centuries of scientific investigations, we nowadays possess a fairly complete knowledge of its properties and behavior. In particular, conserved quantities, such as energy and momentum of light, have been the subject of experimental and theoretical activities leading to a great advancement of science and technology. The momentum of light can be distinguished in two different kinds, that is, linear momentum and angular momentum. The main focus of this work is on the angular momentum of light and its manipulation in order to control the vectorial pattern of the light field.

The angular momentum of the electromagnetic field expresses two different forms of rotation called spin angular momentum and orbital angular momentum. We focus on the cases in which these two rotations can be considered independent. The first is related to the state of the polarization, and the second to the spatial distribution of the beam. Since they are independent, each of these two rotations can be studied separately and used in different applications. The interaction between them, however, attracts great attention, since a beam may possess both at the same time. The device called q-plate is one possible technique which results in spin-orbit coupling.

In this work, we present the importance of the interaction of spin and orbital angular momentum for certain applications. For this purpose, we have designed devices (e.g., q-plates) that combine both forms of angular momentum. This thesis consists of four chapters as follows:

- Chapter 1: In this chapter, we give an introduction about light angular momentum, in particular orbital angular momentum. Various methods

for generating helical modes, in particular q-plates, are discussed.

- Chapter 2: In this chapter, we discuss the optical fibers and the coupling efficiency in the fundamental mode of a single-mode step-index fiber. The main focus of this chapter is on amplitude matching to increase the coupling efficiency.
- Chapter 3: Reaching the highest possible coupling efficiency cannot be achieved by amplitude matching alone. Another important factor is polarization matching, which is the interest of this chapter. We present a novel application for q plates to improve the coupling efficiency by manipulating the polarization structure of the input beam.
- Chapter 4: In this last chapter, we investigate the possibility of beam tailoring and polarization singularity generation using Spatially Varying Axes retardation wave Plates (SVAPs), devices which generalize the q-plates.

Finally, we conclude this work by presenting the results and possible prospects for future work.

# Contents

<b>Acknowledgements</b>	<b>i</b>
<b>Abstract</b>	<b>iii</b>
<b>1 Spin and Orbital Angular Momentum of Light</b>	<b>1</b>
1.1 Introduction . . . . .	1
1.2 Light's angular momentum . . . . .	2
1.3 Electromagnetic field in paraxial approximation . . . . .	6
1.3.1 Gaussian modes . . . . .	9
1.3.2 Polarization of light and SAM . . . . .	9
1.3.3 Orbital angular momentum of light and phase singularity	14
1.3.4 Tools to manipulate and control OAM of light . . . . .	16
<b>2 Improved Scalar Mode Matching</b>	<b>26</b>
2.1 Introduction . . . . .	26
2.1.1 Optical fiber history . . . . .	27
2.1.2 Optical Fibers Classifications . . . . .	28
2.2 Optical Fiber Modes . . . . .	30
2.2.1 Vectorial structure of the optical fiber modes . . . . .	33
2.2.2 Nanofibers . . . . .	35
2.3 Beam coupling . . . . .	37
2.3.1 Scalar mode matching . . . . .	39
2.3.2 Improved scalar mode matching . . . . .	42

---

<b>3</b>	<b>Vectorial Mode Matching</b>	<b>45</b>
3.1	Introduction . . . . .	45
3.2	Generation of light carrying OAM in optical fibers . . . . .	46
3.2.1	Applying pressure . . . . .	47
3.2.2	Bending the fiber . . . . .	48
3.2.3	Applying acousto-optic interaction . . . . .	49
3.3	Literature review of increasing coupling efficiency into optical fibers . . . . .	50
3.4	Polarization manipulation via q-plate . . . . .	51
3.4.1	Fiber Mode synthesis with a geometric phase plate . . . . .	52
3.5	Paraxial approximation validation . . . . .	60
<b>4</b>	<b>Modulated Poincare Beams</b>	<b>63</b>
4.1	Introduction . . . . .	63
4.2	Phase singularity and polarization singularity . . . . .	65
4.2.1	Conversion between lemon and star . . . . .	68
4.3	Techniques to generate polarization singularity of light . . . . .	69
4.4	Generation of light beam with singularities using SVAPs . . . . .	72
4.4.1	modulated Poincaré beams . . . . .	76
4.5	A Free Form Azimuthal SVAP to generate modulated Poincaré beam . . . . .	77
4.6	detection and characterization of polarization singularities . . . . .	78
	<b>Conclusion</b>	<b>91</b>
	<b>Bibliography</b>	<b>102</b>

# Chapter 1

## Spin and Orbital Angular Momentum of Light

### 1.1 Introduction

As one of our most significant and fundamental forms of energy, light (visible light) makes things visible for us. Almost all creatures on Earth need light to continue their lives and it is indeed impossible to imagine the universe without it. Human's eyes are our tool to sense the (visible) light, while we can also feel its heat with our skin. In general, light sensing is different for each creature. One can see different ranges of its frequency and others can sense its properties such as polarization. Therefore, it is important for scientists to understand the light behavior and its characteristics to have a deep realization of the universe. Human attempts during the years results in the generation of artificial light, too. Maybe we can consider fire as the very first one made by humans. However, the invention of laser in 1960 provided a coherent source of light in the laboratories. Since then, manipulation and characterization of light beams are the center of various researches. Thanks to these activities, our knowledge regarding light (in general electromagnetic field) has enriched to the level that it has been applied in a wide range of applications from science, military, medicine to decoration and art. Energy and momenta of light, which can be linear and angular, are two main features of light that are the base of

the mentioned applications as they can be transferred to the matter [1, 2].

Among all the studies regarding electromagnetic fields, light tailoring and wavefront shaping are of huge attention due to their plenty of applications in science and industries. Therefore, we focused on studying this subject and some results are presented in the next chapters of this thesis.

Twisted beam which is our main tool to proceed with our research is described in this chapter. To start with, we introduce the momenta (linear and angular) of the electromagnetic field in the paraxial approximation. We will continue with explaining spin and orbital angular momentum, two distinct forms of angular momentum. The spin angular momentum (SAM) is linked to the polarization of light and orbital angular momentum (OAM) is associated with the wavefront of the beam. We see that in paraxial approximation, each of them can be considered as an independent degree of freedom and result in a form of rotation of the optical field. The first one defines a two-dimensional space while the second spans an infinite-dimensional of degree of freedom (due to their features). This infinite-dimensional degree of freedom makes OAM an outstanding choice to be exploited in many applications ranging from telecommunication, astrophysics, quantum optics to light-matter interaction and biology. Therefore, we also talk about the tools and techniques to generate and manipulate such beams. We talk about applying light carrying OAM for applications, generating and manipulating (which is the main object of this thesis) it in the following chapters.

## 1.2 Light's angular momentum

Now, we know that light is a form of electromagnetic field which encompasses two orthogonal electric and magnetic fields. The two fields lie in a transverse plane perpendicular to the beam propagation direction [3]. But, as mentioned the curious essence of humans leads us to our understanding of our surrounding nature, and maybe lightning was one of the first experiences of human about electricity with no scientific reason to explain it. Through the centuries,



scientists' collaborations to improve our knowledge and expand science lead to our modern understanding of electromagnetic fields. It can be claimed that Maxwell put all the work done by his previous scientists together and improved the theory of electromagnetic fields in four mathematical equations as in equations. 1.1. According to his theory, an electromagnetic field is composed of orthogonal electric and magnetic fields that travel into space at speed of  $c$ , the speed of light in vacuum which is about  $3 \times 10^8$  m/s. [3].

$$\nabla \cdot \mathbf{D} = \rho, \quad (1.1a)$$

$$\nabla \cdot \mathbf{H} = 0, \quad (1.1b)$$

$$\nabla \times \mathbf{E} = - \frac{\partial \mathbf{B}}{\partial t}, \quad (1.1c)$$

$$\nabla \times \mathbf{H} = \mathbf{J} + \frac{\partial \mathbf{D}}{\partial t}, \quad (1.1d)$$

where  $\mathbf{E}$  and  $\mathbf{B}$  are the electric, magnetic fields, respectively.  $\mathbf{D}$  is the electric displacement and  $\mathbf{H}$  is called the magnetic field strength.  $\rho$  shows the free electric charge density and  $\mathbf{J}$  is the free current density. For perfect isotropic dielectrics, the relationships between  $\mathbf{E}$ ,  $\mathbf{D}$ ,  $\mathbf{B}$ , and  $\mathbf{H}$  are  $\mathbf{D} = \epsilon \mathbf{E}$  and  $\mathbf{B} = \mu \mathbf{H}$ .  $\epsilon$  and  $\mu$  stand for electric and magnetic permittivity, respectively. From Maxwell's equations, one can deduce the "wave equation" as in 1.2 for an electromagnetic field to describe its propagation [3].

$$\nabla^2 \mathbf{E} - \frac{1}{c^2} \frac{\partial^2 \mathbf{E}}{\partial t^2} = 0, \quad (1.2a)$$

$$\nabla^2 \mathbf{B} - \frac{1}{c^2} \frac{\partial^2 \mathbf{B}}{\partial t^2} = 0. \quad (1.2b)$$

This theory is still the basis of our researches, and using it one can describe properties of an electromagnetic field such as its "rotation" which is represented by the vector quantity angular momentum.

It has been known that photons, as well as particles, carry energy and linear momentum. In order to describe energy and momenta density of an electromagnetic field in terms of  $\mathbf{E}$  and  $\mathbf{B}$ , one needs to solve the above equations together with Maxwell's equations. From theoretical point of view, it was also

demonstrated that these two quantities are related to each other. The rotational equivalent of this linear momentum is called angular momentum which is an important quantity, as well. In classical physics linear momentum per unit volume is equal to  $\mathbf{E} \times \mathbf{H}$  while it is  $\hbar\mathbf{k}$  per photon in quantum. Angular momentum is also linked to its linear counterpart by  $\mathbf{r} \times \langle \mathbf{E} \times \mathbf{H} \rangle$ , classically and  $\mathbf{r} \times \hbar\mathbf{k}$  in quantum. The angular momentum itself is made of spin and orbital angular momentum and each one is related to a different kind of rotation [4]. To make it more clear, let us consider the Earth. We know that Earth has two rotational movements, one around its own axis which creates days and nights and the other around an imaginary orbit around the Sun. It takes one year for the Earth to rotate around the Sun. The same rotational movements appear in a light beam which can be recognized by transferring it to the matters. Fig. 1.1 shows the difference between spin and orbital angular momentum of light. In general, one can transfer both spin and orbital angular momentum to a particle, simultaneously. In this case, the particle experience both kinds of rotation at the same time [5].

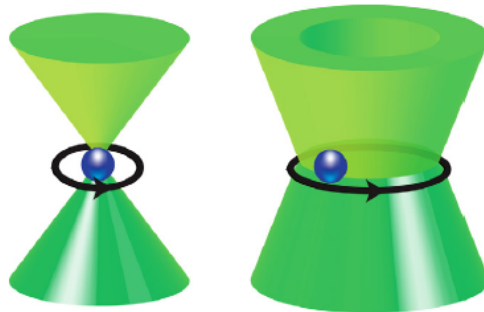


**Figure 1.1:** Light-matter interaction in optical tweezers. It shows the rotation of an absorbing particle around a) its own axis after receiving light with spin angular momentum, and b) the beam axis by transferring orbital angular momentum of light to it. The image is adapted from [1] which shows the particle trapping in optical tweezers.

In fact, history of spin angular momentum (SAM) of light returns to 1909 when Poynting prognosticated the ratio between angular momentum and energy of a circularly polarized beam. He considered the angular momentum of a beam with circular polarization is  $\pm\hbar$  [6]. Years later in 1936, Beth experimentally demonstrated when a circularly polarized light passes through a half

wave plate (HWP), it can transfer its angular momentum to the HWP and hence transform to a circularly polarized beam with opposite handedness [7]. Now, we know the SAM of light is the angular momentum carried by circularly polarized beam.

In general, the spin angular momentum of a beam is  $j_z = N\sigma\hbar$  while its energy is  $W = N\hbar\omega$ , where  $-1 \leq \sigma \leq 1$  and  $N$  represents the number of photons in the beam. Therefore, as Poynting suggested, the ratio between them is written as:

$$\frac{j_z}{W} = \frac{\sigma}{\omega}. \quad (1.3)$$

For a single photon the value of  $\sigma$  is  $+1$  ( $-1$ ) for left handed circular polarization (right handed). It is worth mentioning that this quantity is zero for a linearly polarized light. The idea of orbital angular momentum was introduced years later and is associated to spatial distribution of light.

In 1992, Allen et al. experimentally proved that a light beam with an azimuthal phase dependence  $\exp(im\phi)$  carries orbital angular momentum equal to  $\pm m\hbar$  per photon where  $\phi$  is azimuthal coordinate in the beam's cross section [8]. Interestingly, both SAM and OAM are integer multiple of  $\hbar$ . However, OAM can be considerably greater than SAM of light as  $m$  can take any integer number [9]. But historically, the origin of this concept backs to at least 1950 when higher order transitions like quadrupole carry both SAM and OAM. However, this OAM was considered very rare. In fact, the importance of Allen et al. experiment was that the OAM of light can be easily generated in the laboratories just by adding a proper phase factor to the beam wavefront. Although beams with helical phase front, vortices [10] and phase singularities were studied before 1992, they were not associated to the angular momentum of light [9].

The angular momentum of an electromagnetic field can be expressed as:

$$\mathbf{J} = \epsilon_0 \int \mathbf{r} \times (\mathbf{E} \times \mathbf{B}) d^3\mathbf{r}, \quad (1.4)$$

where  $\epsilon_0$  is the permittivity of the vacuum. Let us consider we have a monochromatic wave with frequency  $\omega$ ,  $\mathbf{E} = \mathbf{E}(\mathbf{r})e^{i\omega t}$ . Applying Maxwell's equations

and equation 1.4 shows that:

$$\mathbf{J} = \frac{\epsilon_0}{2i\omega} \int E_j^* (\mathbf{r} \times \nabla) E_j d^3\mathbf{r} + \frac{\epsilon_0}{2i\omega} \int \mathbf{E}^* \times \mathbf{E} d^3\mathbf{r} \quad (1.5)$$

where  $j = x, y, z$ . Equation 1.5 consists of two terms which can be interpreted as spin (first term) and orbital (second term) angular momentum. Therefore

$$\mathbf{J} = \mathbf{S} + \mathbf{L}, \quad (1.6)$$

where  $\mathbf{L}$  and  $\mathbf{S}$  represent orbital and spin angular momentum, respectively. Starting from the discovery of the two light angular momenta, there have been a lot of investigations to clarify whether these two quantities of light are separable, while still maintaining a distinct physical meaning. However, under the constraints needed for the paraxial approximation, one can safely separate SAM and OAM of light [4]. We do not address here the case where this separation loses its validity. Therefore, the paraxial approximation for electromagnetic fields will be discussed in the next section.

### 1.3 Electromagnetic field in paraxial approximation

It is common to determine electromagnetic field and hence Maxwell's equations in terms of a vector and scalar potential represented by  $\mathbf{A}$  and  $\phi$ , respectively as below:

$$\mathbf{B} = \nabla \times \mathbf{A}, \quad (1.7a)$$

$$\mathbf{E} = -\nabla\phi - \frac{\partial\mathbf{A}}{\partial t}. \quad (1.7b)$$

One can also simply recover the wave equation for the vector potential  $\mathbf{A}$ .

$$(\nabla^2 - \frac{1}{c^2} \frac{\partial^2}{\partial t^2})\mathbf{A} = 0. \quad (1.8)$$

Assuming the time dependence of  $\mathbf{A}$  is  $e^{i\omega t}$  and  $k^2 = \omega^2/c^2$ :

$$\nabla^2 \mathbf{A} + k^2 \mathbf{A} = 0. \quad (1.9)$$

In the scalar field approximation, one can express any electric field amplitude distribution with superposition of plane waves. A typical plane wave can be described by  $\mathbf{A} = A_0 e^{-i\mathbf{k}\cdot\mathbf{r}} \hat{\mathbf{n}}$ , where  $\hat{\mathbf{n}}$  is the unit vector along the direction of electric field fluctuation and  $\mathbf{k}$  is the wave vector. According to Maxwell's equation, electric and magnetic fields oscillate in the transverse plane which is perpendicular to the propagation direction. It implies that  $\hat{\mathbf{n}}\cdot\mathbf{k} = 0$ . As we want our solution to satisfy the equations 1.21:

$$\mathbf{A}(x, y, z, t) = \mathbf{A}(x, y, z) e^{i(kz - \omega t)}. \quad (1.10)$$

Here we considered just forward propagated beam. substituting equation 1.10 into 1.9 give us:

$$\nabla^2 \mathbf{A} + 2ik \frac{\partial}{\partial z} \mathbf{A} = 0. \quad (1.11)$$

It is assumed that  $\mathbf{A}$  varies very slowly along the propagation direction  $z$ , therefore the second derivative can be neglected so that:

$$\frac{\partial^2 \mathbf{A}}{\partial z^2} \ll \frac{1}{\lambda} \frac{\partial \mathbf{A}}{\partial z}. \quad (1.12)$$

In this way, we can rewrite equation 1.11 as:

$$\left( \frac{\partial^2}{\partial x^2} + \frac{\partial^2}{\partial y^2} + 2ik \frac{\partial}{\partial z} \right) \mathbf{A} = 0. \quad (1.13)$$

The last equation is called "paraxial wave equation". Now let us continue with spin and orbital angular momentum in this regime. For simplicity, we consider the potential  $\mathbf{A}$  posses linear polarization along  $x$  axis.

$$\mathbf{A} = u(x, y, z) e^{i(kz - \omega t)} \hat{\mathbf{x}}. \quad (1.14)$$

Using paraxial approximation and Lorenz Gauge, we have electric field as:

$$\mathbf{E} = ik(u \hat{\mathbf{x}} + \frac{i}{2k} \frac{\partial u}{\partial x} \hat{\mathbf{z}}) e^{ikz}, \quad (1.15)$$

and the Poynting vector is:

$$\begin{aligned} \epsilon_0 \langle \mathbf{E} \times \mathbf{B} \rangle &= \frac{\epsilon_0}{2} (\mathbf{E}^* \times \mathbf{B} + \mathbf{E} \times \mathbf{B}^*) \\ &= i\omega \frac{\epsilon_0}{2} (u \nabla u^* - u^* \nabla u) + \omega k \epsilon_0 |u|^2 \hat{\mathbf{z}}. \end{aligned} \quad (1.16)$$

In the following, it is more convenient to use cylindrical coordinate. To find the expression for the angular momentum, we assume the angular dependency to be in the form of  $u(r, \phi, z) = u(r, z)e^{im\phi}$ . Then, the  $\phi$  component in equation 4.4 can be derived as:

$$\epsilon_0 \langle \mathbf{E} \times \mathbf{B} \rangle_\phi = \frac{\epsilon_0 \omega m |u|^2}{r}, \quad (1.17)$$

multiplying  $r$  to this equation and considering also the polarization of our beam, we can find the angular momentum density along the propagation,  $j_z$  as:

$$j_z = \epsilon_0 (\omega m |u|^2 + \sigma_z \frac{r}{2} \frac{\partial |u|^2}{\partial r}). \quad (1.18)$$

Having the energy as  $\epsilon_0 \omega |u|^2$ , the ratio between angular momentum and energy will be:

$$\frac{J_z}{W} = \frac{m + \sigma_z}{\omega}. \quad (1.19)$$

A more detailed calculation is provided in [11, 12].

In equation 1.19  $\sigma_z$  is linked to the spin angular momentum and is equal to  $\pm 1$  depending on the handedness of circular polarization. As we see it takes just two values. Therefore taking SAM as a degree of freedom provides us with two different options. However,  $m$  which is related to OAM is the eigenvalue of  $L_z$  and can take any integer number. So, it gives us infinite degrees of freedom. For this reason, in many applications of SAM, one can use OAM to enhance their desired results and add more value to it. However, it might happen that adding the degree of freedom does not help. Considering  $m = 0$ , equation 1.19 converts to what Poynting predicted for the ratio.

To conclude this section, we can claim that under the paraxial approximation, the spin and orbital angular momenta of light (a photon) are well-defined and can be measured separately. Many optical (in general physical) cases satisfy this regime. For example, a laser mode, which is the most applicable device in an optical lab, can be described by it. That is why in the following we will give a brief introduction to Gaussian mode, that is the fundamental

mode of a typical laser.

### 1.3.1 Gaussian modes

A common strategy to describe a laser beam propagation is to solve the wave equation in paraxial approximation. One of the simplest solutions in this regime is Gaussian beam. It is also the most available and applicable beam light in most optical labs as it can simply be produced by a laser. For the purpose of our studies, we also used a Gaussian beam for the starting point and by manipulating it we obtained our goal. If the polarization and wavelength are fixed, one can describe a Gaussian beam just by a single parameter called beam waist at  $z = 0$ ,  $w_0$ . The mathematical equation for a Gaussian beam amplitude is provided by:

$$G(r, z) = A_0 \frac{w_0}{w(z)} \exp\left(-\frac{r^2}{w^2(z)}\right) \exp\left(-ik\frac{r^2}{R(z)} - i\text{Arctan}\left(\frac{z}{z_0}\right)\right), \quad (1.20)$$

where  $z_0 = \frac{\pi w_0^2}{\lambda}$  is the "Raileigh range",  $R(z) = z(1 + (\frac{z_0}{z})^2)$  is called "wave-front curvature radius" and finally  $w(z) = w_0\sqrt{1 + (\frac{z}{z_0})^2}$  stands for the "beam radius". Interestingly, a focused Gaussian beam has still a Gaussian pattern but with a smaller beam waist [13].

Having such an amplitude, one can add a phase factor  $e^{im\phi}$  and generate a helical phase front or change its polarization to circular to let it carry SAM. To continue, we talk about devices and methods to manipulate light in order to add angular momentum to it and we start with polarization as it is connected to SAM.

### 1.3.2 Polarization of light and SAM

Polarization of light is referred to the orientation of the electric field oscillations in the transverse plane. Following the outreach of the optical systems sensitive to the polarization of light, controlling this factor has become demanding. However, it may affect the systems which do not measure it. Besides, for some

applications, one needs to alter the light polarization. We will discuss some of its significance as well as its manipulation importance in Chapters 3 and 4.

The light beam is unpolarized if its electric field orients randomly in time. Sunlight is the most familiar unpolarized light for us. On the other hand, if the direction of the electric field fluctuations is explicitly determined, the light is polarized. Laser beams are the most prevalent artificial sources of polarized light in laboratories. One can categorize the polarized light into elliptical, circular, and linearly polarized light. The most general one is the elliptical polarization, while the two linear and circular polarizations are its two important extremes. Let us consider the electric field at the transverse plane in the Cartesian coordinate to be:

$$\mathbf{E} = E_x \hat{\mathbf{e}}_x + E_y \hat{\mathbf{e}}_y, \quad (1.21)$$

where  $E_x = E_{0x} \cos(\omega t - kz + \delta_x)$  and  $E_y = E_{0y} \cos(\omega t - kz + \delta_y)$ . For simplicity, one can use normalized field such that  $E_{0x}^2 + E_{0y}^2 = 1$ .

Having the equation 1.21, when we follow the electric field vector tip behavior over a complete cycle of oscillation, an ellipse which is called polarization ellipse will be achieved and mathematically is described as:

$$\frac{E_x^2}{E_{0x}^2} + \frac{E_y^2}{E_{0y}^2} - 2 \frac{E_x E_y}{E_{0x} E_{0y}} \cos \delta = \sin^2 \delta, \quad (1.22)$$

where  $\delta = \delta_x - \delta_y$  and expresses the phase difference between the two components. Changing the amplitudes and phase, the polarization ellipse changes. Fig. 1.2 demonstrates the tip of the electric field vector movements around mentioned polarization ellipse. When this ellipse collapse to form just a line which means the direction of the electric field vector remains constant during propagation, it is called linear polarization. This is associated to  $\delta = 0, \pi$ . However; when in the equation 1.21,  $E_{0x} = E_{0y}$ , and  $\delta = \pi/2, 3\pi/2$  one can refer to it as circular polarization. Depending on the rotation direction of tip which can be clockwise or anticlockwise, left and right handed circular polarization are described, respectively. This state is related to the SAM of light and as shown in previous section the value is  $-\hbar$  for right handed circular polarization (RHC) and  $+\hbar$  for left handed circular polarization (LHC).



In conclusion, the polarization ellipse can be exploited for defining a polarized light but can not be used to explain unpolarized or partially polarized light [13].

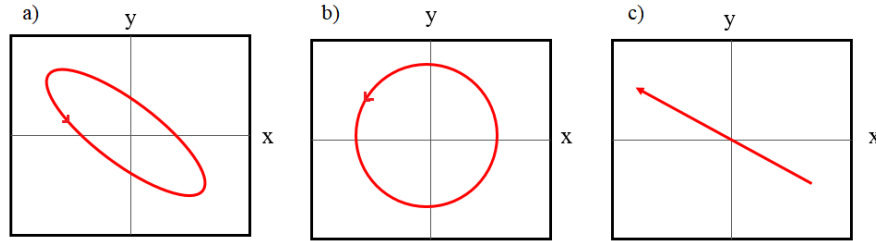


**Figure 1.2:** Polarization ellipses obtained by following the electric field oscillations tip during one cycle. a) General elliptical polarization, b) circular left handed, and c) linear polarization.

In the equation 1.21,  $\mathbf{e}_x$  and  $\mathbf{e}_y$  are the unit vectors along  $x$  and  $y$  axes. In the following, we use complex fields for our purpose, e.g.  $\mathbf{E} = E_{0x}\hat{\mathbf{e}}_x + E_{0y}\hat{\mathbf{e}}_y$  where  $E_{0x}$  and  $E_{0y}$  are complex coefficients. We can introduce four other unit vectors as we will use them in the future:

$$\mathbf{e}_R = \frac{\mathbf{e}_x - i\mathbf{e}_y}{\sqrt{2}}, \quad (1.23a)$$

$$\mathbf{e}_L = \frac{\mathbf{e}_x + i\mathbf{e}_y}{\sqrt{2}}, \quad (1.23b)$$

$$\mathbf{e}_D = \frac{\mathbf{e}_x + \mathbf{e}_y}{\sqrt{2}}, \quad (1.23c)$$

$$\mathbf{e}_A = \frac{\mathbf{e}_x - \mathbf{e}_y}{\sqrt{2}}, \quad (1.23d)$$

where  $R$ ,  $L$ ,  $D$ , and  $A$  show right and left handed circular, diagonal and anti-diagonal polarizations, respectively.

In general, one can use any orthogonal sets of polarization as basis, such as linear or circular polarization and represents the rest based on that. A wise choice of the basis, is based on the convenience and simplification of the calculations. As we see in chapter 2, we opt to use circular polarization basis for our comfort.

Alternative and other common ways to describe the state of polarization (SOP) of a beam are Poincaré sphere and Stokes parameters which can be

used also for unpolarized light. We use the Stokes parameters in Chapters 3 and 4 when we talk about the polarization singularities. An electromagnetic field can be described by a set of values called as Stokes parameters.

$$S_0 = E_x^2 + E_y^2 = I_x + I_y, \quad (1.24a)$$

$$S_1 = E_x^2 - E_y^2 = I_x - I_y, \quad (1.24b)$$

$$S_2 = 2\text{Re}(E_x^* E_y) = I_D - I_A, \quad (1.24c)$$

$$S_3 = 2\text{Im}(E_x^* E_y) = I_L - I_R. \quad (1.24d)$$

where,  $I$  stands for the intensity of each component. The Stokes parameters can be easily measured in an optical setup composed of waveplate and polarizers (to choose the proper component). For a polarized beam,  $S_0^2 = S_1^2 + S_2^2 + S_3^2$ , therefore one can normalize the parameters as  $s_i = S_i/S_0$  where  $i = 0, 1, 2, 3$ . In this way, we can explain the state of polarization in graphical way. Here we can introduce a coordinate corresponding to Cartesian coordinate but with  $(s_1, s_2, s_3)$  as the three axes. One can prove any polarization state defining by normalized Stokes parameters is located on a surface of a sphere with radius equal to unity. This sphere is called "Poincaré sphere" and its origin is at the zero of this coordinate. We recall that partially polarized light can also be defined by this sphere in a way that all the space inside of the sphere is devoted to partially polarized lights. We should mention that the origin of Poincaré sphere represents completely unpolarized light. We can see the graphical view of this approach in Fig. 1.3.

Using the circular polarization basis, we can recover the electric field as:

$$\mathbf{E} = E_R \cos \frac{\theta}{2} \mathbf{e}_R + E_L e^{i\phi} \sin \frac{\theta}{2} \mathbf{e}_L, \quad (1.25)$$

where,  $\phi$  and  $\theta$  show the polar and azimuthal angles, respectively and refer to the position of a point on the Poincaré sphere as shown in Fig. 1.3.

### 1.3.2.1 Tools for polarization manipulation

Polarization manipulation is essential for a great amount of applications ranging from polarimetry to communications. In general for most applications

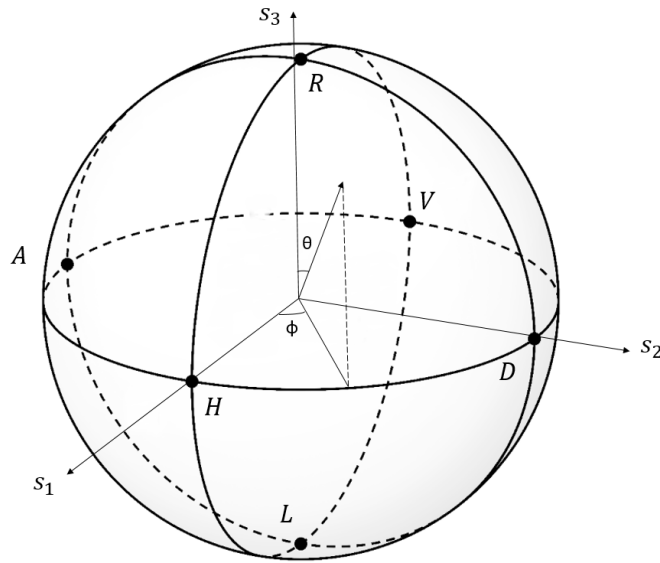


**Figure 1.3:** The Poincaré sphere represented in SAM space. The linear polarizations are located on the equator and RHC and LHC can be found on the north and south poles, respectively.

we need a specific state of polarization. Two common devices to obtain it are polarizers and waveplates.

- **Polarizers**

To select a particular desired polarization and discard the others a polarizer can be a helpful device. In fact, it acts as a filter. Polarizers are important as in some optical setups or devices we need to block some polarizations and let pass a certain one like in Camera filters and sunglasses.

- **Waveplates**

In order to modify the input beam polarization, a birefringent and homogeneous tool known as waveplate or retarder facilitate our work. They generally add a phase shift (due to their birefringence) between the two orthogonal components of the input beam. One can adjust the required phase shift by choosing proper parameters as thickness and refractive index of the plate and wavelength of incident beam. There are two common waveplates: half waveplates and quarter waveplates. A half wave-

plate (HWP) changes the direction of linear polarization and a quarter waveplate (QWP) is used for the conversion between circular and linear polarizations; however, it can generate a general elliptical polarization, as well. Therefore, clearly, a combination of waveplates as QWP-HWP-QWP generates any desirable output polarization.

### 1.3.3 Orbital angular momentum of light and phase singularity

To describe a light beam, we need the information about its state of polarization as well as its spatial distribution. Some features are related to spatial and some to polarization structure of light. There are some properties like "rotation" which is connected to both. We introduced the polarization and hence SAM of light and instruments to manipulate it in the previous section. This section is dedicated to the spatial distribution of the electromagnetic field and orbital angular momentum contribution. Such beams are also called optical vortices and they show a phase singularity as they possess a zero of optical field (optical intensity).

Maybe randomly, there are some sources of structured light (in general any desired light) in the nature. However, one might also decide to manipulate a beam like laser beam in the optical labs in order to transform it into the desired form. Shaping the beam is not only scientifically interesting but also can be exploited for many applications and technologies improvements.

As we discussed if a light beam envelope consists of a phase factor dependent to azimuthal coordinate as  $e^{im\phi}$ , it carries a well-defined amount of OAM, corresponding to one  $\hbar$  per photon. The different states of OAM form a complete and orthogonal set:

$$\langle m|m' \rangle = \delta_{m,m'}. \quad (1.26)$$

In the paraxial approximation, there are some solution of the wave equation with this rotational property. The most familiar one is Laguerre-Gaussian

mode which has a doughnut shape intensity pattern. However, one can also refer to Bessel or Hypergeometric beams for OAM. In Fig. 1.4 some examples of wave and phase front of Laguerre-Gaussian modes are illustrated.

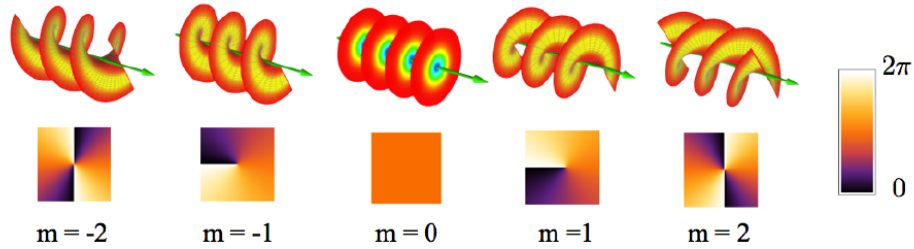


**Figure 1.4:** The wave and phase front structure of light carrying OAM. This image is adapted from the Wikipedia page "Orbital Angular Momentum of light", edited by L. Marucci and E. Karimi.

### 1.3.3.1 Laguerre-Gaussian beam

In cylindrical symmetry, Laguerre-Gaussian ( $LG$ ) modes are a perfect and complete set of solutions for the paraxial wave equation. The azimuthal phase term in their formula  $e^{im\phi}$  means they carry a well-defined amount of OAM. In fact, they are the most common form of structured light as they can be generated directly from a laser. A Laguerre-Gaussian mode is usually characterized by two important parameters  $p$  and  $m$  as in  $LG_{p,m}$ . The first refers to the radial distribution of the intensity pattern in a way that there are  $p + 1$  rings in the structure. The latter, the azimuthal index, is called "topological charge" and denotes the number of complete  $2\pi$  phase cycles around the mode circumference. The scalar field of such beam can be described as [14, 8]:

$$LG_{p,m}(\rho, \xi, \phi) = \sqrt{\frac{2^{(m+1)}p!}{\pi(p+|m|)!(1+\xi^2)}} \left(\frac{\rho}{\sqrt{1+\xi^2}}\right)^{|m|} e^{-\frac{\rho^2}{1+\xi^2}} \quad (1.27)$$

$$L_p^{|m|}(2\rho^2/(1+\xi^2)) e^{i\frac{\rho^2}{\xi+1/\xi}} e^{im\phi} e^{-i(2p+|m|+1)\arctan(\xi)},$$

where  $\rho = r/w_0$  and  $\xi = z/z_0$  are dimensionless coordinates.  $L_p^{|m|}$  represents generalized Laguerre polynomials. The intensity pattern of some  $LG$  modes are provided in Fig. 1.5. As we can see, the  $LG_{00}$  has a Gaussian profile and

carries no OAM and by increasing  $m$  the size of the central hole increases. It is worth mentioning that they are orthogonal, hence they satisfy [8, 1]

$$\langle LG_{p,m} | LG_{p',m'} \rangle = \delta_{p,p'} \delta_{m,m'}. \quad (1.28)$$

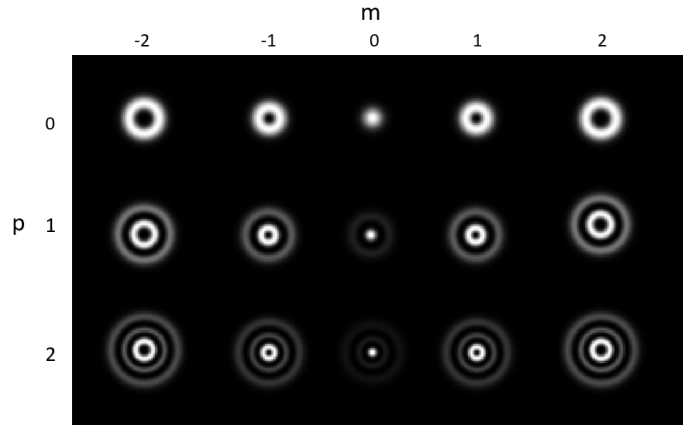


**Figure 1.5:** The intensity pattern of some Laguerre-Gaussian modes. It can be seen that as  $m$  increases, the central hole becomes larger, while  $p$  indicates the number of additional annular rings.  $LG_{00}$  shows a Gaussian profile.

Although such beam can be a laser mode, we can take a fundamental  $TEM_{00}$  mode known as Gaussian mode and manipulate it to produce helical phase front.

### 1.3.4 Tools to manipulate and control OAM of light

As mentioned in the previous section, numerous applications have been developed for twisted beam. Hence, introducing innovative methods for its generation was the focus of many studies for the last three decades. Here, we discuss the most common techniques to manipulate a light beam in order to generate structured light. In all the discussed approaches a laser source (Gaussian beam) passes through an optical element and is converted to a helical beam.

#### 1.3.4.1 Spiral Phase Plate

Maybe, the most straightforward way to generate a twisted beam can be achieved by passing a plane wave through an optical element with a helical

surface which is called spiral phase plate (SPP). As it is shown in Fig 1.6, the SPP can add a helical phase  $e^{im\phi}$  to the input Gaussian beam. In order to add such phase to the beam, the thickness of the device must increase gradually proportional to the azimuthal angle  $\phi$ .

When a SPP is illuminated by a light beam, the wave front goes through a phase shift  $\delta$ :

$$\delta = \frac{(n_1 - n_2)\lambda}{h}\phi, \quad (1.29)$$

where,  $\lambda$  is the wavelength of the input beam,  $n_1$  and  $n_2$  are the refractive indices of the plate and medium, respectively. And  $h$  which is the physical height of the step when  $\phi = 0$  is [15]:

$$h = \frac{l\lambda}{(n_1 - n_2)}. \quad (1.30)$$

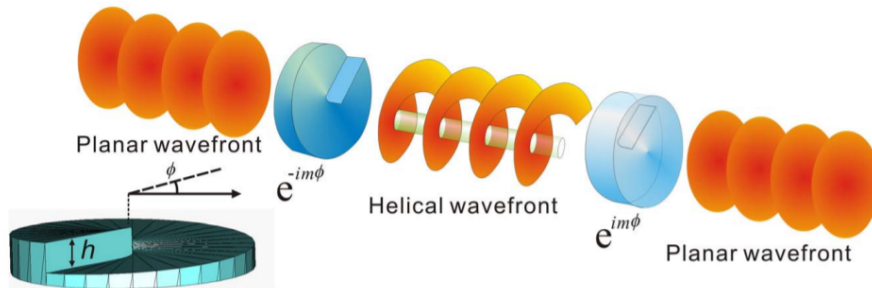


**Figure 1.6:** Schematic of a spiral phase plate and its optical effect. The first SPP is applied to add OAM equal to  $-m\hbar$  to the input beam and the second one cancels the effect of the first SPP by adding  $m\hbar$  orbital angular momentum to the generated vortex beam [16].

#### 1.3.4.2 Computer Generated Holograms

Perhaps, the simplest way to generate any arbitrary beam wavefront can be holography technique. In this approach, the desired pattern is obtained by recording the interference pattern between the reference and any interested beam (phase and wavefront profile) on a "hologram". Then, if we illuminate the hologram with reference beam, we can recover the phase and intensity of the wanted pattern after the hologram. In order to make things easier, one

can find the interference pattern numerically or analytically and then record it on the hologram (such as photographic film or a spatial light modulator) and that is why it is called computer generated hologram [17].

Let us focus on generation of light carrying OAM. Having the laser beam as Gaussian, one needs to add a phase factor  $e^{im\phi}$  to it to produce helical beam. Calculating (with computer) the interference pattern between a reference plane wave  $E_0e^{ik_x x}$  and a helical beam  $E_0e^{im\phi}$ , both propagating in z direction, one will produce a fork shape pattern. So, it must be the registered scheme on the hologram. Here is the intensity pattern of the interference,  $I$ :

$$I = 2|E_0|^2(1 + 2\cos(k_x x - m\phi)). \quad (1.31)$$

Fig. 1.7, shows this pattern and as it is clear from the image, the splitting of the lines happens at the place of the phase singularity. And the value of  $m$  can be retrieved from the difference of the lines number above and below the singularity.

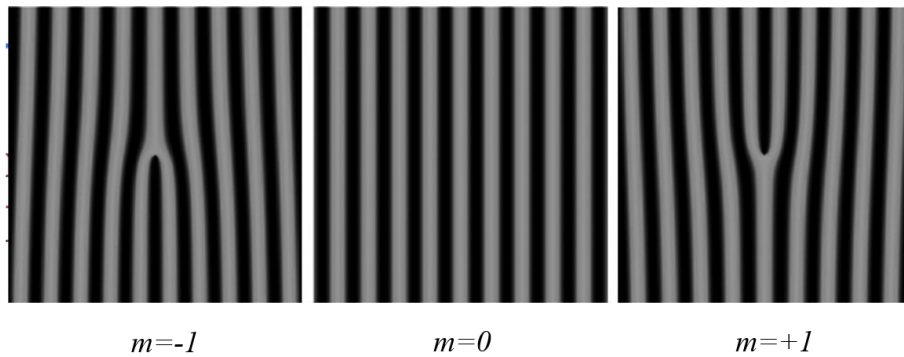


**Figure 1.7:** Pitchfork intensity pattern of the reference plane wave and a helical beam. One can determine the value of OAM from the difference between the number of upper and lower fringes.

The transmitted field from a hologram is like other devices as:

$$E_t = T(x, y)E_0. \quad (1.32)$$

where  $T(x, y)$  is the transmission function and for hologram is

$$T(x, y) = \frac{1}{2}(1 + \cos(k_x x - m\phi)). \quad (1.33)$$



Therefore after the hologram, we have:

$$E_t = \frac{1}{2}E_0(1 + \frac{1}{2}e^{i(k_x x - m\phi)} + e^{-i(k_x x - m\phi)}). \quad (1.34)$$

As one can understand from equation 1.34, a part of beam is unchanged which is the zero order of diffraction. The diffracted part is made of two distinct beams. One with  $e^{im\phi}$  phase, the first diffractive order and the other with  $e^{-im\phi}$  which is the order of negative first.

To the best of our knowledge, it is the most widespread way of OAM generation although there might be just one drawback in using this technique which is its poor efficiency to generate structured light.

### 1.3.4.3 Cylindrical Lenses Mode Converters

As it is clear, Gaussian beam is not the only solution of wave equation. As an illustration, Hermit-Gaussian (*HG*) beams are another solution in the Cartesian coordinate and they have the following expression [13]:

$$U_{n,m}(x, y, z) = A_{n,m} \left( \frac{w_0}{w(z)} \right) G_n \left( \frac{\sqrt{2}x}{w(z)} \right) G_m \left( \frac{\sqrt{2}y}{w(z)} \right) \times \exp \left\{ -ikz - ik \left( \frac{x^2 + y^2}{2R(z)} \right) + i(n + m + 1)\xi(z) \right\}, \quad (1.35)$$

where  $A_{n,m}$  is a constant and  $n, m = 0, 1, 2, ..$  and

$$G_n(u) = H_n(u)e^{(-u^2/2)} \quad (1.36)$$

is the Hermit-Gaussian function. As  $H_0(u) = 1$ , Hermit-Gaussian function of order zero is basically a Gaussian mode. The intensity pattern of these modes are described as:

$$I_{n,m}(x, y, z) = (A_{n,m})^2 \left( \frac{w_0}{w(z)} \right)^2 \left( G_n \left( \frac{\sqrt{2}x}{w(z)} \right) \right)^2 \left( G_m \left( \frac{\sqrt{2}y}{w(z)} \right) \right)^2. \quad (1.37)$$

Fig. 1.8 provides the intensity patterns of some of these modes. We should mention that  $n$  and  $m$  express the minimum of intensity in  $x$  and  $y$  directions, respectively.

As they are a complete and orthogonal set of modes, one can expand any other modes as sum of these modes with proper coefficient (weight).

$$\langle HG_{n,m} | HG_{n',m'} \rangle = \delta_{n,n'} \cdot \delta_{m,m'} \quad (1.38)$$

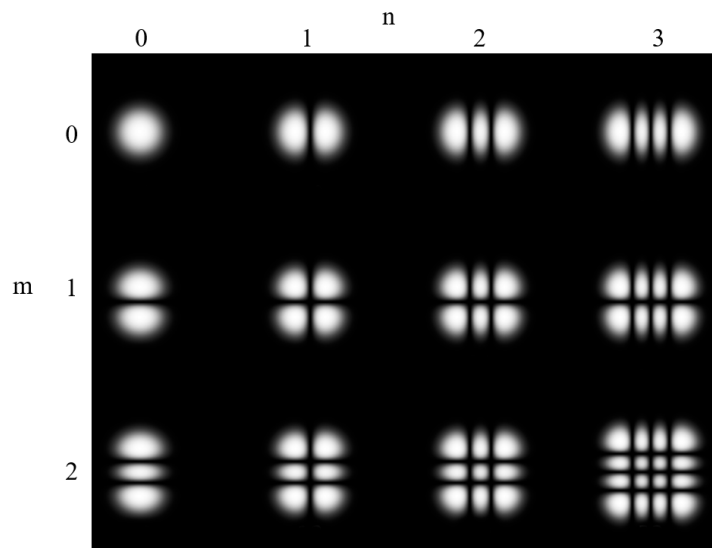


**Figure 1.8:** The intensity pattern of some Hermit-Gaussian modes.  $n$  and  $m$  show the number of minimum in intensity in  $x$  and  $y$  directions, respectively.

Hence, an  $LG$  mode can be represented as sum of  $HG$  modes. Let us consider the Laguerre-Gaussian mode of first order. One can rewrite it as:

$$LG_{01} = \frac{1}{\sqrt{2}}(HG_{01} + iHG_{10}). \quad (1.39)$$

Here  $i$  can be correspond to a phase difference equivalent to  $\pi/2$  ( $e^{i\pi/2} = i$ ) and  $\frac{1}{\sqrt{2}}$  is for the normalization. Other  $LG$  modes can be expanded similarly from the other orders of  $HG$  modes.

In 1992, Allan et al. figured out that such phase shift can be produced by cylindrical lenses. When different modes pass through cylindrical lens, they experience different Gouy phase and therefore there will be a phase difference between them. To achieve the desired phase shift there must be  $f/\sqrt{2}$  distance between two aligned lenses, where  $f$  expresses the focal length of each lens. Using same technique, one can change the sign of OAM. This happens when the lenses are  $2f$  apart and of course well-aligned [1, 8]. This was the very first method to generate structured light in the lab. However, to generate each  $LG$  mode, a specific input  $HG$  mode is needed. This can be a drawback which prevents it to be a versatile way of OAM generation in the optical labs.

#### 1.3.4.4 Liquid Crystal Based device to manipulate SAM and OAM of light

The limitations, difficulties, and drawbacks of previously mentioned methods, make them not the ideal way to generate OAM, at least for certain applications. Besides, they all manipulate the beam wavefront by adding a phase to it without changing its polarization. As we have seen, for years, it was considered that there is no interaction between SAM and OAM of light and each of them was an independent degree of freedom.

However, in 2006, Marrucci et al. introduced an optical device, called q-plate, which results in spin-orbit coupling [18, 19]. As discussed in 1.3.2 an anisotropic birefringent media with uniform optic axis can change the polarization of light. But adding a proper non-uniformity to the optic axis leads to producing a further phase in the incident beam. Therefore, they designed and fabricated an anisotropic birefringent plate with "inhomogeneous" optic axis, which changes at each point of the transverse plane of the plate. A q-plate is essentially a liquid crystal layer sandwiched between two glass substrates, with a peculiar singular pattern of molecular alignment, which creates the desired non-uniformity in the optic axis. The optic axis of the device forms an angle  $\alpha(x, y)$  with the x axis, where  $\alpha$  depends on the position according to the following law (in polar coordinates):

$$\alpha(\phi) = q\phi + \alpha_0, \quad (1.40)$$

where  $\phi$  is the azimuthal angle,  $\alpha_0$  is the angle at  $\phi = 0$  and is a constant value and  $q$  shows the topological charge of the plate and that is the reason they named it q-plate. Here, we considered there is just a linear dependency to the azimuthal angle. Fig. 1.9 demonstrates some of the patterns for different topological charge and  $\alpha_0$ .

Like other wave plates, a q-plate induces a phase delay  $\delta$  between the two orthogonal components of the impinging beam and as mentioned this phase delay depends on the wavelength of incident beam, thickness and refractive indices of the plate along fast and slow axis. To have a uniform  $\delta$ , one can choose

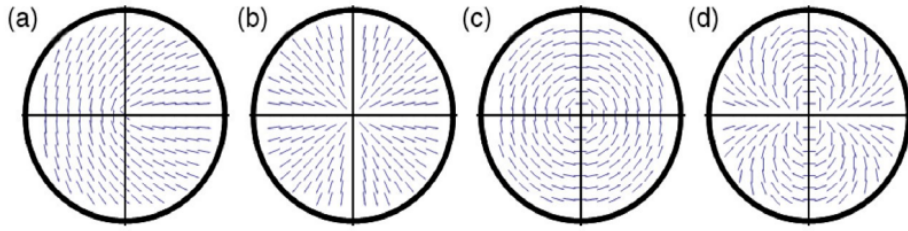


**Figure 1.9:** Spin-orbit coupling with q-plate. The pattern of optic axis of a q-plate is illustrated, a)  $q = 1/2$ ,  $\alpha_0 = 0$ , b)  $q = 1$ ,  $\alpha_0 = 0$ , c)  $q = 1$ ,  $\alpha_0 = \pi/2$ , d)  $q = 2$ ,  $\alpha_0 = 0$ . The image is adapted from [11].

to have a uniform thickness along the  $z$ -direction (propagation direction). In general, the Jones matrix of a space-variant waveplates with non-uniform  $\delta$  is:

$$\hat{U}(\alpha, \delta) = \cos\left(\frac{\delta(x, y)}{2}\right) \begin{pmatrix} 1 & 0 \\ 0 & 1 \end{pmatrix} + i \sin\left(\frac{\delta(x, y)}{2}\right) \begin{pmatrix} 0 & e^{2i\alpha(x, y)} \\ e^{-2i\alpha(x, y)} & 0 \end{pmatrix}. \quad (1.41)$$

For a uniform retardation, one can just simply remove the dependency to  $x$  and  $y$ . In this chapter we mainly focus on a uniform  $\delta$  which is the case of a normal q-plate; However, in chapter 3, we see that a non-uniform phase retardation can be exploited for the applications when we need inhomogeneous polarization structure.

Based on the input beam polarization, q-plate manipulates the beam profile and adds a phase factor  $e^{im\phi}$  to it, and for this reason the method is called spin-orbit coupling of light.

To have a pure helical beam after the q-plate (tuned q-plate), the value of phase retardation  $\delta$  should be  $\pi$ , which is the case of HWP configuration. Let us consider we have circular polarization as input. Substituting  $\alpha$  from equation 1.40, in equation 1.41 for a tuned q-plate leads to:

$$\hat{U}(\alpha, q)|L\rangle = |R\rangle i e^{2iq\phi} e^{2i\alpha_0}, \quad (1.42a)$$

$$\hat{U}(\alpha, q)|R\rangle = |L\rangle i e^{-2iq\phi} e^{-2i\alpha_0}. \quad (1.42b)$$

Figure 1.10 demonstrates the effect of input polarization on the polarization of generated helical beam.

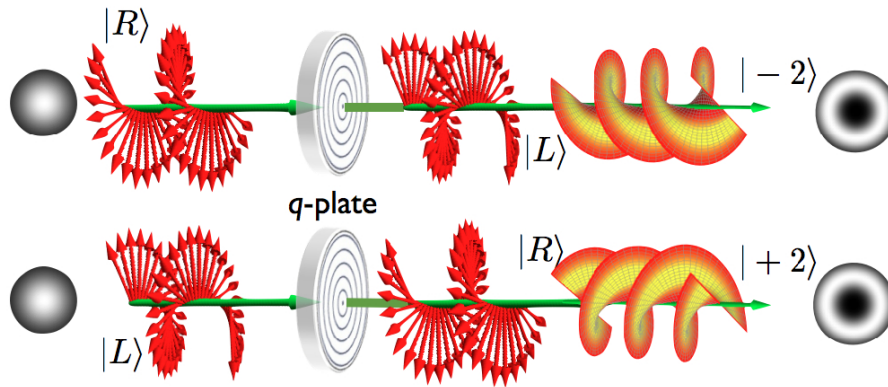


**Figure 1.10:** Generation of a beam carrying OAM with a tuned q-plate. Picture adapted from the Wikipedia page "Angular momentum of light".

However, according to 1.41, the action of a q-plate with  $0 \leq \delta \leq 2\pi$  on a circular polarization input is described as below:

$$U_{q\text{-plate}}|R, m\rangle \rightarrow \cos(\delta/2)|R, m\rangle + i \sin(\delta/2)e^{+2i\alpha_0}|L, m - 2q\rangle, \quad (1.43a)$$

$$U_{q\text{-plate}}|L, m\rangle \rightarrow \cos(\delta/2)|L, m\rangle + i \sin(\delta/2)e^{-2i\alpha_0}|R, m + 2q\rangle, \quad (1.43b)$$

where  $m$  is the orbital angular momentum value of the input beam. Based on the value of  $\delta$ , we can have different superposition of right and left handed circular polarization. Noticing the equations 1.43, one can perceive that beam after q-plate is composed of two terms. The part proportional to  $\cos \delta/2$  remains untouched (both polarization and phase) while the term proportional to  $\sin \delta/2$  alters the handedness of circular polarization and changes OAM by  $\pm 2q$  based on input handedness.

In order to vary the value of phase retardation  $\delta$ , one can apply external electric field to the plate [20]. In this way, one can choose the proper value of delta for the aim of their experiment. Fig 1.11 shows the experimental data of phase retardation by changing voltage for a q-plate with  $q = 1/2$ . It is clear that  $\delta_\pi$  happens when the voltage is 280 V and when the voltage is 400 V we have completely untuned q-plate.

As circular polarization basis is a complete set, one can expand other basis based on it. As an example, we recall that it is possible to write linear polarizations in terms of circular polarizations. Let us assume a simple case of

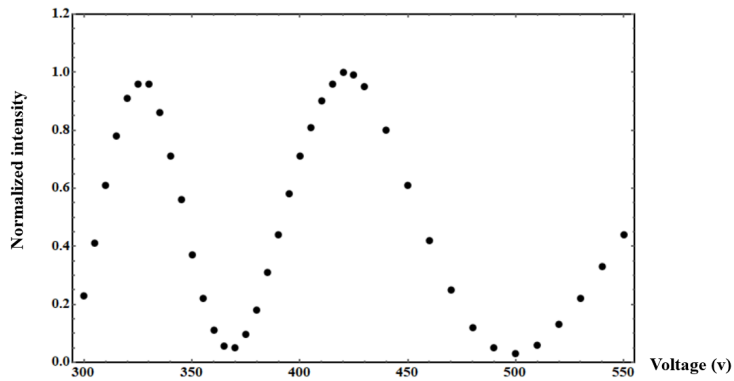


**Figure 1.11:** Tuning the q-plate by applying an external electric field. The plot shows the intensity of converted beam vs applied voltage. The complete tuned q-plate ( $\delta = \pi$ ) appears when we have the maximum intensity which is correspond to  $V=320$  V. In contrast the untuned q-plate ( $\delta = 0$ ) is for  $V=360$  V where the intensity is minimum.

having a horizontal linear input. Therefore, we can write:

$$|H\rangle = \frac{|R\rangle + |L\rangle}{\sqrt{2}}. \quad (1.44)$$

Using equations 1.43, and 1.44, we can rewrite the action of q-plate on the input beam as:

$$U_{q\text{-plate}}|H, 0\rangle \rightarrow \frac{1}{\sqrt{2}} [(\cos \delta/2 + i \sin \delta/2 e^{2iq})|R\rangle + (\cos \delta/2 + i \sin \delta/2 e^{-2iq})|L\rangle]. \quad (1.45)$$

For simplicity we considered  $\alpha_0$  and  $m$  equal to zero. Now, for a tuned q-plate,  $\delta = \pi$ , the equation 1.45 can be reduced to:

$$U_{q\text{-plate}}|H, 0\rangle \rightarrow \frac{1}{\sqrt{2}} (|R, 2q\rangle + |L, -2q\rangle). \quad (1.46)$$

In general, one can reproduce any state of polarization as a superposition of circular polarizations. We should notice that when we have a superposition of right and left handed circular polarization as the input, SAM and OAM of output are not separable anymore. However, by choosing different values for  $q$  and adjusting the input polarization, we can engineer the desired complex structured beams.

All the mentioned instruments are used in free space. These days, there is huge attention toward guided modes in optical fibers. The reason is due to guided mode applications. In Chapters 2 and 3, we introduce optical fibers and their guided modes. Also, we talk about OAM generation in optical fibers and we see how we can greatly benefit from a special kind of q-plate to maximize light coupling into an optical fiber. Later on in Chapter 4, we see how we can tailor a beam and generate a desired amplitude and add polarization singularity, as well to it.

# Chapter 2

## Improved Scalar Mode Matching

### 2.1 Introduction

An optical fiber refers to a z-invariant dielectric structure (waveguide) that confines laterally the light by the principle of total internal reflection. Thanks to their many applications in science and technology, optical fibers have been an interesting subject of research and industry development since their invention. Having a very small size (diameter), an optical fiber can be compared to a human hair which is around  $120 \mu m$ . Concerning the internal reflection and mechanical support, a typical optical fiber consists of three parts as the following:

- **Core**, a low-loss inner part in which most of the light energy is confined and forwarded.
- **Cladding**, which surrounds the core and has a slightly lower refractive index than core to support total internal reflection; a part of light energy goes to this region.
- **Coating**, a plastic layer around the cladding to protect the fiber against external damages and moisture. This part is not strictly functional in



the optical fiber, so it can be absent, but it is needed in most practical applications [13].

Fig 3.6 reports these three main parts of an optical fiber. As it can be seen, the cladding layer reflects the light into the core. Optical fibers' capability to transmit more data (information) in long distances has improved the technologies such as communications. However, the very first fibers had a high energy loss and could be used just in short distances. Now let us see briefly how the optical fiber industry reached this high level.

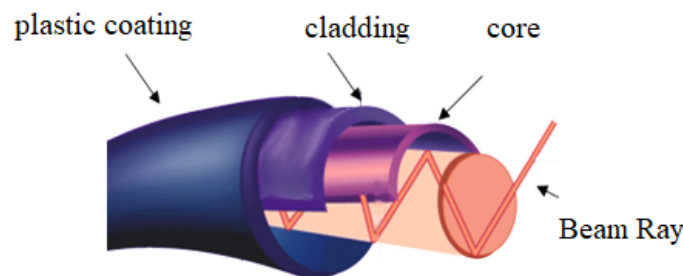


**Figure 2.1:** The three main parts of an optical fiber. The light ray travels into the core by the principle of total internal reflection.

### 2.1.1 Optical fiber history

Light has been one of the first tools to communicate among humans. As a consequence, propagating and controlling it for a diverse range of applications have been demanding through the years. In the year 1840, the first attempts were done by Daniel Collodon and Jaques Babinet to demonstrate they could guide light along a water jet. Using the same approach, John Tyndall showed one can transmit the light through a stream of water. The next step was to direct the light signal along other materials such as glass. Subsequently, in the 1950s, they realized using another layer around the light path (core) could lead to a better transmission, and finally, the invention of lasers in 1960 and hence having a coherent source of light opened a new window in light transmission.

However, there was still the problem of high energy loss along the distance. To reduce this loss, in 1964, Charles K. Kao proposed to use purer forms of glasses as an environment to guide the light. On that account, the optical fiber industry flourished. By all the improvement in the fiber industry, now light can travel along them in long distances with low loss [21, 22, 23].

### 2.1.2 Optical Fibers Classifications

Based on the number of transmitted modes, optical fibers are classified into two main types. We talk about fiber modes in the next section.

- **single-mode fibers (SMF)** in which just one mode (fundamental mode) is allowed to propagate at a time. A typical SMF has a small core diameter around 6 to 9  $\mu m$ . However, some other core diameters are available, as well. Telecommunications is one of the main applications of such optical fibers. In this chapter, our focus is on the single-mode fibers.
- **Multi-mode fibers (MMF)** that are designed to be able to guide more than one mode at a time. The wavelength of the input beam, the diameter, and refractive index of core determine the number of supported modes. A typical multi-mode fiber has a core diameter around 60  $\mu m$  [13].

There is another classification that is based on the core refractive index. If the refractive index of core is uniform it refers to step-index fiber. However, In graded index fiber, the core refractive index decreases gradually going from center to cladding [13, 24]. Our focus is on the step-index single-mode fiber.

Due to its larger core diameter, an MMF has a higher attenuation. Hence, the SMF is more suitable for long distance applications.

Talking about the applications of optical fibers, here we can mention some. As we face a growth in the global population, maybe we can claim that medical applications of fibers are among the most important ones. Due to their unique properties, optical fibers are greatly exploited for patient diagnosis and also treatment [25, 26]. They can also be used in surgeries or endoscopy [27, 28].

Apart from the medical applications, they are applied in telecommunications, as well, which is another significant application of optical fibers. Thanks to them, we can transfer more data faster and safer in longer distances [29, 30]. Sensing is another worth-mentioning application of optical fibers which can be used also in communications and medicine [31]. Some other applications are mentioned in ref. [32, 33].

To exploit an optical fiber in applications, it is usually important to send as much light as possible to it. Suppose we send a signal with wavelength  $\lambda = 1550 \text{ nm}$  into a low-loss optical fiber with a loss about  $0.154 \text{ dB/km}$ . Then, after propagating  $20 \text{ km}$  in the fiber core, the signal loses about 50% of its intensity [24]. Clearly, if we can send as much light as possible into the fiber, there will be more power left after  $20 \text{ km}$ . Therefore, the coupling efficiency is an important factor when working with fibers, as it describes what fraction of the input beam is coupled into fiber modes.

In this chapter, we discuss the problem of optimizing the coupling of a free-space beam into a single-mode optical fiber and calculate what can be the best amplitude profile for optimizing the coupling into a single-mode step-index fiber. We further discuss how a properly designed q-plate can help us improve in principle the coupling efficiency between a laser source and a single-mode step-index fiber. As we will show, high efficiency coupling becomes more challenging in nanofibers where the vectorial structure of the field becomes more prominent, and this is the area in which the vectorial patterning allowed for by q-plates can be most useful. To begin with, we introduce optical fiber modes. We show how the amplitude and polarization of the fundamental mode (our interest) of a single-mode fiber change by reducing the core size. We also discuss other methods and devices used in literature to increase coupling efficiency. Finally, in the next chapter, we introduce our technique that is a novel application of q-plates to manipulate lights' polarization structure and improve the coupling efficiency.

## 2.2 Optical Fiber Modes

To realize how to improve coupling efficiency in optical fibers, it is necessary to understand the structure of exact fiber modes. We recall that the behavior of electromagnetic waves is governed by Maxwell's equations as discussed in Chapter 1 equations 1.1. The optical fiber modes are the possible solutions of wave equation and are a set of orthogonal eigenfunctions. The fiber fundamental guiding mode is of huge and special importance, because one can design an optical fiber to propagate just this mode. Thus, here, we are just interested in the fundamental mode of a step-index single-mode optical fiber (usually labeled  $HE_{11}$ ).

As an ideal optical fiber has a perfect cylindrical core, it is more convenient to solve it in cylindrical coordinate such that

$$\mathbf{E}(r, \phi, z) = E_r(r, \phi, z)\hat{\mathbf{r}} + E_\phi(r, \phi, z)\hat{\phi} + E_z(r, \phi, z)\hat{\mathbf{z}}, \quad (2.1a)$$

$$\mathbf{H}(r, \phi, z) = H_r(r, \phi, z)\hat{\mathbf{r}} + H_\phi(r, \phi, z)\hat{\phi} + H_z(r, \phi, z)\hat{\mathbf{z}}. \quad (2.1b)$$

An optical fiber can support transverse electric (TE) modes with  $E_z = 0$ , transverse magnetic (TM) modes with  $H_z = 0$ , and the most general form where none of the components of the fields is zero,  $E_z \neq 0$  and  $H_z \neq 0$ , called hybrid modes ( $HE$  and  $EH$ ). Our focus is on hybrid modes as they are the exact and complete solutions. In general, in this regime, one can write the structure of transverse fields in terms of longitudinal ones

$$\mathbf{E}_t(r, \phi, z) = \frac{i\beta}{\omega^2\mu\epsilon - \beta^2} \left( \left( \hat{\mathbf{r}} \frac{\partial}{\partial r} + \hat{\phi} \frac{\partial}{r\partial\phi} \right) E_z - i\omega\mu \left( \hat{\phi} \frac{\partial}{\partial r} - \hat{\mathbf{r}} \frac{\partial}{r\partial\phi} \right) H_z \right), \quad (2.2a)$$

$$\mathbf{H}_t(r, \phi, z) = \frac{i\beta}{\omega^2\mu\epsilon - \beta^2} \left( \left( \hat{\mathbf{r}} \frac{\partial}{\partial r} + \hat{\phi} \frac{\partial}{r\partial\phi} \right) H_z + i\omega\epsilon \left( \hat{\phi} \frac{\partial}{\partial r} - \hat{\mathbf{r}} \frac{\partial}{r\partial\phi} \right) E_z \right), \quad (2.2b)$$

where  $\beta$  is the propagation constant of each mode. It is clear that to find an exact form for the transverse fields, one needs to find the longitudinal ones.

Optical fibers are z-invariant media, then in cylindrical coordinate,  $E_z$  and  $H_z$  do not couple into transverse fields. So, by solving Maxwell's equations,

the total longitudinal fields amplitude for a step-index cylindrical fiber can be written as

$$E_z(r, \phi, z) = \begin{cases} AJ_m(ur/a)e^{im\phi}e^{i\beta z} & r \leq a \\ A\frac{J_m(u)}{K_m(w)}K_m(wr/a)e^{im\phi}e^{i\beta z} & r > a \end{cases} \quad (2.3)$$

$$H_z(r, \phi, z) = \begin{cases} BJ_m(ur/a)e^{im\phi}e^{i\beta z} & r \leq a \\ B\frac{J_m(u)}{K_m(w)}K_m(wr/a)e^{im\phi}e^{i\beta z} & r > a \end{cases} \quad (2.4)$$

Here, we ignored the dependency on time.  $a$  is the core radius, and  $m$  stands for the mode order that shows the total angular momentum (hence not only the OAM component) of the corresponding mode.  $J_m(r)$  and  $K_m(r)$  are the  $m$ th order of Bessel and modified Bessel functions, respectively. In the above equations, we defined  $u$  and  $w$  as the wave number in the core and cladding along the transverse direction, where

$$u = a\sqrt{k_0^2 n_1^2 - \beta^2}, \quad (2.5a)$$

$$w = a\sqrt{\beta^2 - k_0^2 n_2^2}, \quad (2.5b)$$

$n_1$  and  $n_2$  represent the refractive index of core and cladding, respectively and  $k_0 = 2\pi/\lambda$ . Here we define another important parameter in an optical fiber which is linked to the number of modes.

$$V = u^2 + w^2 = a^2 k_0^2 (n_1^2 - n_2^2). \quad (2.6)$$

If  $V \leq 2.405$ , the fiber is single-mode fiber and for the  $V$  greater than that value, we have multi-mode fiber.

Substituting equations 2.3 and 2.4 into 2.2, we can have electromagnetic field transverse components as the following:

In the core region ( $r \leq a$ ):

$$E_r(r) = \frac{a}{2u} [J_{m-1}\left(\frac{ur}{a}\right)(Ai\beta_m - B\omega\mu) + J_{m+1}\left(\frac{ur}{a}\right)(-Ai\beta_m - B\omega\mu)], \quad (2.7a)$$

$$H_r(r) = \frac{a}{2u} [J_{m-1}\left(\frac{ur}{a}\right)(Bi\beta_m - A\omega\epsilon_1) + J_{m+1}\left(\frac{ur}{a}\right)(-Bi\beta_m - A\omega\epsilon_1)], \quad (2.7b)$$

and

$$E_\phi(r) = \frac{a}{2u} [J_{m-1}\left(\frac{ur}{a}\right)(A\beta_m + i\omega\mu\beta_m) + J_{m+1}\left(\frac{ur}{a}\right)(A\beta_m - i\omega\mu\beta_m)], \quad (2.8a)$$

$$H_\phi(r) = \frac{a}{2u} [J_{m-1}\left(\frac{ur}{a}\right)(-B\beta_m + iA\omega\epsilon_1\beta_m) + J_{m+1}\left(\frac{ur}{a}\right)(-B\beta_m - iA\omega\epsilon_1\beta_m)]. \quad (2.8b)$$

And in the cladding region ( $r > a$ ):

$$E_r(r) = \frac{a}{2w} \frac{J_m(u)}{K_m(w)} [K_{m-1}(ur/a)(Ai\beta_m - B\omega\mu) + K_{m+1}(ur/a)(-Ai\beta_m - B\omega\mu)], \quad (2.9)$$

$$H_r(r) = \frac{a}{2w} \frac{J_m(u)}{K_m(w)} [K_{m-1}(ur/a)(Bi\beta_m - A\omega\epsilon_2) + K_{m+1}(ur/a)(Bi\beta_m - A\omega\epsilon_2)], \quad (2.10)$$

$$E_\phi(r) = \frac{a}{2w} \frac{J_m(u)}{K_m(w)} [K_{m-1}(ur/a)(-B\beta_m - Ai\omega\epsilon_1\beta_m) + K_{m+1}(ur/a)(B\beta_m - Ai\omega\epsilon_1\beta_m)], \quad (2.11)$$

and finally,

$$H_\phi(r) = \frac{a}{2w} \frac{J_m(u)}{K_m(w)} [K_{m-1}(ur/a)(-B\beta_m + iA\omega\epsilon_2\beta_m) + K_{m+1}(ur/a)(B\beta_m + iA\omega\epsilon_2\beta_m)]. \quad (2.12)$$

Applying the boundary conditions between core and cladding at  $r = a$  (for  $E_\phi$ ,  $H_\phi$ ) will lead us to obtain the characteristics (dispersion) equation for the step-index fiber.

$$\left(\frac{1}{u^2} + \frac{1}{w^2}\right)\left(\frac{\mu_1\epsilon_1}{u^2} + \frac{\mu_2\epsilon_2}{w^2}\right)m^2 J_m^2(u) = \left(\epsilon_1 \frac{J'_m(u)}{u} + \epsilon_2 \frac{J_m(u)K'_m(w)}{wJ_m(u)}\right). \quad (2.13)$$

One can find the propagation constant of a mode by solving equation 2.13 together with 2.6, numerically [24, 34]. For instance, for  $n_1 = 1.5$ ,  $n_2 = 1.48$  and core radius equal to  $3\mu m$  in a single-mode fiber with  $m = 1$ , we calculated  $\beta_m$  equal to  $6.071/\mu m$ . Equation 2.13 also shows that  $\beta_m = \beta_{-m}$ , which means the modes will be degenerate in pairs, due to the fiber mirror symmetry. Interestingly, modes with opposite angular momentum show the symmetry as:

$$E_r^{-m} = E_r^m, \quad E_\phi^{-m} = -E_\phi^m, \quad E_z^{-m} = E_z^m, \quad (2.14a)$$

$$H_r^{-m} = -H_r^m, \quad H_\phi^{-m} = H_\phi^m, \quad H_z^{-m} = -H_z^m. \quad (2.14b)$$

In the following we see that we opt to choose a general representations of the fiber modes in AM basis to facilitate our calculations.

### 2.2.1 Vectorial structure of the optical fiber modes

In a general form, a propagated electromagnetic field in an optical fiber with the eigen modes  $\begin{bmatrix} \mathbf{E}_m \\ \mathbf{H}_m \end{bmatrix}$  can be written as:

$$\mathbf{E}_m(r, \phi, z) = e^{im\phi} e^{i\beta_m z} \left( E_r^m(r) \hat{\mathbf{r}} + E_\phi^m(r) \hat{\boldsymbol{\phi}} + E_z^m(r) \hat{\mathbf{z}} \right), \quad (2.15a)$$

$$\mathbf{H}_m(r, \phi, z) = e^{im\phi} e^{i\beta_m z} \left( H_r^m(r) \hat{\mathbf{r}} + H_\phi^m(r) \hat{\boldsymbol{\phi}} + H_z^m(r) \hat{\mathbf{z}} \right). \quad (2.15b)$$

Rewriting equations 2.15 in circular polarization basis, turns it into:

$$\mathbf{E}_m = e^{i\beta_m z} \left( e^{i(m-\sigma)\phi} E_\sigma^m(r) \hat{\mathbf{e}}_\sigma + e^{i(m+\sigma)\phi} E_{-\sigma}^m(r) \hat{\mathbf{e}}_{-\sigma} + E_z^m(r) \hat{\mathbf{z}} \right), \quad (2.16a)$$

$$\mathbf{H}_m = e^{i\beta_m z} \left( e^{i(m-\sigma)\phi} H_\sigma^m(r) \hat{\mathbf{e}}_\sigma + e^{i(m+\sigma)\phi} H_{-\sigma}^m(r) \hat{\mathbf{e}}_{-\sigma} + H_z^m(r) \hat{\mathbf{z}} \right), \quad (2.16b)$$

here we used the notation  $\hat{\mathbf{e}}_\sigma = \frac{1}{\sqrt{2}}(\hat{\mathbf{x}} + i\sigma\hat{\mathbf{y}})$  for the unit vector of right and left handed circular polarization where  $\sigma = \pm 1$  for left and right handed circular

polarization , respectively. And therefore,

$$E_{\sigma}^m = \frac{1}{\sqrt{2}}(E_r^m - i\sigma E_{\phi}^m), \quad (2.17a)$$

$$H_{\sigma}^m = \frac{1}{\sqrt{2}}(H_r^m - i\sigma H_{\phi}^m). \quad (2.17b)$$

It is clear from the equations 2.16 that the eigen-modes in AM basis are complex structured fields with coherent superposition of fields carrying  $\sigma\hbar$  amount of SAM and  $(m-\sigma)\hbar$  of OAM. Interestingly, these eigen-modes possess the highest symmetry.

As mentioned, mode  $m$  and  $-m$  are a complete and orthonormal set of degenerate solutions for the characteristic equation. Thus, any linear combination of them can also be a solution for the fiber modes. In this way, we can define another basis called "even and odd" basis as follow:

$$\begin{bmatrix} \mathbf{E}_{o,|m|} \\ \mathbf{H}_{o,|m|} \end{bmatrix} = \frac{\text{sign}(m)}{\sqrt{2}} \left( \begin{bmatrix} \mathbf{E}_m \\ \mathbf{H}_m \end{bmatrix} - \begin{bmatrix} \mathbf{E}_{-m} \\ \mathbf{H}_{-m} \end{bmatrix} \right), \quad (2.18a)$$

$$\begin{bmatrix} \mathbf{E}_{e,|m|} \\ \mathbf{H}_{e,|m|} \end{bmatrix} = \frac{1}{\sqrt{2}} \left( \begin{bmatrix} \mathbf{E}_m \\ \mathbf{H}_m \end{bmatrix} + \begin{bmatrix} \mathbf{E}_{-m} \\ \mathbf{H}_{-m} \end{bmatrix} \right), \quad (2.18b)$$

where  $\{e, o\}$  represent even and odd modes. This representation of modes has linear state of polarization across the fiber cross section. Thus, this is more convenient to use this basis for presenting intensity pattern and polarization structure of fiber modes. However, we realized that by reducing the core size and hence increasing the refractive index contrast between core and cladding (in order to stay in single-mode regime), the spatial amplitude distribution and state of polarization of the fundamental mode change. We reported an example of this change in Fig. 2.2, 2.3. In general, the mode pattern depends on the core radius ( $a$ ) and refractive index contrast between core and cladding ( $\Delta = \frac{n_1^2 - n_2^2}{2n_1^2}$ ), we considered other parameters are fixed.

In Fig. 2.2, the Electric field of the fundamental mode for a fiber with  $a = 10\mu m$  and  $\Delta = 0.0006$  is shown. It is clear that when  $\Delta \ll 1$  (Low



contrast fiber (LC)), the fundamental mode ( $|m| = 1$ ) has a uniform linear polarization with an almost Gaussian intensity pattern. The reason is that according to equations 2.7 to 2.12, the electric field of the fundamental mode is a combination of the zero and second order of the Bessel function and by considering that  $\Delta \ll 1$ , the second order can be neglected, and thus the fundamental mode is linearly polarized. In other words, the intensity is in one polarization direction. However, for high contrast (HC) single-mode, Fig. 2.3, fiber with  $a = 0.2\mu m$ ,  $\Delta = 0.401$ , the effect of  $\Delta$  in the field components is not negligible anymore and it results in the appearance of a non-uniformity in polarization profile. Besides, the intensity pattern is not a uniform Gaussian anymore and a noticeable amount of field energy goes to the cladding. For example for the odd mode, in the mentioned HC fiber we calculated that around 3.5% of the energy goes to  $x$  direction while about 96.5% is in  $y$  direction. However, for the LC fiber (odd configuration) essentially all the energy is carried in  $y$  direction. Even mode follows the same pattern in a way that for HC even mode 96.5% of energy is in the direction of  $x$  and 3.5% goes to  $y$  direction. And in LC counterpart all the energy is in  $x$  direction. Therefore, for achieving high coupling efficiency for HC single-mode fiber it is required to manipulate the polarization structure of the coupled beam appropriately, too. We discuss this in the next chapter.

When we squeeze the size of core and consequently increase  $\Delta$ , we can reach the size of a nanofiber and we see that coupling light into a nanofiber requires more consideration of polarization structure. In the following, we briefly introduce nanofibers and some of their applications.

### 2.2.2 Nanofibers

Nanofibers refer to the fibers with the core diameters in the nanometer range and have many potential applications due to their remarkable properties. Compared to a typical optical fiber (with diameter in micron), nanofibers have noticeable mechanical strength and high flexibility. It is interesting and worth mentioning that a very thin nanofiber can have a diameter as thin as 36 nm

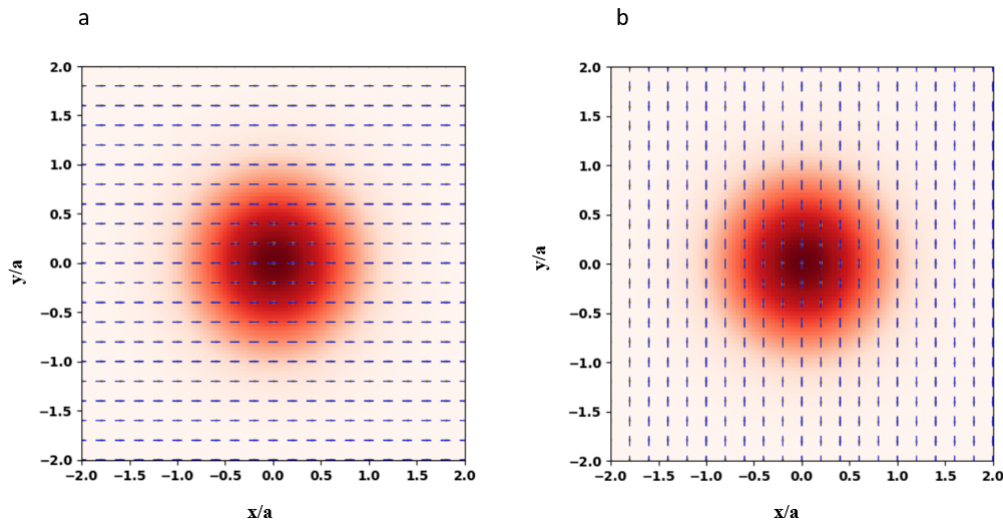


**Figure 2.2:** The almost Gaussian intensity pattern and uniform linear polarization structure of  $HE_{11}$  in a step-index optical fiber when  $\lambda = 1550 \text{ nm}$ ,  $a = 10 \text{ }\mu\text{m}$  and  $\Delta = 0.0006$ , a) for even mode, and b) odd mode.

[35]. There are plenty of applications in science and engineering for this unique type of fibers. They can be exploited in optical sensors [36, 37], quantum optics [38], tissue engineering [39], cancer diagnosis [40], and drug delivery [41], to mention some. However, the coupling efficiency is still a challenge. Interestingly, for some applications such as sensing or medicine, using structured light may lead to a better result. Therefore, the possibility of improving this efficiency by applying structured light is worth being explored.

### 2.2.2.1 Electromagnetic field in nanofibers

The tight confinement of light in nanofibers has increased the interest in them. Thus, understanding the modes in nanofibers is of huge importance. In fact, in section 2.2, we provided the complete and exact (without any approximation) electromagnetic field in an optical fiber. Although we can apply the paraxial approximation for a typical fiber mode (with micron size), nanofiber modes do not follow this approximation. In Fig. 2.3, we reported the intensity and polarization distribution of  $HE_{11}$  in a nanofiber. Nevertheless, it is of our interest to find the coupling efficiency of such fibers.

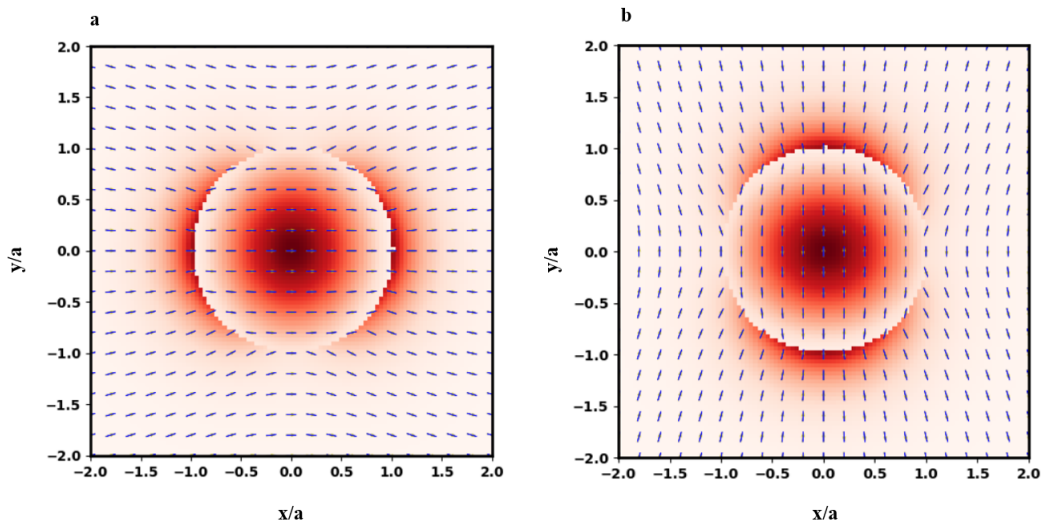


**Figure 2.3:** The intensity pattern and polarization structure of  $HE_{11}$  in a step-index optical fiber when  $\lambda = 1550 \text{ nm}$ ,  $a = 0.2 \text{ }\mu\text{m}$  and  $\Delta = 0.401$ , a) for even mode, and b) odd mode. The polarization pattern is not uniform anymore and a noticeable amount of intensity goes to the cladding.

## 2.3 Beam coupling

Even after the invention and fabrication of low-loss fibers, the coupling mechanism of a laser Gaussian beam and a specific eigen mode (of order  $m$ ) of fiber is still of huge importance. Multiple studies and activities have been done aimed at increasing the coupling efficiency. In this section we start with the coupling efficiency formulation, later we review some of the researches done by other groups and then we introduce an amplitude tailoring method to have an efficient scalar mode matching. In addition, of course, in order to couple an input beam to optical fiber mode, a suitable lens is used to focus the light into the fiber core.

Once sending the light into an optical fiber, the fiber modes will be excited. Depending on how much of the input light couples into the excited fiber mode, one can find the coupling efficiency. At first sight, coupling light into an optical fiber might seem simple and straightforward. However, having an efficient coupling needs careful consideration. To find the exact amount of coupling efficiency into an optical fiber, the exact intensity as well as polarization profile

of the fiber mode must be taken into account. However, for the sake of simplicity, in many works it is just assumed the optical fiber fundamental mode has a Gaussian pattern with uniform linear polarization. This approximation, as we shall see, is very good for low-contrast fibers but becomes less and less appropriate for increasing-contrast smaller-radius fibers.

Let us consider we have a properly focused electromagnetic field  $(\mathbf{E}, \mathbf{H})$  at the interface of an optical fiber. The coupling efficiency can be calculated as:

$$\eta = \frac{P_m}{P} + \frac{P_{-m}}{P} = \eta_m + \eta_{-m}, \quad (2.19)$$

where  $P = \langle S_z \rangle = \frac{1}{2} \iint (\mathbf{E}^* \times \mathbf{H} + \mathbf{E} \times \mathbf{H}^*) \cdot \hat{\mathbf{z}} dS$  and  $P_m = \langle S_z^m \rangle = |a_m|^2 \iint \mathbf{E}_m^* \times \mathbf{H}_m \cdot \hat{\mathbf{z}} dS$  is the power carried by the mode with total AM equal to  $m$ . The coupling coefficient  $a_m$  can be defined as:

$$a_m = \frac{\iint \mathbf{E}_m^* \times \mathbf{H} \cdot \hat{\mathbf{z}} dS}{\iint \mathbf{E}_m^* \times \mathbf{H}_m \cdot \hat{\mathbf{z}} dS} = \frac{\iint \mathbf{E} \times \mathbf{H}_m^* \cdot \hat{\mathbf{z}} dS}{\iint \mathbf{E}_m \times \mathbf{H}_m^* \cdot \hat{\mathbf{z}} dS}. \quad (2.20)$$

Applying the symmetry between the modes  $m$  and  $-m$  shows that  $\mathbf{E}_m^* \times \mathbf{H}_m \cdot \hat{\mathbf{z}} = \mathbf{E}_{-m}^* \times \mathbf{H}_{-m} \cdot \hat{\mathbf{z}}$ , therefore equation 2.19 turns into:

$$\begin{aligned} \eta &= \frac{|\iint \mathbf{E}_m^* \times \mathbf{H} \cdot \hat{\mathbf{z}} dS|^2 + |\iint \mathbf{E}_{-m}^* \times \mathbf{H} \cdot \hat{\mathbf{z}} dS|^2}{\iint \mathbf{E}_m^* \times \mathbf{H}_m \cdot \hat{\mathbf{z}} dS \cdot \iint \mathbf{E}^* \times \mathbf{H} \cdot \hat{\mathbf{z}} dS} \\ &= \frac{|\iint \mathbf{E} \times \mathbf{H}_m^* \cdot \hat{\mathbf{z}} dS|^2 + |\iint \mathbf{E} \times \mathbf{H}_{-m}^* \cdot \hat{\mathbf{z}} dS|^2}{\iint \mathbf{E}_m^* \times \mathbf{H}_m \cdot \hat{\mathbf{z}} dS \cdot \iint \mathbf{E}^* \times \mathbf{H} \cdot \hat{\mathbf{z}} dS}. \end{aligned} \quad (2.21)$$

Doing some more algebra and applying paraxial approximation, we can find a close form for the coupling efficiency as:

$$\eta = \frac{|\int \mathbf{E}_{fiber}^*(x, y) \cdot \mathbf{E}(x, y) dx dy|^2}{\iint |\mathbf{E}(x, y)|_{fiber}^2 dx dy \iint |\mathbf{E}(x, y)|^2 dx dy}, \quad (2.22)$$

where  $\mathbf{E}_{fiber}$  and  $\mathbf{E}$  are the electric field of fiber mode and the input beam, respectively.  $\mathbf{E}_{fiber}$  can be written as superposition of mode  $m$  and  $-m$  as:

$$\mathbf{E}_{fiber} = a_m \mathbf{E}_m + a_{-m} \mathbf{E}_{-m}, \quad (2.23)$$

where,  $|a_m|^2 + |a_{-m}|^2 = 1$ .

By considering an input beam with a uniform polarization like  $\mathbf{E} = E\hat{\mathbf{e}}$  where  $\hat{\mathbf{e}} = (\hat{e}_x, \hat{e}_y)$ , and using Eqs.2.15 and 2.22 and applying the symmetry between the modes with opposite AM, the coupling efficiency becomes:

$$\eta = \frac{|\int (E_r^m(r) - iE_\phi^m(r))E(r)rdr|^2}{2(\int (|E_r^m(r)|^2 + |E_\phi^m(r)|^2))rdr(\int |E|^2rdr)} \quad (2.24)$$

The equation 2.24 shows that the coupling efficiency does not depend on the state of polarization (SOP) of the input beam, as long as it is uniform across the beam cross-section. Therefore, when using an input with uniform polarization for coupling the light, we can only optimize the amplitude profile but not the polarization. In the following, we consider the amplitude matching between an incident beam and  $HE_{11}$ . In the next chapter we consider the more general case of space-varying polarization of the input beam and we will explain how to use a tool called q-plate to manipulate the amplitude and polarization of the beam to perfectly match  $HE_{11}$ .

### 2.3.1 Scalar mode matching

The coupling of light into an optical fiber can be categorized into coupling into multi-mode fibers and single-mode fibers, and thus different approaches should be used for each. Here, we only focus on the problem of coupling light into a single-mode step-index optical fiber. In this case, we need to overcome the problem of mode matching between the incident laser Gaussian beam and the fundamental mode of the fiber  $HE_{11}$ .

In section 3.2 we have explained the properties and behavior of modes in step-index fibers, in particular the fundamental mode  $HE_{11}$ . According to Fig. 2.2, the fundamental mode has a nearly uniform linear polarization over the core and cladding regions. However, we can prove it by the Stokes parameters of the fiber modes. Here we give information about the polarization state of the "even" and "odd" modes. Using various references such as Cartesian (x and y), cylindrical (r and  $\phi$ ), and circular polarization basis ( $\sigma$  and  $-\sigma$ ), we

can show:

$$S_0 = |E_x|^2 + |E_y|^2 = |E_r|^2 + |E_\phi|^2 = |E_\sigma|^2 + |E_{-\sigma}|^2 \quad (2.25a)$$

$$S_1 = |E_x|^2 - |E_y|^2 = (|E_r|^2 - |E_\phi|^2) \cos 2\phi - 2\text{Re}(E_r^* E_\phi) \sin 2\phi = 2\text{Re}(E_\sigma^* E_{-\sigma}) \quad (2.25b)$$

$$S_2 = 2\text{Re}(E_x^* E_y) = (|E_r|^2 - |E_\phi|^2) \sin 2\phi + 2\text{Re}(E_r^* E_\phi) \cos 2\phi = 2\sigma \text{Im}(E_\sigma^* E_{-\sigma}) \quad (2.25c)$$

$$S_3 = 2\text{Im}(E_x^* E_y) = 2\text{Im}(E_r^* E_\phi) = \sigma (|E_\sigma|^2 - |E_{-\sigma}|^2). \quad (2.25d)$$

According to the equation 2.16, the Stokes parameters of the  $m^{\text{th}}$  mode of an optical fiber can be written as follows:

$$S_0 = |E_r^m(r) - iE_\phi^m(r)|^2 + |E_r^m(r) + iE_\phi^m(r)|^2 = 2(|E_r^m(r)|^2 + |E_\phi^m(r)|^2) \quad (2.26a)$$

$$S_1 = -2\text{Re}(E_\sigma^* E_{-\sigma}) = 2 \cos 2\phi (|E_r^m(r)|^2 + |E_\phi^m(r)|^2) \quad (2.26b)$$

$$S_2 = -2\text{Im}(E_\sigma^* E_{-\sigma}) = 2 \sin 2\phi (|E_r^m(r)|^2 + |E_\phi^m(r)|^2) \quad (2.26c)$$

$$S_3 = |E_{-\sigma}|^2 - |E_\sigma|^2 = 4\text{Im}(E_r^m(r)^* E_\phi^m(r)). \quad (2.26d)$$

Then, normalized Stokes parameters are:

$$\begin{pmatrix} s_0 \\ s_1 \\ s_2 \\ s_3 \end{pmatrix} = \begin{pmatrix} S_0/S_0 \\ S_1/S_0 \\ S_2/S_0 \\ S_3/S_0 \end{pmatrix} = 2 \begin{pmatrix} 1 \\ \cos 2\phi \\ \sin 2\phi \\ 2 \frac{\text{Im}(E_r^m(r)^* E_\phi^m(r))}{|E_r^m(r)|^2 + |E_\phi^m(r)|^2} \end{pmatrix}. \quad (2.27)$$

Finally, applying the symmetry between modes  $m$  and  $-m$  results in:

$$\begin{cases} S_0^m = S_0^{-m} \\ S_1^m = S_1^{-m} \\ S_2^m = S_2^{-m} \\ S_3^m = -S_3^{-m} \end{cases} \quad (2.28)$$

Using the above definitions, it can be shown that the "even" and "odd" modes are linearly polarized since  $S_3$  is zero for both the electric and magnetic components. Interestingly,  $HE_{11}$  shows very nearly uniform linear polarization with approximately Gaussian amplitude in the case of LC fibers. Thus, the most favorable light that can be coupled into an LC fiber is the fundamental mode of a laser source. In Fig. 2.5 (panel a) we have compared the amplitude of the fundamental fiber mode  $HE_{11}$  with a correctly focused Gaussian beam. It is clear that they have similar amplitudes.

To proceed, suppose we have a uniformly polarized Gaussian beam  $\mathbf{E}(r) = e^{-r^2/w_0^2}(\hat{\mathbf{e}}_x + \hat{\mathbf{e}}_y)$  with a suitable beam waist  $w_0$  at the interface of the fiber as our input beam. To efficiently couple light into the fiber, the beam waist must be centered on the fiber core and have the size of the fiber mode field diameter (MFD). MFD describes the size of the beam profile within the fiber. By using a suitable lens, one can focus the input beam with the beam waist  $w_0 = \text{MFD}$ . Nevertheless, it has been demonstrated in a large number of studies that efficient coupling into  $HE_{11}$  is possible if the input beam is properly focused and centered on the fiber core [42, 43]. We have also theoretically shown that a Gaussian beam can be coupled into the aforementioned LC fiber with a maximal efficiency of 99.66%. However, when we move from the LC fiber to the mentioned HC fiber, the coupling efficiency decreases to 89.65%. Many studies have focused only on sending a Gaussian beam into optical fibers. Nevertheless, the coupling efficiency can be increased by manipulating the input beam amplitude and polarization spatial profiles. In Section 2.3.2, we show how we can improve to some extent the mode matching and hence the coupling efficiency for HC fibers just by changing the input amplitude profile.

In Fig. 2.4, we have shown how the coupling efficiency depends on the beam waist ( $w_0$ ) of the Gaussian beam. For the appropriate beam waist, the red curve corresponding to the coupling efficiency for an LC fiber is higher than the blue curve showing the efficiency for an HC fiber. The decrease in coupling efficiency is due to an increased mismatch between the amplitude distribution and polarization structure of the Gaussian beam and the fundamental mode

of the HC fiber.

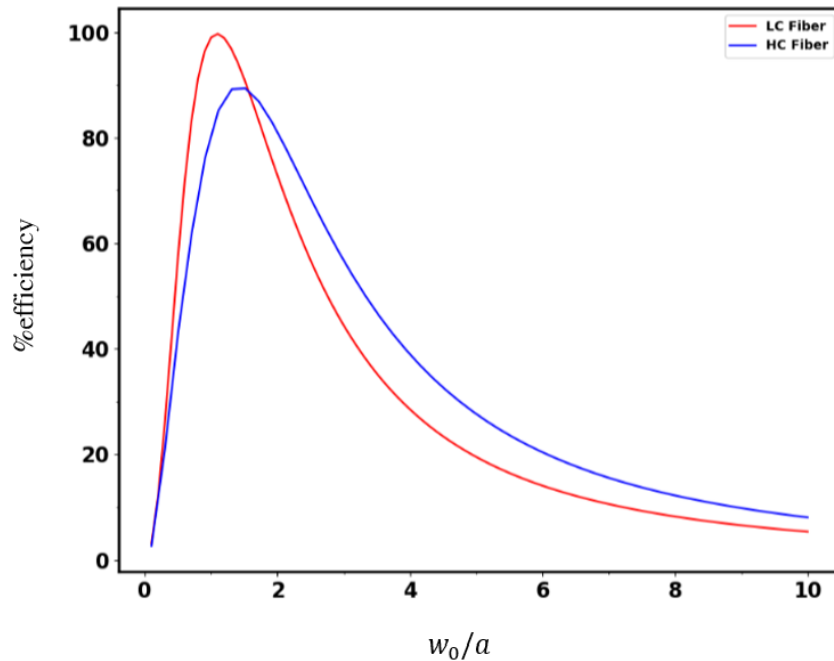


**Figure 2.4:** Coupling efficiency,  $\eta$ , between a uniformly polarized Gaussian input beam and the fundamental mode of a single-mode step-index fiber. The red curve shows  $\eta$  for a LC fiber with  $\Delta = 0.0006$ ,  $a = 10\mu\text{m}$  and the blue curve shows  $\eta$  for a HC single-mode fiber at  $\Delta = 0.401$ , and  $a = 0.2\mu\text{m}$ . It is proved that we have the maximum efficiency when the beam waist is close to the mode field diameter.

### 2.3.2 Improved scalar mode matching

Here we propose a method based solely on complex amplitude profile shaping to improve the coupling efficiency into an HC fiber. From Fig. 2.3 we see that a non-uniformity occurs in the fundamental mode intensity and polarization distribution of a single-mode nanofiber (HC fiber). In this case, a Gaussian amplitude with uniform polarization is no longer suitable. Therefore, one should modify the input beam structure. Here, we only focus on amplitude shaping, although polarization matching also plays a significant role in this case, as we shall discuss in the next Chapter.

To proceed, let us find the best complex amplitude profile matching for the fundamental mode in an HC single-mode fiber. Equation 2.24 shows that the



coupling efficiency is maximized when the input beam has a complex amplitude equal to  $E_r^m - iE_\phi^m$ . We call this "effective amplitude"  $EA$ . This  $EA$  may be the best fit for the fiber modes in the case of scalar mode matching since it is composed of the electric field components of the fiber modes. We call it scalar mode matching since it only refers to amplitude matching and has nothing to do with polarization (vector contribution of the fields). Using  $EA$ , we show, for example, that the maximal coupling efficiency may be improved from 89.65% to 92%, for the considered HC fiber having refractive index contrast  $\Delta = 0.401$ .

In Fig. 2.5, we compare the Gaussian amplitude profile, the  $EA$ , and the optical fiber fundamental mode for the mentioned HC and LC fibers. As can be seen, in the LC optical fiber, all amplitudes overlap, while in the HC fiber, the Gaussian amplitude is very different from  $HE_{11}$ . Then, in Fig. 2.6 we report the computed coupling efficiency of a Gaussian beam and  $EA$  to  $HE_{11}$ . The Gaussian input experiences a larger decrease in efficiency than  $EA$ , as the index contrast  $\Delta$  is increased. The reason is due to the increasing mode mismatch.

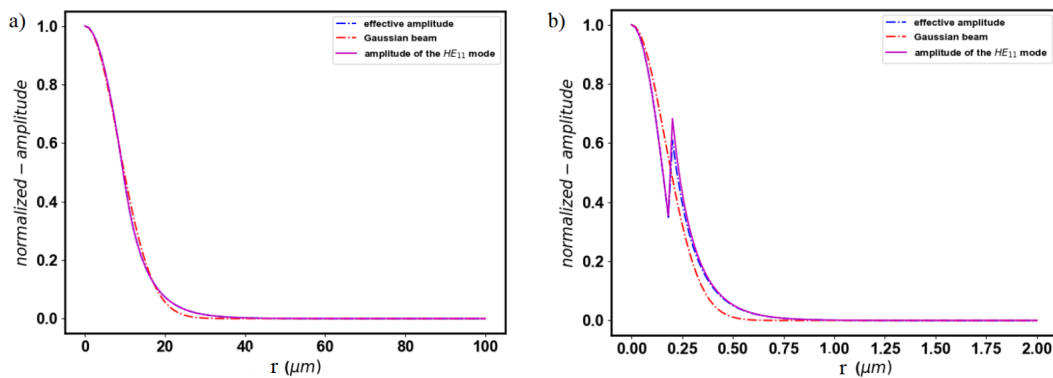


**Figure 2.5:** Comparison between the normalized amplitude of a Gaussian beam, the effective amplitude, and  $HE_{11}$  a) LC fiber, b) HC fiber. In the LC fiber, almost all amplitudes match perfectly, while in the HC fiber, the Gaussian amplitude is not close to the fundamental mode.

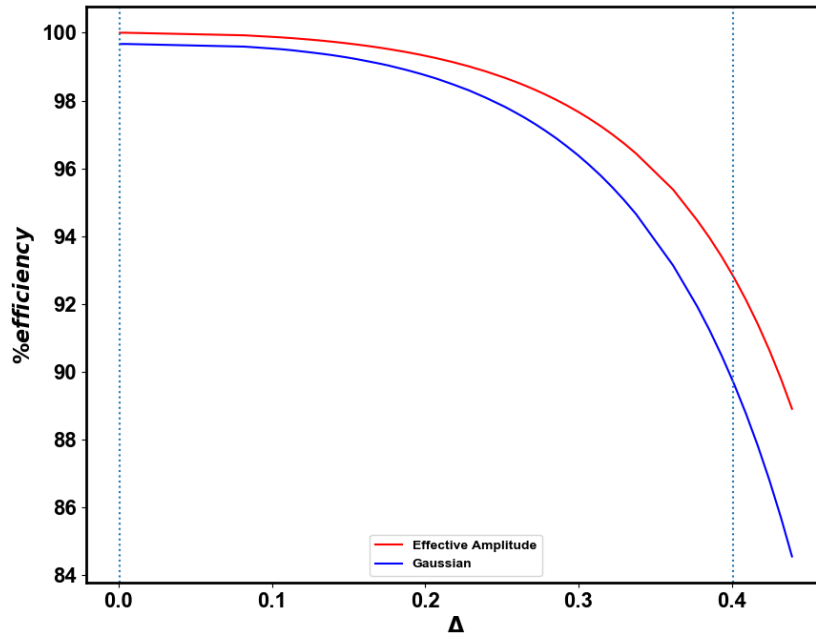


**Figure 2.6:** Comparison between the coupling efficiency,  $\eta$ , of a uniformly polarized Gaussian input beam and the effective amplitude profile, as a function of the index contrast  $\Delta$ . The coupling to the two mentioned HC and LC fibers are also shown by dashed lines. The effective amplitude always has a higher coupling efficiency. It can be seen that, as the refractive index contrast increases, the difference between the two efficiencies increases, proving the importance of amplitude matching.

To conclude this chapter, we can claim that one can improve the coupling efficiency to the fundamental mode of a single-mode step-index optical fiber by just properly tailoring the amplitude profile of the input beam, while keeping a uniform polarization. We name this "scalar mode matching". However, to achieve the highest possible value for efficiency, we need to design a device that manipulates also the polarization pattern of the input beam and matches it to the fiber mode. In the next chapter, we present a novel application for the q-plate to achieve such goal. In this case, we can not only achieve maximum efficiency but also benefit from sending structured light into the fiber.

# Chapter 3

## Polarization Effects in Single Mode Fibers: Vectorial Mode Matching

### 3.1 Introduction

In Chapter 2, we demonstrated that the fundamental mode  $HE_{11}$  of a microfiber (an optical fiber with a core size in the micrometer range) can be approximated by a Gaussian beam with a uniform linear polarization state. Also, the lowest order mode of a laser has a nearly Gaussian intensity pattern. Therefore, it can be efficiently coupled to  $HE_{11}$  of a single-mode step-index fiber. We recall that the efficiency is theoretically about 99%. However, when moving from microfibers to nanofibers, the intensity and polarization profile of the modes change dramatically, since a significant amount of power goes into the cladding and a non-uniformity in the polarization structure occurs. Therefore, it is not possible anymore to approximate it with the  $TEM_{00}$  mode. One can still send a Gaussian amplitude with uniform polarization into such optical fibers, but the expected efficiency will decrease. The increasing range of applications of nanofibers make them an interesting topic for research and science, as well as for industry, and thus the issue of coupling efficiency acquires great importance.

One way to improve efficiency is to modify only the input beam amplitude to match the fundamental mode  $HE_{11}$ . However, as we showed in Chapter 2, this is not sufficient to reach very high values of efficiency since polarization matching becomes more dominant in nanofibers.

A q-plate changes the polarization state of an input beam. Therefore, it can be a promising device to manipulate the input polarization state and bring it in line with  $HE_{11}$ . In addition to mode matching, a q-plate produces structured light. There have been many studies on the generation of light carrying OAM in an optical fiber due to the many applications of guided helical modes in both classical and quantum physics. But as we will see in this chapter, the generation methods only apply to multi-mode fibers and can cause a loss in the intensity of the signal.

In the following, we will first discuss some common methods for generating helical modes in optical fibers. Then, we mention some activities performed by other groups to increase the coupling efficiency in optical fibers, especially nanofibers. Finally, we present our method, that is, the use of q-plates for optimizing the light coupling to a single-mode optical fiber.

## 3.2 Generation of light carrying OAM in optical fibers

In Chapter 1, we discussed the common techniques for producing structured light. However, they are all applied in free space. Recently, guided modes have developed great appeal in many industries and science because of their advantages. Moreover, the applications using optical fibers as a medium for propagating structured light have been the interest of several studies.

Similar to the use of mode converter lenses, this method applies the  $HG$  to  $LG$  conversion. This mode conversion occurs due to birefringence phenomena in the optical fibers. In general, birefringence occurs in anisotropic media in which the refractive index depends on the state of polarization and the direction of propagation of light [44]. As shown in Fig. 3.1, the birefringence

in an optical fiber is mainly due to the loss of cylindrical symmetry in the core. An elliptical core (due to manufacturing defects), bending, twisting, or applying pressure to a fiber section can result in an asymmetric core, and thus cause birefringence. These reasons induce internal stress in the fiber and the refractive index changes along the stress direction. Therefore, the two components of the propagated mode (with two orthogonal polarization state) experience two different refractive indices along their directions. As a result, the birefringence occurs [45, 44].

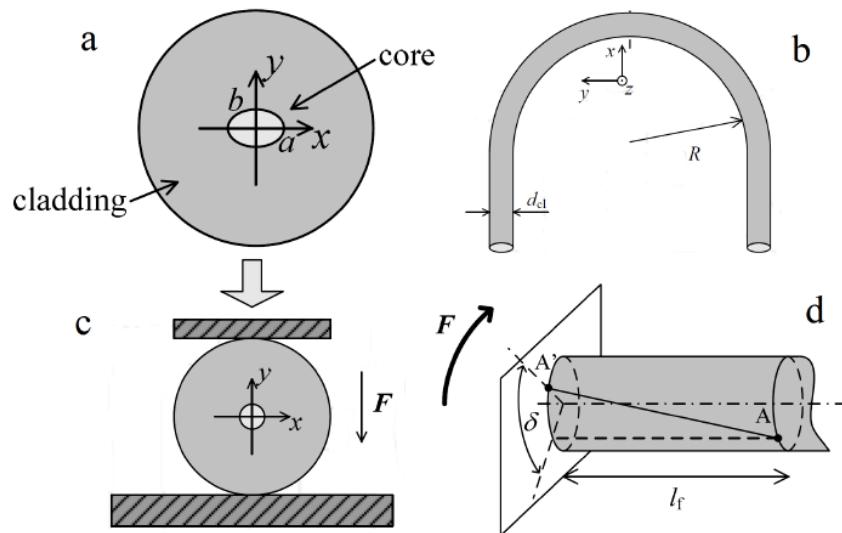


**Figure 3.1:** Schematic representation of the stresses on the optical fiber: a) elliptical core  $a$  and  $b$  are the small and large axes of the ellipse, b) bending the fiber,  $R$  is the radius of the circle generated by bending the fiber, c) external pressure produced by force  $F$ , d) twisting of the fiber (force  $F$  causes twisting (by angle  $\delta$ ) on a section of the fiber ( $l_f$ ). These stresses produce the birefringence.

### 3.2.1 Applying pressure

The exertion of varying weight is the simplest way of applying pressure on any object. Accordingly, Padgett et al. produced the desired birefringence in the fiber core by placing a weight on a section of optical fiber. In doing so, they were able to generate an  $LG$  beam with  $m = 1$  where  $m$  is the topological

charge and is related to OAM. This experiment was performed with trial and error to find the correct amount of weight. Fig. 3.2 shows their experimental setup. In this experiment, a  $HG_{10}@45$  was coupled to the optical fiber using a focusing lens. Variable loads were then applied to 100 mm of the optical fiber to exert uniform pressure on it. The required birefringence ( $\pi/2$  phase shift) was created by using 2 kg of weight. They found that by adding more loads, a  $3\pi/2$  phase shift and thus an  $LG$  mode with  $l = -1$  [46] can be produced. This work has also been done by other groups [47].

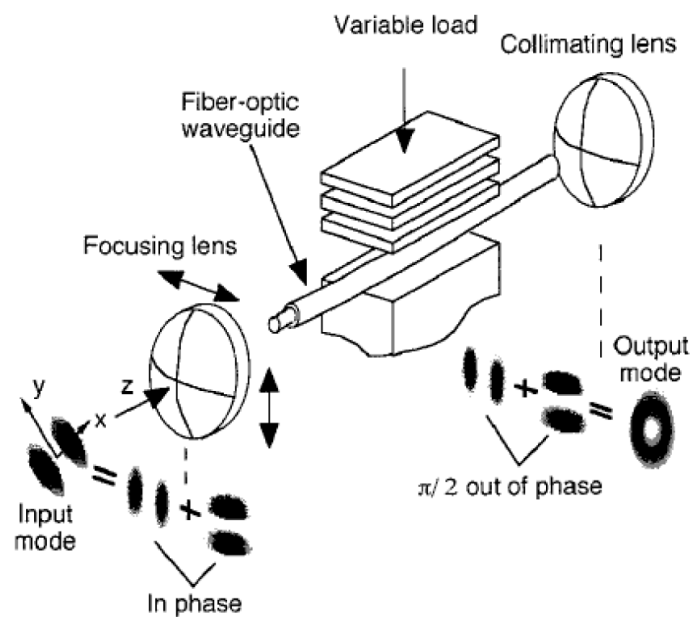


**Figure 3.2:** Generation of  $LG_{10}$  in an optical fiber. Applying pressure causes the desired phase shift equal to  $\pi/2$  between the two components of the input  $HG_{10}@45$ . The proper weight of the loads was found by repeating the experiment for different weights. The setup is adapted from [46].

### 3.2.2 Bending the fiber

Another way to create birefringence in optical fibers is to bend them with a device called "microbend grating". Fig. 3.3 illustrates an optical fiber positioned in a microbend grating. The mechanism is such that the applied stress (pressure and bending) on the embedded fiber between the displacement of the

device is suitable to produce a phase shift between the propagated  $HG$  modes in the fiber. Ref. [48] contains more details and results on this method.

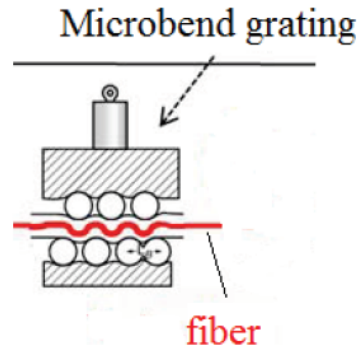


**Figure 3.3:** An optical fiber is embedded in microbend grating. External stress from this device results in the generation of OAM.

### 3.2.3 Applying acousto-optic interaction

Acousto-optics is one of the branches of physics that deals with the interaction of sound and light waves. The sound wave creates a refractive index lattice in the materials and causes the change of their refractive indices. Therefore, sending an acousto-optic wave into an optical fiber leads to the occurrence of birefringence in the core section and then to the desired phase shift between the  $HG$  modes [49].

Some more studies on OAM generation in optical fibers can be found in [50, 51, 47].

To conclude this section, it is worth mentioning that all approaches follow the same strategy, which is creating a birefringence in the core by external stress. However, this stress leads to a loss of power in the core and is therefore not a suitable approach for long-distance applications. Sending structured light into the optical fiber is a more suitable way to benefit from the helical modes in the optical fiber. The typical structured lights do not match well with the fundamental mode of the optical fibers. One has to modify the intensity pattern and polarization profile of the input beam. This is the main interest of this chapter.

Before explaining our proposal, it is worthwhile to consider the other activities aimed at improving light coupling in optical fibers, especially nanofibers.

### 3.3 Literature review of increasing coupling efficiency into optical fibers

Since the invention of optical fibers, many activities have been done to design them to have the lowest possible loss and the highest possible coupling efficiency. This section is devoted to techniques and devices that can increase the coupling efficiency between the input beam (usually the laser Gaussian beam) and the fundamental mode of single-mode step-index fibers.

Recall that in Chapter 2 we divided fibers into low-contrast (LC) and high-contrast (HC) refractive indices. The reason to increase the refractive index contrast between the core and cladding was to stay in the single-mode regime when decreasing the core size to get a nanofiber. And we are interested in single-mode fibers.

Tapered film coupling, prism coupling [52], two-beam interference [53], microlenses [54, 55], grating coupling [56] and end-fire coupling [57] are different approaches to increase efficiency. All these methods confirm high coupling efficiency in LC single-mode optical fibers. This is also shown by our simulation. The main idea of all mentioned methods is the modification of the beam amplitude leading to a scalar mode matching. In Chapter 2, we showed that the optimal scalar mode matching is provided by tailoring the input beam to have effective amplitude  $(E_r(r) - iE_\phi(r))$ , which provides the best fit to the spatial distribution of the fiber modes when the input polarization is uniform.

Let us now consider the case of HC single-mode optical fibers, which are very widely used because they have tight confined electromagnetic modes. In 2014, using a nanofiber tip, an efficiency of up to 87% was reported [58]. In 2017, a coupling efficiency of about 75% was obtained for nanophotonic devices [59]. In the same year, the coupling efficiency to a nanofiber was improved to 80%. A similar value was published in 2018 by another group [60]. Therefore,



the researchers have been working on the issue of efficient coupling in HC single-mode fibers.

All reported values for coupling efficiency into a single-mode nanofiber demonstrate the difficulties and challenges of this process.

In the next section, we show, theoretically, how a q-plate can improve efficiency to the highest possible value.

### 3.4 Polarization manipulation via q-plate

In Chapter 2, we introduced the vectorial structure of optical fiber modes. The vectorial structure is more obvious for higher order modes because they have nonuniform polarization and amplitude. Fig. 3.4 shows some higher order modes in an optical fiber. However, the fundamental mode  $HE_{11}$  is a particular case and can be used in many significant applications such as telecommunications [61, 62]. Therefore, it attracts more attention. We find that the fundamental mode in LC and HC single-mode fibers shows two different patterns. In LC fibers, the SOP structure is homogeneously distributed, and the intensity profile is almost Gaussian, which makes it more convenient and less challenging to work with LC fibers. On the other hand, HC single-mode fibers cannot be neglected because, as mentioned, they can be used in many fields. Thus, we need to design a device that modifies the vectorial structure of the input beam to match  $HE_{11}$ .

Any polarized beam can be written as a superposition of two orthogonal polarizations as  $\mathcal{A}_+(r)|\sigma^+\rangle + \mathcal{A}_-(r)|\sigma^-\rangle$ . We choose the circular polarization basis so that  $\mathcal{A}_\pm$  represents the amplitude contribution in each direction. For simplicity, we decide to use the amplitudes that depend only on  $r$  (radial distance in cylindrical coordinate) and has no dependency to  $\phi$ . In the next section, 3.4.1, we use this expression for the beam before the q-plate.

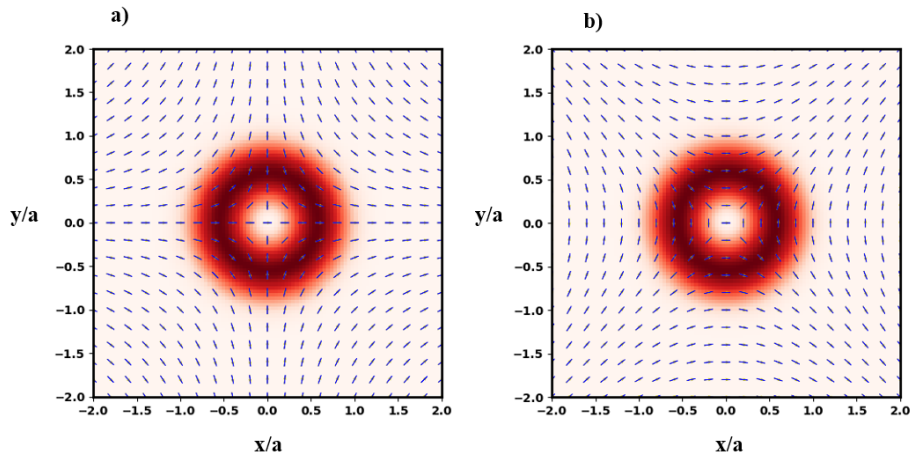


**Figure 3.4:** Intensity pattern and polarization structure of higher order modes in an LC optical fiber. a)  $HE_{21}$  odd, and b)  $HE_{21}$  even. They show a nonuniform polarization pattern.

### 3.4.1 Fiber Mode synthesis with a geometric phase plate

To get a real benefit from a q-plate, the latter should be thin enough and integrated at the fiber facet. The effect of a thin q-plate on any input beam in the near field can be then described as follows:

$$\begin{aligned} \mathcal{A}_+(r)|\sigma^+\rangle + \mathcal{A}_-(r)|\sigma^-\rangle \rightarrow & |\sigma^+\rangle(\cos(\delta/2)\mathcal{A}_+(r) + i\sin(\delta/2)e^{-2iq\phi}e^{-2i\alpha}\mathcal{A}_-(r)) \\ & + |\sigma^-\rangle(\cos(\delta/2)\mathcal{A}_-(r) + i\sin(\delta/2)e^{2iq\phi}e^{-2i\alpha}\mathcal{A}_+(r)), \end{aligned} \quad (3.1)$$

where  $q$ ,  $\delta$ , and  $\alpha$  must be chosen to result in fiber mode synthesis.

The fiber modes can be represented as the superposition of the total angular momentum  $m$  and  $-m$ :

$$a_m\mathbf{E}_m + a_{-m}\mathbf{E}_{-m}. \quad (3.2)$$

We can do a little more algebra and use the symmetry between modes with opposite total angular momentum to find the complete form for the equation

3.2 as:

$$\begin{aligned}
& a_m \mathbf{E}_m + a_{-m} \mathbf{E}_{-m} = \\
& |\sigma^+\rangle \{ a_m (E_r^m(r) - iE_\phi^m(r)) e^{i(m-\sigma)\phi} + a_{-m} (E_r^m(r) + iE_\phi^m(r)) e^{-i(m+\sigma)\phi} \} + \\
& |\sigma^-\rangle \{ a_m (E_r^m(r) + iE_\phi^m(r)) e^{i(m+\sigma)\phi} + a_{-m} (E_r^m(r) - iE_\phi^m(r)) e^{i(-m+\sigma)\phi} \}
\end{aligned} \tag{3.3}$$

where  $\sigma = \pm 1$  for right and left-handed circular polarization, respectively.

Comparing the equations 3.1 and 3.3 to match the total angular momentum (phase) and amplitude, the q-plate optimal parameters should be as follows:

$$q = 1, \tag{3.4a}$$

$$\alpha = \pi/4, \tag{3.4b}$$

$$\delta(r) = 2 \arctan \left( \frac{E_r^m(r) - iE_\phi^m(r)}{E_r^m(r) + iE_\phi^m(r)} \right). \tag{3.4c}$$

From 3.4c it can be seen that the phase retardation of the q-plate is not uniform and depends on the optical fiber parameters and the radial distance  $r$  (in cylindrical coordinate).

Moreover, in order to have the best fit, we can find the best amplitude before the q-plate as:

$$\mathcal{A}_{\pm m}(r) = a_{\pm m} \frac{E_r^m(r) - iE_\phi^m(r)}{\sqrt{2} \cos \delta/2}. \tag{3.5}$$

This is the "best amplitude" (  $BA$  ) possible before the q-plate. We should mention that the choice of the value for  $a_{\pm m}$  is optional under the condition  $|a_m|^2 + |a_{-m}|^2 = 1$ . In this case, we can propose to have  $a_m = \cos \gamma$  and  $a_{-m} = \sin \gamma e^{i\theta}$ , where  $0 < \gamma < 2\pi$  and  $0 < \theta < 2\pi$  so that all points of the Poincare sphere can be covered.

The equations 3.3, 4.4, and 3.5 are written for each mode with angular momentum  $|m|$ . Since we are interested in the fundamental mode ( $|m| = 1$ ),

we can recover it this way:

$$\begin{aligned}
& a_+ \mathbf{E}_+ + a_- \mathbf{E}_- = \\
& |\sigma^+\rangle \{a_+(E_r^+(r) - iE_\phi^m(r)) + a_-(E_r^+(r) + iE_\phi^+(r))e^{-2i\phi}\} + \\
& |\sigma^-\rangle \{a_+(E_r^+(r) + iE_\phi^+(r))e^{2i\phi} + a_-(E_r^+(r) - iE_\phi^+(r))\},
\end{aligned} \tag{3.6}$$

$$\delta(r) = 2 \tan^{-1} \left( \frac{E_r^+(r) - iE_\phi^+(r)}{E_r^+(r) + iE_\phi^+(r)} \right), \tag{3.7}$$

and,

$$A_\pm(r) = a_\pm \frac{E_r^+(r) - iE_\phi^+(r)}{\sqrt{2} \cos \delta/2}, \tag{3.8}$$

where  $E^\pm$ ,  $A_\pm$ , and  $a_\pm$  respectively stand for  $m = \pm 1$ .

Equation 3.8 is close to the effective amplitude in Chapter 2. In comparison, there is only one coefficient in the form of  $\delta$  in the  $BA$ , which is the correction of the  $EA$  for vectorial mode matching. In Fig. 3.5, we show the phase retardation of the q-plate to change the polarization of the input beam to achieve the highest coupling efficiency for the LC and HC fibers mentioned in Chapter 2. As can be seen, the change in  $\delta$  for LC fibers is about 0.07 degrees, which is very small and can be neglected. The reason is that in LC fibers, the fundamental mode has a uniform polarization state. Therefore, we can apply the (improved) scalar mode matching, and it is not necessary to manipulate the polarization structure. However, the jump in phase retardation for an HC fiber is about 80 degrees, which is expected since it proves the importance of polarization manipulation for this type of fiber.

In Fig. 3.6 we compare the best amplitude, effective amplitude, and  $HE_{11}$  for the aforementioned LC and HC fibers. In the case of the LC fiber, almost all amplitudes overlap and show a Gaussian amplitude pattern. This again shows that for high coupling efficiency, sending a uniformly polarized Gaussian amplitude is sufficient and we do not need to touch the input polarization. Interestingly, the above amplitudes also match in the HC fiber, but they show a non-Gaussian distribution; however,  $BA$  fits  $HE_{11}$  better than  $EA$ .

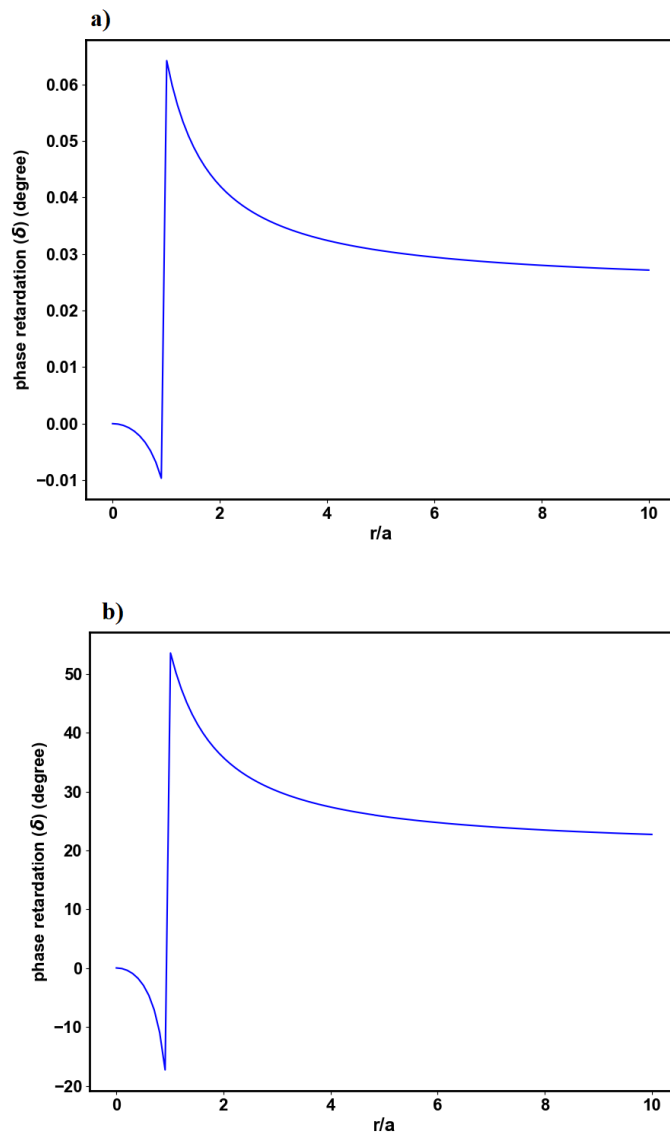


**Figure 3.5:** Phase retardation of a q-plate for input polarization modification and tuning with a) LC fiber with  $\Delta = 0.0006$  and  $a = 10 \mu\text{m}$ , and b) HC fiber with  $\Delta = 0.401$  and  $a = 0.2 \mu\text{m}$ . In the case of LC fiber, the phase retardation can be negligible.

To explain the effect of a q plate with proper parameters and suitable amplitude before that, we report Fig. 3.7. As it is clear, applying the right q-plate results in manipulating the polarization of the input beam and its profile to match the fiber modes. For example, in the mentioned HC fiber, the q-plate increases the coupling efficiency of the Gaussian beam from 89% to 96.20%, an improvement of 7.2%. The same is true for the effective amplitude with 7.5% of improvement. It is worth noting that the coupling efficiency for the

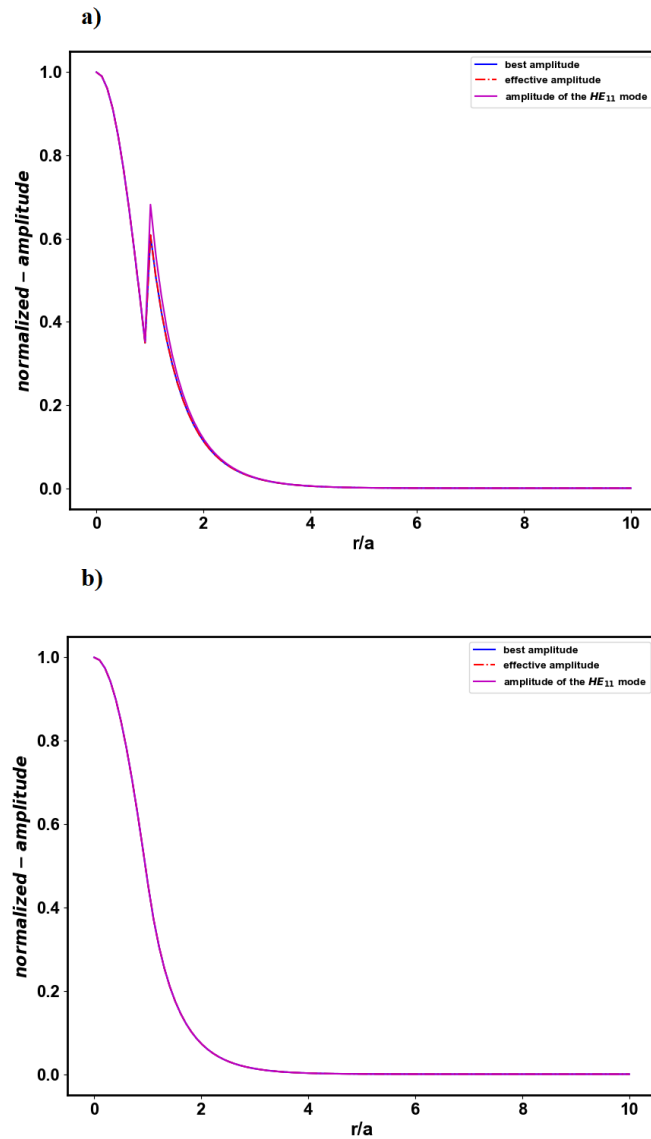


**Figure 3.6:** Normalized best amplitude, effective amplitude and  $HE_{11}$  for a) LC -fiber with  $\Delta = 0.0006$  and  $a = 10 \mu m$ , and b) HC-fiber with  $\Delta = 0.401$  and  $a = 0.2 \mu m$ . In both cases, LC and HC fiber, all amplitudes match perfectly, showing that the effective and best amplitudes are almost the same.

beam EA (red curve) and the manipulated beam GA (cyan curve) shows that by increasing the refractive index contrast, the effect of polarization matching (manipulated GA) is more significant than amplitude matching (EA).

We have gone further and tried to figure out what other amplitudes can be used before the q-plate to have efficient coupling.

The electric field after the q-plate is described using the Jones vector as

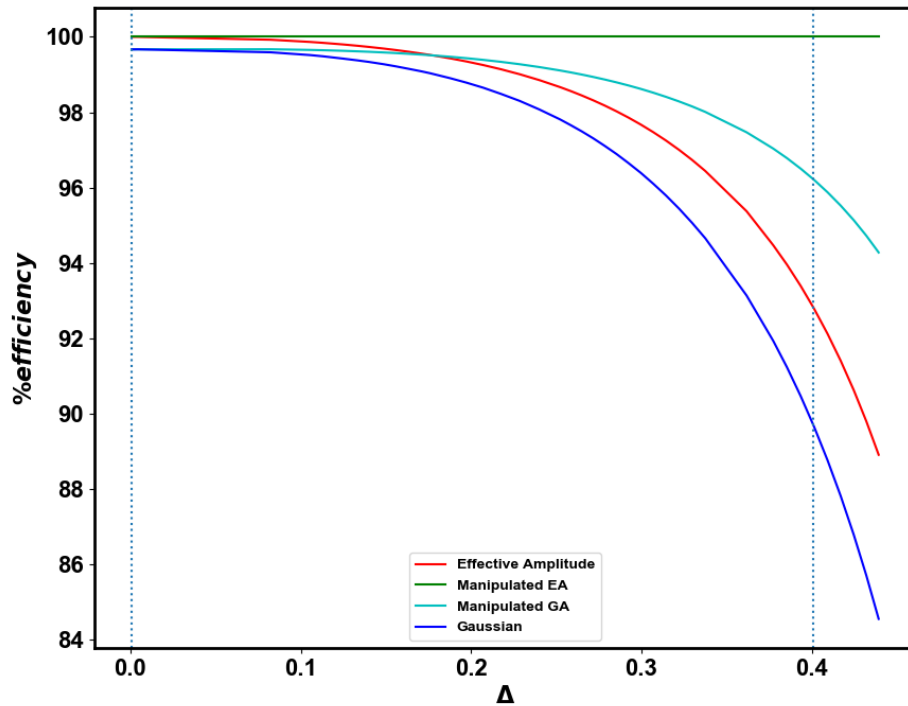


**Figure 3.7:** A comparison of the calculated coupling efficiencies for different refractive index contrasts  $\Delta$ . The dashed lines correspond to the LC fiber ( $n_1 = 1.48$ ,  $n_2 = 1.47$ , and  $a = 10 \mu m$ ) and the HC fiber ( $n_1 = 3.5$ ,  $n_2 = 1.47$ , and  $a = 0.2 \mu m$ ). The green line shows the highest coupling efficiency for any  $\Delta$  and corresponds to a manipulated  $EA$  through a suitable q-plate at the fiber facet. For the other amplitudes, there is a decrease in the coupling efficiency when going from LC to HC refractive index. However, exploiting the q-plate increases the coupling efficiency for each amplitude.

below:

$$\begin{aligned} \mathbf{J}\mathbf{E} &= \cos(\delta/2)\mathbf{E} + i \sin(\delta/2)e^{2i\alpha_0}e^{2iq\phi}|\sigma_{-}\rangle\langle\sigma_{+}|\mathbf{E}\rangle \\ &+ i \sin(\delta/2)e^{-2i\alpha_0}e^{-2iq\phi}|\sigma_{+}\rangle\langle\sigma_{-}|\mathbf{E}\rangle \end{aligned} \quad (3.9)$$

Since a q-plate can transform the input beam and synthesize the fiber modes, we assume to have the fiber modes after the q-plate. We use an inverse approach to find the optimal input before a q-plate. In this way, we can use the inverse Jones vector of the q-plate. Therefore,  $\delta$  changes to  $-\delta$ . We have shown that the fiber modes in circular basis are described by  $A_1|\sigma_{+}\rangle + A_2|\sigma_{-}\rangle$ .

The parameters of the fields are not shown explicitly. By applying the Jones vector:

$$A_1 = \cos(\delta/2)\langle\sigma_+|\mathbf{E}\rangle + i\sin(\delta/2)e^{-2i\alpha_0}e^{-2iq\phi}\langle\sigma_-|\mathbf{E}\rangle, \quad (3.10)$$

and,

$$A_2 = \cos(\delta/2)\langle\sigma_-|\mathbf{E}\rangle + i\sin(\delta/2)e^{2i\alpha_0}e^{2iq\phi}\langle\sigma_+|\mathbf{E}\rangle. \quad (3.11)$$

Substituting the fundamental mode expressions  $\mathbf{E}_+$  and  $\mathbf{E}_-$  and applying symmetry between them yields:

$$\begin{aligned} A_1 = & a_+ \left( \cos(\delta/2)(E_r^+ - iE_{phi}^+) + i\sin(\delta/2)e^{2i\alpha_0}e^{-2iq\phi}(E_r^+ + iE_{phi}^+) \right) + \\ & a_- e^{-2i\phi} \left( \cos(\delta/2)(E_r^+ + iE_{phi}^+) + i\sin(\delta/2)e^{-2i\alpha_0}e^{-2iq\phi}(E_r^+ - iE_{phi}^+) \right), \end{aligned} \quad (3.12)$$

and

$$\begin{aligned} A_2 = & a_+ e^{-2i\phi} \left( \cos(\delta/2)(E_r^+ + iE_{phi}^+) + i\sin(\delta/2)e^{2i\alpha_0}e^{-2iq\phi}(E_r^+ - iE_{phi}^+) \right) + \\ & a_- \left( \cos(\delta/2)(E_r^+ - iE_{phi}^+) + i\sin(\delta/2)e^{2i\alpha_0}e^{-2iq\phi}(E_r^+ + iE_{phi}^+) \right). \end{aligned} \quad (3.13)$$

In a general form, we can express the amplitudes  $A_1$  and  $A_2$  as:

$$A_1 = E_1(r) + E_2(r)e^{-2i\phi} \quad (3.14)$$

$$A_2 = E_3(r) + E_4(r)e^{2i\phi} \quad (3.15)$$

To find the simplest expressions for  $A_1$  and  $A_2$  we can use the Stokes parameters. For this reason, we explain more about the Stokes parameters of the fundamental mode of an optical fiber.

Stokes parameters in circular polarization basis can be written as:

$$\begin{aligned} S_0 = & |A_1|^2 + |A_2|^2 = |E_1(r)|^2 + |E_3(r)|^2 + |E_2(r)|^2 + |E_4(r)|^2 \\ & + 2\text{Re}(E_1^*(r)E_2(r) + E_3^*(r)E_4(r)e^{2i\phi}) \end{aligned} \quad (3.16)$$



$$S_1 = 2\text{Re}(A_1^*A_2) \quad (3.17)$$

$$S_2 = 2\text{Im}(A_1^*A_2) \quad (3.18)$$

$$S_3 = |A_1|^2 - |A_2|^2 = |E_1(r)|^2 - |E_3(r)|^2 + |E_2(r)|^2 - |E_4(r)|^2 \\ + 2\text{Re}(E_1^*(r)E_2(r) - E_3^*(r)E_4(r)e^{2i\phi}). \quad (3.19)$$

To have the simplest beam impinging on the q-plate, we consider that the intensity ( $S_0$ ) has no dependence on the azimuthal angle  $\phi$ . Thus,

$$E_1^*(r)E_2(r) + E_3^*(r)E_4(r)e^{2i\phi} = 0, \quad (3.20)$$

which results in:

$$E_1^*(r)E_2(r) = 0, \quad (3.21a)$$

$$E_3^*(r)E_4(r) = 0. \quad (3.21b)$$

Having the same assumption for  $S_3$ , and using equations 3.12-3.15 finally, we can find the best field before q-plate as below:

$$\mathbf{E} = E_1(r)|\sigma^+\rangle + E_3(r)|\sigma^-\rangle. \quad (3.22)$$

This may be the most general, containing both right-handed and left-handed circular polarization. However, the expressions

$$\mathbf{E} = E_2(r)|\sigma^+\rangle e^{-2i\phi}, \quad (3.23)$$

or

$$\mathbf{E} = E_4(r)|\sigma^-\rangle e^{-2i\phi}, \quad (3.24)$$

can be the other solutions for the best amplitude before q-plate.

### 3.5 Paraxial approximation validation

In this section, we will prove how we can use the paraxial approximation for the coupling efficiency equation in a nanofiber. In fact, in nanofibers, owing to the large index contrast, the back reflection of light from the fiber facet is so significant that it cannot be neglected. Therefore, in general we cannot use the paraxial approximation in this case. However, if we can prove that under certain conditions, the back-reflected light at the interface between the q-plate and the fiber facet is small enough to be neglected, the paraxial approximation is valid.

One can derive the coupled fields into the fiber as follows:

$$\vec{\mathcal{E}}_m = \vec{\mathcal{E}}_i + \vec{\mathcal{E}}_r, \quad (3.25)$$

and,

$$\vec{\mathcal{H}}_m = \vec{\mathcal{H}}_i + \vec{\mathcal{H}}_r, \quad (3.26)$$

where  $i$  represents the input beam coupling into the fiber mode, and  $r$  shows the reflected field. We have used this notation because we consider the electromagnetic field at the fiber facet as a Fourier Transform of a source field from a distance, and we need it to be fiber modes. This type of notation is common in Fourier space, and hence we use it here as well, where:

$$\mathcal{E}_m = \int e^{i(\mathbf{q}\cdot\mathbf{r})} \mathbf{E}_m \frac{d^2\mathbf{q}}{(2\pi)^2}, \quad (3.27a)$$

$$\mathcal{H}_m = \int e^{i(\mathbf{q}\cdot\mathbf{r})} \mathbf{H}_m \frac{d^2\mathbf{q}}{(2\pi)^2}. \quad (3.27b)$$

In the following, we just consider the electromagnetic field in the transverse plane ( $\perp$ ). The wavevector  $\mathbf{k}$  can be written as  $\mathbf{k} = \mathbf{k}_\perp + \hat{\mathbf{z}}k_z$ , and  $\mathbf{q} = \mathbf{k}_\perp$ .

Then using TE and TM mode division [34],

$$\boldsymbol{\mathcal{E}}_m^{TE} = \boldsymbol{\mathcal{E}}_i^{TE} + \boldsymbol{\mathcal{E}}_r^{TE} = \hat{s} \cdot \boldsymbol{\mathcal{E}}_{\perp m}, \quad (3.28a)$$

$$\boldsymbol{\mathcal{E}}_i^{TE} / \eta_{TE} - \boldsymbol{\mathcal{E}}_r^{TE} / \eta_{TE} = (\hat{z} \times \hat{s}) \cdot \boldsymbol{\mathcal{H}}_{\perp m}, \quad (3.28b)$$

$$\boldsymbol{\mathcal{E}}_m^{TM} = \boldsymbol{\mathcal{E}}_i^{TM} + \boldsymbol{\mathcal{E}}_r^{TM} = \hat{t} \cdot \boldsymbol{\mathcal{E}}_{\perp m}, \quad (3.28c)$$

$$\boldsymbol{\mathcal{E}}_i^{TM} / \eta_{TM} - \boldsymbol{\mathcal{E}}_r^{TM} / \eta_{TM} = (\hat{z} \times \hat{t}) \cdot \boldsymbol{\mathcal{H}}_{\perp m}, \quad (3.28d)$$

where  $\hat{s} = \frac{\hat{z} \times \mathbf{k}_{\perp}}{|\mathbf{k}_{\perp}|}$  and  $\hat{t} = \frac{\hat{s} \times \mathbf{k}_{\perp}}{|\mathbf{k}_{\perp}|}$  are the unit vectors along TE and TM modes, respectively and  $z$  is propagation direction.  $\eta_{TE} = \frac{\omega \mu}{k_z}$  and  $\eta_{TM} = \frac{k_z}{\omega \epsilon}$ .  $\omega$ ,  $\mu$ , and  $\epsilon$  stand for frequency, Magnetic permeability, and electric permittivity, respectively. More details are provided in ref. [63].

From 3.28a and 3.28b:

$$2\boldsymbol{\mathcal{E}}_r^{TE} = \boldsymbol{\mathcal{E}}_m^{TE} - \eta_{TE}(\hat{z} \times \hat{s}) \cdot \boldsymbol{\mathcal{H}}_{\perp m} = \hat{s} \cdot \boldsymbol{\mathcal{E}}_{\perp m} - \eta_{TE}(\hat{z} \times \hat{s}) \cdot \boldsymbol{\mathcal{H}}_{\perp m}. \quad (3.29)$$

Using equations 3.28c and 3.28d also results in:

$$2\boldsymbol{\mathcal{E}}_r^{TM} = \boldsymbol{\mathcal{E}}_m^{TM} - \eta_{TM}(\hat{z} \times \hat{t}) \cdot \boldsymbol{\mathcal{H}}_{\perp m} = \hat{t} \cdot \boldsymbol{\mathcal{E}}_{\perp m} - \eta_{TM}(\hat{z} \times \hat{t}) \cdot \boldsymbol{\mathcal{H}}_{\perp m}. \quad (3.30)$$

Combining the equations and applying Fourier Transform, the reflected field is:

$$\mathbf{E}_r = \mathbf{E}_m - \int e^{iq(r-r')} \mathbf{G}(\mathbf{q}) \mathbf{H}_m(r') dr' \frac{d^2q}{(2\pi)^2}, \quad (3.31)$$

where  $\mathbf{G}(\mathbf{q}) = \eta_{TE}(-\hat{q}) \times (\hat{z} \times \hat{q}) + \eta_{TM} \hat{q} \times (\hat{z} \times \hat{q})$  and  $\hat{q}$  is the unit vector in the direction of  $\mathbf{k}$ . In order to have the maximum coupling,  $\mathbf{E}_r$  should be minimum. Here, we assume that the q-plate is integrated at the fiber facet, thus, the only parameter which can play a role in minimization is the refractive index of the q-plate. Fig. 3.8 demonstrates when the refractive index of the q-plate is equal to the refractive index of fiber core ( $n_1$ ) we have the minimum value for reflected field which means that under this condition using the paraxial approximation is still valid.

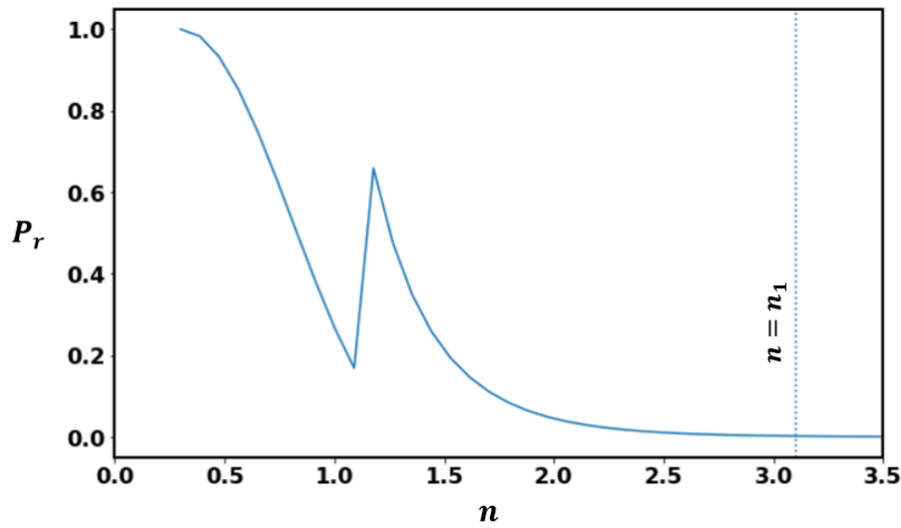


**Figure 3.8:** The normalized reflected power at the fiber interface. When the refractive index of the q-plate ( $n$ ) is equal to refractive index of core  $n_1$  (dashed line) we have the minimum reflected part and most of the light couples into the fiber mode. Here we chose the same HC fiber parameters as we chose in Chapter 2 with  $n_1 = 3.1$ .

As the conclusion we proved that applying a q-plate integrated at the fiber facet can be an effective way to improve the coupling efficiency to the fundamental mode of a nanofiber, theoretically. We demonstrated that Vectorial mode matching always results in a better coupling than scalar mode matching. Also, this method can be used for coupling light into multi-mode fibers as we showed the higher order modes do not possess homogeneous polarization distribution

# Chapter 4

## Modulated Poincare Beams<sup>1</sup>

### 4.1 Introduction

In Mathematics, a singularity is defined when a function of independent variables, such as space or time, is not well-behaved or well-defined [64]. As a simple example, consider the water in the sink drain. When the water goes down the drain, it forms a vortex and the closer it gets to the center of the vortex, the greater the velocity. At the center, this velocity ideally goes to infinity. Therefore, there can be no water in the center of the vortex which means the density of water must vanish there. So, the water vortex in the sink represents a singularity in the velocity of the water. As shown by this example, singularities also exist in physics and, more specifically, in optics as the parameters defining an electromagnetic field can be indefinite at some points. These parameters can be amplitude, phase, or polarization. In Chapter 1, we introduced the light beam carrying OAM and we realized such beams possess a phase singularity (undetermined phase) and they show a dark hole in their intensity pattern (zero amplitude). As recently, a lot of studies have been done in singular optics, this field spans from Light-matter interactions [65, 66], through telecommunications [67, 68], nonlinear optics [69, 70], and quantum communications [71, 72], to better understanding of classical and

---

<sup>1</sup>Some of the sentences or images of this chapter are adapted or copied verbatim from the work [103] which I coauthored

quantum nature of features of light.

Generating twisted beams which carry orbital angular momentum (OAM) is an example of tailoring beam amplitude and adding phase singularity to it, as discussed in Chapter 1. Besides phase singularity, there are also polarization singularities which are the main focus of this chapter. Polarization singularity refers to the condition in which any of the polarization components is not well-behaved [73]. One can benefit from helical beams with phase singularity to obtain polarization singularity. This feature of light can be found in non-uniform polarization distributions across the beam cross section [74]. Wide range of applications in edge enhancement [75, 76], robust beam [77], tight focusing [78], astronomy [79, 80], data communications [71], and biology [74], to mention some, are the proof for the huge interest towards polarization singularities generation and detection methods.

In this chapter, we are concerned with the polarization singularities that may be induced starting from a uniform polarized input beam which is Gaussian laser beam. We present a general method to engineer inhomogeneously polarized beams (IPBs) in which the rotation rate of the local polarization azimuth around singularities known as C-points or V-points can be set as desired and realized in practice without resorting to computational approximations. The design procedure lies on the same geometric approach applied for the generation of Free Form Dark Hollow (FFDH) beams [81]. In this way, we can tailor the wavefront of the spatial modes such that it produces the desired polarization distribution without passing through the direct manipulation of the orbital angular momentum (OAM) spectrum. Our technique is based on engineering liquid crystal based Spatially Varying Axes retardation wave-Plates (SVAPs), which are devices which generalize the q-plate concept. In Chapter 1, we introduced q-plate as the most common SVAP which can generate phase singularity through spin-orbit coupling. Interestingly, it was demonstrated that a typical q-plate can lead to polarization singularities generation, as well [82, 83, 84, 85]. A SVAP, in fact, can be operated so as to directly imprint the LC optic axis distribution onto the topographic map of the po-

larization azimuth, over the whole transverse cross section of the transmitted laser beam. Using this approach, there is no need to exploit an interferometer optical setup. This makes our method unique in its straightforward simplicity. The azimuth orientation information is actually encoded in the SVAP in the form of Pancharatnam-Berry phase. In principle, the same could be done by Spatial Light Modulator (SLM). Considering the need of the interferometry and high cost of SLM, however, this method is not as straight and convenient as our approach. Moreover, we proved that our SVAPs can generate both C-point and V-point singularities and any other complex structured polarization distribution desired. Moreover, this method can also give rise to generation of complex and exotic intensity patterns.

To begin with, we introduce polarization singularities in more detail and review some of their generation methods. Then, we provide a solid theory to explain the generation of IPBs with nonuniform azimuthal rotation rate. Also, we present the mathematical operation of SVAPs on the input beam to generate different non-uniform polarization structure. Finally, we show experimentally the results of passing a light beam through our SVAPs.

## 4.2 Phase singularity and polarization singularity

Polarization is one of the main features of a light beam. Elliptical polarization is the most general form while linear and circular polarizations are two important special cases [13].

Certain animals or plants can identify the polarized light or even exploit it as a signal. As an example, some sea creatures like a certain type of shrimp can reflect a specific pattern with circular polarization [86]. Some other animals or insects use the polarization of light to navigate [87]. Thus, working on animal sensitivity to the polarization of light has attracted huge attention in biology [88, 89].

When a beam has a uniform polarization across its cross-section, it repre-

sents a homogeneously polarized beam such as circularly and linearly polarized beams. As they have the same state of polarization at all the points, one can refer to them by a point in the Poincaré sphere, as we discussed in Chapter 1. However, inhomogeneously polarized light is described when the SOP of light changes across the beam cross-section [90]. Polarization singularity is linked to the non-uniform distribution of polarization. They show slowly spatially varying distribution of polarization. We recall that in Chapter 1, we discussed the polarization of electromagnetic fields, and we realized that the state of polarization of an electromagnetic field can be described by four parameters called Stokes parameters,  $S_i$  where  $i = 0, 1, 2, 3$  [91]. Thus, using Stokes parameters is a suitable way to describe the polarization singularities. To obtain these values, we need the components of intensity in horizontal, vertical, diagonal, anti-diagonal, and right and left-handed circular configurations [92]. There are two other parameters, ellipticity ( $\kappa$ ) and orientation of the polarization ellipse ( $\gamma$ ), which are linked to the SOP of light and are important to understand the polarization singularities. One can relate them to the Stokes parameters as:

$$\gamma = \frac{1}{2} \arctan\left(\frac{S_2}{S_1}\right), \quad (4.1a)$$

$$\kappa = \frac{1}{2} \arcsin\left(\frac{S_3}{S_0}\right). \quad (4.1b)$$

Since polarization singularities arise from superpositions of OAM states (phase singularities) in orthogonal circular polarization basis [74], we briefly review phase singularities. Here, we use circular polarization basis where  $|R\rangle$  and  $|L\rangle$  represent the unit vectors of right and left-handed circular polarization. As mentioned in Chapter 1, a general form to describe the spatial distribution of a vortex beam is  $E(r)e^{im\phi}$ , where  $m$ , the topological charge, can take any integer value and is defined as [93, 94]:

$$m = \frac{1}{2\pi} \oint \nabla\psi \cdot dl, \quad (4.2)$$

where  $dl$  describes the path of integration which is a (closed) curve around the singularity point and  $\psi$  is the phase of the field at each point and is



defined modulo  $2\pi$ . Now, superimposing two vortex beams with orthogonal right and left handed circular polarizations results in generation of polarization singularity as follows:

$$\mathbf{E}(\mathbf{r}, \phi) = \hat{\mathbf{e}}_R E_R(r) e^{im_1\phi} + \hat{\mathbf{e}}_L E_L(r) e^{im_2\phi}, \quad (4.3)$$

The two main polarization singularities discussed in this chapter are called ellipse fields and vector fields. Ellipse fields singularities correspond to inhomogeneously polarized fields with elliptical state of polarizations. However, linear SOP can also exist, but only at some isolated points. Therefore, in general  $S_3(x, y) \neq 0$ . In other words, it occurs when in the equation 4.3  $E_R \neq E_L$  and  $m_1 \neq m_2$ .

In ellipse fields, points corresponding to an undefined ellipse orientation are called C-points. In the far field pattern of a C-point, there is a circular state of polarization that is surrounded by elliptical state of polarization. The orientation of these ellipses can be clockwise or counterclockwise which can be defined by the polarization singularity index as:

$$I_c = \frac{1}{2\pi} \oint_c \nabla \gamma \cdot d\mathbf{l}, \quad (4.4)$$

where  $\gamma$  is defined only modulo  $\pi$  and hence  $I_c$  can be integer or half integer. The lowest value for polarization index can be  $\pm\frac{1}{2}$  where plus and minus correspond to clockwise and counterclockwise, respectively. In addition to orientation and ellipticity, ellipses can form various patterns around the singular point. These patterns are divided into three cases called "lemon", "star", and "monstar". Among them, monstar is the rarest form. By definition, star has a negative index while lemon and monstar have positive ones. We have shown lemon, star, and monstar polarization configurations for  $|I_c| = 1/2$  in Fig. 4.1. It can be seen that the polarization distribution in the neighborhood of each C-point (around a closed smooth path) has a specific orientation and distribution of ellipses. Specifically, one can define the number of radial lines (shown in red in Fig. 4.1) in each pattern. Radial lines are lines which start from singularity point where the orientation of the polarization ellipse is radial, i.e.,

$\gamma = \phi$  where  $\phi$  denotes the azimuthal angle. According to Fig. 4.1a, star configuration has three radial lines, while lemon 4.1b has only one. However, for the same value of  $I_c = 1/2$  (as lemon) monstar 4.1c consists of three radial lines.

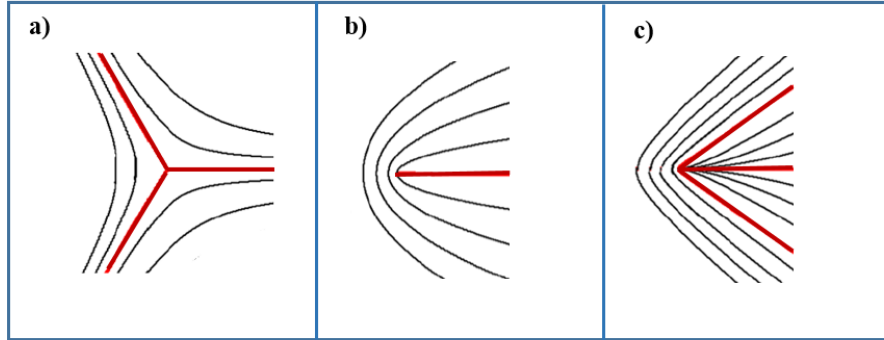


**Figure 4.1:** Polarization pattern (more precisely the lines give the orientation of the ellipse major axis at each point) of three classes of C-points when  $|I_c| = \frac{1}{2}$ . a) star with  $I_c = \frac{-1}{2}$  and three radial lines, b) lemon  $I_c = \frac{1}{2}$  and only one radial line, and c) monstar  $I_c = \frac{1}{2}$  and three radial lines. The number of radial lines distinguishes between lemon and monstar.

On the other hand, vector field singularities occur when the local polarization state is almost everywhere predominantly linear,  $S_3(x, y) = 0$ . Mathematically, this occurs when  $E_R = E_L$  and  $m_1 = -m_2$ . Singularities of vector fields are called V-points. In V-points both the polarization azimuth and handedness are indeterminate and thus the field itself must vanish. To calculate the polarization singularity index for a V-point ( $\eta$ ), called Poincaré-Hopf index, one follows the same strategy as for the C-point:

$$\eta = \frac{1}{2\pi} \oint_c \nabla \gamma dl, \quad (4.5)$$

where  $\eta$  is index of V-point. V-point is surrounded by linear polarization and  $\eta$  can take only integer values [95, 96].

### 4.2.1 Conversion between lemon and star

Interestingly, lemon and star configurations can be easily converted into each other optically. Since they express inhomogeneous polarization states, one has

to change the state of the polarization distribution in all points simultaneously to switch from one to the other, so that the index changes sign. This means that in the equation 4.4,  $\nabla\gamma$  needs to change the sign. Let us consider the lowest index  $I_c = \pm\frac{1}{2}$ . To go from  $\frac{1}{2}$  to  $\frac{-1}{2}$ ,  $\nabla\gamma$  must change the sign. This can be achieved if one of the linear polarization components undergoes a  $\pi$  phase shift. Due to the mechanism of waveplates, a half-waveplate is a suitable tool to transform the star configuration into lemon or vice versa since it can change the ellipticity, azimuth, and sign of the index simultaneously [96, 97]. In our experiments, we used a half waveplate to switch between lemon and star, as well.

As mentioned in previous chapters, manipulating and modifying the beam spatial distribution and polarization have many scientific and industrial benefits. Therefore, here our focus is on the wavefront shaping and polarization manipulation of a light beam using SVAPs to generate polarization singularities. In fact, we studied, theoretically and experimentally, the non-uniformity of the polarization around a C-point and a V-point singularities by SVAPs based on liquid crystals. We start with introducing common approaches to generate a polarization singularity and then we present our method.

### 4.3 Techniques to generate polarization singularity of light

It goes without saying that the great potential for applications of polarization singularities in many scientific fields, as mentioned in 4.1, leads many studies to focus on their possible generation techniques. Here we discuss briefly some methods. Generally speaking, in all methods two beams with different amount of OAM interfere and generate polarization singularities.

However, there is another way for creation of these singularities which uses a Spatially Varying Axis Plates (SVAPs) based on liquid crystals [81]. We saw in Chapter 1 that the most common one is called q-plate. Using this technique one can produce any state of OAM using a simple laser beam

(mostly Gaussian). In addition, if the SVAP is not completely tuned, there will be the superposition of two beams with different state of OAM and also opposite spin angular momentum (SAM). Therefore, in a simple way, one can generate different polarization singularities such as lemon, monstar, star.

- **Interference technique**

One way to produce such beams is to interfere two orthogonal polarized beams with phase singularity. The amplitude distribution and phase singularity should be chosen properly. The Sagnac or Mach–Zehnder interferometer are the two most common configurations for the optical setup. However, there must be a device such as spiral phase plate to generate proper phase singularity (in one or both arms of the interferometer). This method requires a precise alignment of the setup as they are highly sensitive to the overlap of the vortices [98, 99].

- **Spatial light modulators**

A typical spatial light modulator (SLM) operates only to one linear polarization state and act as a mirror (reflects) for the other. In fact, this device can be used to generate phase singularities. One can benefit from this, usually in combination with some form of interferometers, to produce polarization singularities. However, SLM is costly which makes it not available in all labs [74].

- **Intra-cavity technique**

One can achieve polarization singularity by adding a polarization-selective mirror inside a laser resonator cavity. In this way, one polarization state will be blocked while the other one will be transmitted. Using this device, one can only generate a V-point. Moreover, it needs a complex technique to fabricate the device [100].

- **q-plate**

A q-plate can manipulate the polarization and spatial distribution of electromagnetic field in a way that it gives birth to a non uniformity in both polarization and amplitude profile, in the transverse plane. It can add a phase singularity to the beam and generates structured light [101, 18]. Moreover, one can produce undefined ellipticity or orientation of the polarization ellipse and hence singular polarized beam [73] called vector vortex beam. Having control on the input polarization and phase retardation of the plate, a typical q-plate can generate both C-point and V-point singularities. However, we should mention that monstar cannot be generated via a q-plate. In Fig. 4.2 we report the polarization singularity lemon generated by a q-plate with  $q = 1/2$ . More details about generating vector beam via q-plate is provided in ref. [102].

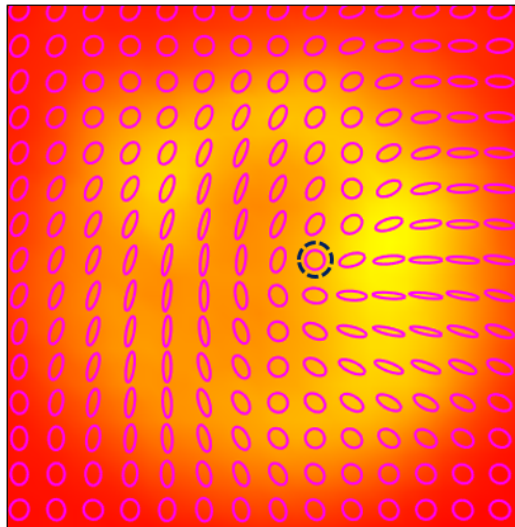


**Figure 4.2:** Intensity and polarization patterns of lemon in the near field generated by a circularly polarized input beam passed through a q-plate with  $q = 1/2$  and  $\delta = \pi/2$ . The small ellipses (orientation and ellipticity) shown in the figure are calculated from space-resolved polarization tomography. The dashed circle shows the position of the C-point singularity.

The advantage of using q-plate over an interferometric method is that all the procedure is accomplished only in one line and there is no need for in-

terferometers layouts. Also, it does not have the complexity of laser cavity technique and is less costly than spatial light modulators.

As the mechanism of q-plate and SVAP is similar, I will explain its action to generate polarization singularity with more details in the next section.

## 4.4 Generation of light beam with singularities using SVAPs

Liquid crystal-based devices such as SVAPs and in particular q-plates can be greatly beneficial in spin-orbit coupling by modifying the polarization and spatial distribution profile, as discussed. In this section we present the possibility of generating the light beams possessing phase singularity with exotic structure and landscape with such devices. To reach this goal, a technique was developed to modulate the geometric features of a desired curve into an azimuthal phase factor. In this way, one can adjust the optic axis distribution of the inhomogeneous waveplate based on liquid crystals. This plate (SVAP) can be exploited for wave front shaping via Pancharatnam-Berry phase [81]. We should mention that the input beam is simply a Gaussian laser beam.

An azimuthal mode can be written as a function of the azimuthal angle  $\phi$  as  $A(r)e^{i\psi(\phi)}$  and therefore a more general form of equation 4.3 can be represented as:

$$|IPB\rangle = c_L E_L(r, \phi, z) e^{i\psi_L(r, \phi, z)} |\hat{e}_L\rangle + c_R e^{i\alpha} E_R(r, \phi, z) e^{i\psi_R(r, \phi, z)} |\hat{e}_R\rangle, \quad (4.6)$$

where  $|IPB\rangle$  refers to the inhomogeneously polarized beams,  $z$  defines the propagation direction, and the two complex functions  $E_L(r, \phi, z) e^{i\psi_L(r, \phi, z)}$  and  $E_R(r, \phi, z) e^{i\psi_R(r, \phi, z)}$  represent the normalized scalar modes in the two orthogonally circularly-polarized states. The two coefficients  $c_L$  and  $c_R e^{i\alpha}$  also determine the contribution of each mode. The position of the state of polarization on the Poincaré sphere of such beams depends on the ratio between the two coefficients, the phase difference  $\psi_R(r, \phi, z) - \psi_L(r, \phi, z)$ , and the global phase factor  $\alpha$ . One simple method to generate an IPB mode is to superimpose two

*HG* mode with orthogonal linear polarization or two *LG* beams with orthogonal circular polarization [97]. However, our approach is to apply the designed SVAP to a single beam to generate IPB modes having the desired polarization singularities and intensity pattern. When a circularly polarized beam is passed through this device with optimal tuning, the modified intensity pattern consists of a dark hollow zone and can therefore be called a free-form dark-hollow. Here, we propose to use a nonseparable superposition of free-form helical (FFH) modes with orthogonal circular polarization to produce IPB modes [81, 103].

To continue, we discuss first the generation of free form helical modes using SVAPs. In Chapter 1 we mentioned the generation of beams with a well-defined amount of OAM using q-plates, which are a typical form of SVAPs. One can produce a free form helical spatial mode of order  $m$  and topological charge  $l$  by subjecting a helical-phase mode with topological charge  $l$  to an additional  $m$ -fold rotation-symmetric phase which is defined by a suitable curve  $\gamma$  in the plane, which can in turn be defined by the function  $\rho(\phi)$  which gives the radius of the point for each azimuthal angle  $\phi$ .

$$\rho(\phi) = \left( \left| \frac{\cos \frac{m\phi}{4}}{a} \right|^{n_2} + \left| \frac{\sin \frac{m\phi}{4}}{b} \right|^{n_3} \right)^{-\frac{1}{n_1}}, \quad (4.7)$$

where  $m$  is an integer,  $n_1$ ,  $n_2$  and  $n_3$  define the local radius of curvature, and  $a$  and  $b$  stand for the radius of circumferences, respectively inscribed and circumscribed to the curve  $\gamma_m$ . One can generate several classes of plane curves  $\gamma_m(a, b, n_1, n_2, n_3)$  of various kinds by changing only the parameters  $m$ ,  $n_1$ ,  $n_2$ ,  $n_3$  and  $a$  and  $b$  in eq. 4.7 in polar coordinates.

Fig. 4.3 illustrates the examples for the wavefront shapes of free form helical spatial mode of order  $m$  and topological charge  $l$  by the mentioned phase combinations.

In general, adding a phase factor  $e^{i2\Psi(\phi)} = e^{i\ell\Phi(\phi)}$  to a Gaussian beam will result in generation of free form helical beams, where

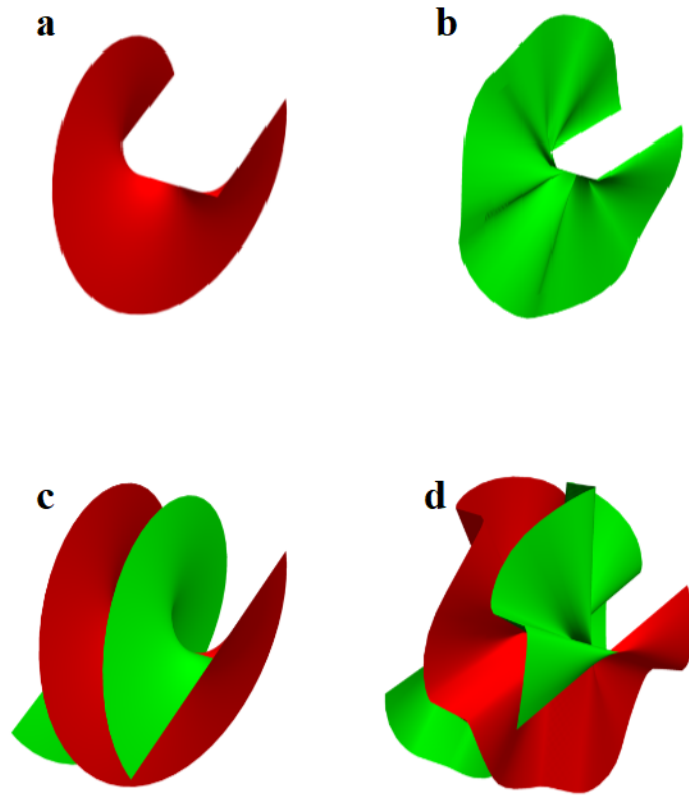


**Figure 4.3:** Demonstration of modulated vs un-modulated helical wavefronts. a) uniform helical wavefront for  $\ell = 1$  ( $\gamma_\infty$ ), (b) modulated helical wavefront for  $\ell = 1$  and  $\gamma_5(a = b, n_1 = 1/2; n_2 = n_3 = 4/3)$ , c) uniform helical wavefront for  $\ell = 2$  ( $\gamma_\infty$ ), d) modulated helical wavefront for  $\ell = 2$  and  $\gamma_6(a = b, n_1 = 2/3; n_2 = n_3 = 2.3)$  [103].

$$\cos \Phi = n_x(\phi) = \frac{\rho \cos \phi + \dot{\rho} \sin \phi}{(\dot{\rho}^2 + \rho^2)^{1/2}}, \quad (4.8a)$$

$$\sin \Phi = n_y(\phi) = \frac{\rho \sin \phi - \dot{\rho} \cos \phi}{(\dot{\rho}^2 + \rho^2)^{1/2}}, \quad (4.8b)$$

where  $\phi$  is the azimuthal angle and  $\Phi$  defines the polar angle of the unit vector  $\hat{\mathbf{n}} = (n_x, n_y)$ , which is everywhere normal to the defining curve  $\gamma$ , and  $\dot{\rho} = \frac{d\rho}{d\phi}$ .

In general, one can choose any desired curve; However, Lamé's curve can be a particularly interesting choice to be imprinted on the SVAP. The reason for this is that a Lamé's curve is a closed curve that is similar to an ellipse and retains the geometric properties (shape) of semi-major and semi-minor axes as in ellipse, but has a different shape. In polar coordinate, one can describe



it mathematically by

$$(a \cos(\phi))^{\frac{n}{n-1}} + (b \sin(\phi))^{\frac{n}{n-1}} = \rho(\phi)^{\frac{n}{n-1}}, \quad (4.9)$$

where,  $a$ ,  $b$ , and  $n$  are positive and real and describe the geometric shape of the curve. This equation is close to ellipse equation, thus they are called also superellipses [104].

The curve can be closed over an interval of  $[0, 2\pi)$  or  $[0, 4\pi)$  depending on  $m$ . If  $m$  is even the first case happens while for odd values of  $m$  the second one is the result. Any choice of the mentioned parameters creates a distinct curve and based on the needs, one can select the suitable one. As an example, for our purpose, we selected the parameters such that the intensity pattern resemble a seastar or primrose (we see the chosen parameters in the next sections).

From equations 4.8:

$$(n_x + i n_y)^\ell = \left[ \frac{\rho(\phi) - i \dot{\rho}(\phi)}{\rho(\phi) + i \dot{\rho}(\phi)} \right]^q e^{i 2q \phi} = e^{i q \bar{\psi}(\phi)} e^{i 2q \phi}, \quad (4.10)$$

and therefore, for our convenience, we can define the phase  $\Psi(\phi)$  as:

$$e^{i 2\Psi(\phi)} = (n_x + i n_y)^\ell, \quad (4.11)$$

where  $2q = \ell$ , and then clearly the phase factor is  $e^{i q \bar{\psi}(\phi)} e^{i \ell \phi}$  which is a helical phase factor multiplied by a modulation phase factor. Interestingly, the phase factor  $e^{i q \bar{\psi}(\phi)}$  is a periodic function of  $\phi$  as  $e^{i q \bar{\psi}(\phi + \frac{2\pi}{m})} = e^{i q \bar{\psi}(\phi)}$  and therefore, its Fourier expansion can be written

$$e^{i q \bar{\psi}(\phi)} = \sum_h \chi_h e^{i h m \phi}, \quad (4.12a)$$

$$\chi_h = \frac{m}{2\pi} \int_0^{\frac{2\pi}{m}} \left[ \frac{\rho(\phi) - i \dot{\rho}(\phi)}{\rho(\phi) + i \dot{\rho}(\phi)} \right]^q e^{-i h m \phi} d\phi. \quad (4.12b)$$

Thus, the OAM spectrum of an  $\ell$ -charge  $m$ -order FFH beam can take only the components with indices  $\ell \pm h m$ ,  $h$  being any integer and  $\ell = 2q$  the OAM index corresponding to the background helical mode. Using helical

mode expansion, the azimuthal phase factor in equation 4.11 can be recovered as:

$$e^{i2\Psi(\phi)} = \sum_h \chi_h e^{i(2q+hm)\phi} = \sum_l c_l e^{il\phi}, \quad (4.13)$$

where  $l = 2q + hm$ .

Doing some more algebra and using equation 4.8, the mean value of the OAM in an  $m$ -order FFH mode can be written as:

$$\langle L_z \rangle = -\frac{i\hbar}{2\pi} \int_0^{2\pi} e^{-i2\Psi(\phi)} \frac{\partial}{\partial \phi} e^{i2\Psi(\phi)} = \frac{\hbar}{\pi} \Psi(\phi)|_0^{2\pi} = \frac{\hbar}{\pi} q \Phi(\phi)|_0^{2\pi} = 2\hbar q. \quad (4.14)$$

It clearly demonstrates that the mean OAM carried by an  $\ell$ -charge FFH mode does not depend on  $m$  and is equal to  $\ell\hbar = 2q\hbar$  per photon. Interestingly, this is the value for OAM of the background helical mode. In fact, a homogeneous helical mode is a particular form of free form helical mode if the curve  $\gamma_m$  degenerates into a circumference ( $\gamma_m \rightarrow \gamma_\infty$ ).

However, it is worth to mention that FFH mode with charge  $\ell$  and order  $m$  have the symmetry as following:

Odd  $\ell$  results in invariant phase under combined charge inversion and reflection across the  $x$  axis; While, even  $\ell$  (integer  $q$ ) and even  $m$  mean phase profile is invariant under combined charge inversion and reflection across either  $x$  or  $y$  axis. And finally, even  $\ell$  and odd  $m$  indicates for invariant phase profile but only under combined charge inversion and reflection across the  $x$  axis. We should also mention that propagating in free space changes the FFH profile. However the symmetries will remain untouched.

#### 4.4.1 modulated Poincaré beams

Equation 4.6 refers to a general form of azimuthal mode. In section 4.4, we introduced FFH modes. Thus applying FFH modes as the spatial modes in equation 4.6 results in generation of a new class of optical beams with non uniform polarization distribution known as "modulated Poincaré beams" (MPBs)

as they can be considered as a generalization of ordinary Poincaré beams to the case of nonuniform azimuthal rotation rate of the polarization ellipses:

$$|MPB(m_1, q_1, \xi_1; m_2, q_2, \xi_2)\rangle = c_L FFH_{q_1}^{m_1}(\xi_1)|\hat{e}_L\rangle + c_R e^{i\alpha} FFH_{q_2}^{m_2}(\xi_2)|\hat{e}_R\rangle, \quad (4.15)$$

where  $FFH_{q_i}^{m_i}(\xi_i)$  denotes the  $m$ -order FFH mode of topological charge  $2q_i$ , corresponding to the set of parameters  $\xi_i = (a_i, b_i, n_{1i}, n_{2i}, n_{3i})$ .

## 4.5 A Free Form Azimuthal SVAP to generate modulated Poincaré beam

As mentioned in Chapter 1, using circular polarization basis, the action of the free form azimuthal SVAP ( $\hat{Q}(q, m, \xi)$ ) on an input beam can be described using Jones matrix as:

$$\begin{aligned} \hat{Q}(q, m, \xi) &= \cos \frac{\delta}{2} (|e_L\rangle \langle e_L| + |e_R\rangle \langle e_R|) \\ &+ i \sin \frac{\delta}{2} (e^{i2\Psi(\phi; q, m, \xi)} |e_R\rangle \langle e_L| + e^{-i2\Psi(\phi; q, m, \xi)} |e_L\rangle \langle e_R|) \end{aligned} \quad (4.16)$$

where the phase factor  $e^{i2\Psi(\phi; q, m, \xi)}$  is given by equation 4.11 and the phase retardation  $\delta$  appears by applying external electric field for tuning the plate. To generate different singular polarized light we consider two different cases: first with the circular polarization input and  $\delta = \pi/2$  (half-tuned) to generate C-points and the second with linear polarization input and  $\delta = \pi$  (tuned) to produce V-point singularities.

Let us consider C-point singularities generation: In this case, it is needed to shine the SVAP with circular polarization input (left or right handed) and apply the external electric field such that it induces a  $\pi/2$  phase retardation as in QWP. The generated modulated Poincaré beam will have  $q_1 = 0$ ,  $q_2 = q$ ,  $m_2 = m$ ,  $\xi_2 = \xi$ , and  $c_R/c_L = 1$ . In near field, the beam will take non uniform linear polarization distribution indicating C-point singularity at the center

with index  $I_c = q$ . Moving to V-point, it is required to change the polarization state of input beam as well as SVAP phase retardation. We demonstrated impinging a uniform linearly polarized Gaussian beam to SVAP can produce V-point if the phase retardation is  $\pi$  as in HWP, which is the case of completely tuned SVAP. Therefore, the MBP takes  $-q_1 = q_2 = q$ ,  $m_1 = m_2 = m$ , and  $\xi_1 = \xi_2 = \xi$  with the non uniform linear polarization pattern corresponding to V-point at the center. In this case the index of the singularity is  $\eta = 2q$  [103].

In Fig. 4.4, we demonstrated the intensity pattern of the beam when the input beam is circularly polarized Gaussian and the SVAPs are completely tuned,  $\delta = \pi$ .

## 4.6 detection and characterization of polarization singularities

As mentioned in section 4.4, selecting different values of parameters results in creating various curves and hence various modulated Poincaré beams. Here we provide four different SVAPs geometries called "starfish" (seastar) and "primrose". The primrose itself is designed in three different pattern to obtain various polarization singularities.

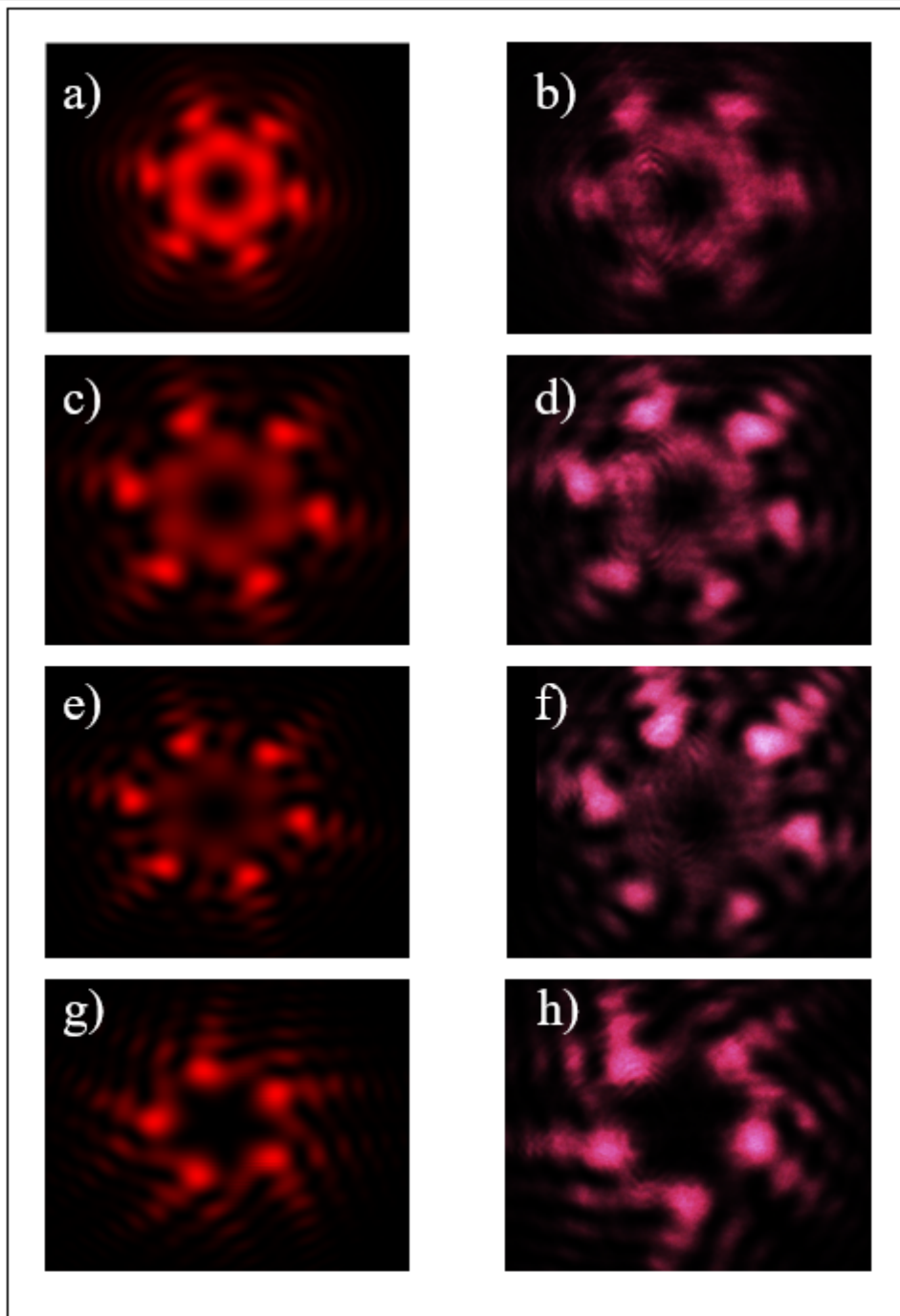
Polarimetry is a common approach to describe the state of polarization of a light beam based on a proper combination of wave plates. Thus, here, we used a space-resolved polarimetric system to describe the non-uniformity in the polarization distribution.

The experimental setup is reported in Fig. 4.5. A Helium-Neon (He-Ne) laser beam with  $TEM_{00}$  spatial mode at  $\lambda = 632.8 \text{ nm}$ , is followed by a telescope system. This procedure allows one to have a collimated beam with a uniform intensity. To have an initial linear state of polarization, we applied a linear polarizer ( $P_1$ ). This is followed by  $QWP_1$  to send a circular input into the SVAP (for C-point singularity). However, to generate linear horizontal or vertical (for V-point singularity) it is replaced by  $HWP_1$ . To adjust the angle  $\alpha = 0$  in equation 4.6 the sequence of  $HWP_2$  and  $HWP_3$  was exploited. We

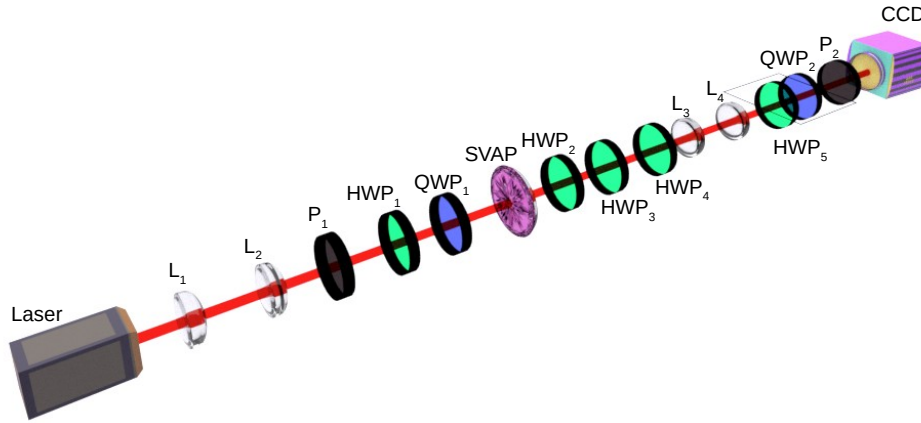
applied a  $4f$  system of lenses ( $L_2$  and  $L_3$ ) to obtain near field measurements.  $HWP_5$  or  $QWP_2$  are used to obtain the intensities needed for Stokes parameters. Finally a  $CCD$  camera is inserted to record the corresponding intensity of each state of polarization. Fig. 4.6 illustrates the examples of the recorded intensities for primrose SVAP in the near field with linear polarized input beam. As it is clear, the intensity profile of each component of the electric field is different from the others. We applied right handed circular polarization to the SVAP to generate C-point singularities and vertical and horizontal polarized beams to get V-points. We report these singularities in Fig. 4.7-4.12. The SVAPs are the mentioned starfish and primroses.  $HWP_4$  is placed to convert lemon to star and vice versa, as mentioned in section 4.2.1.

Now, let us see how to adjust  $\alpha = 0$ . We recall that SVAPs are nematic liquid-crystal cells where the alignment of molecular direction is based on the fabrication process. The director pattern, usually, may have an angular orientation related to azimuthal coordinate  $\phi$ . For simplicity, in many cases, this orientation is considered to be zero. However, there is not an exact control on it and if it is not zero the constructed pattern will undergo a rotation. In Fig. 4.13, we reported an example of rotation when  $\alpha \neq 0$ . In order to avoid that rotation, we used  $HWP_2$  and  $HWP_3$ . The relative angle of the two HWPs can be calculated by comparing the theoretical results with  $\alpha = 0$  and the experimentally reconstructed pattern. We determined the relative angle for the two HWPs for SVAPs primrose profile 1, profile 2, and profile 3 to be 21, 18, and 32 degree, respectively.

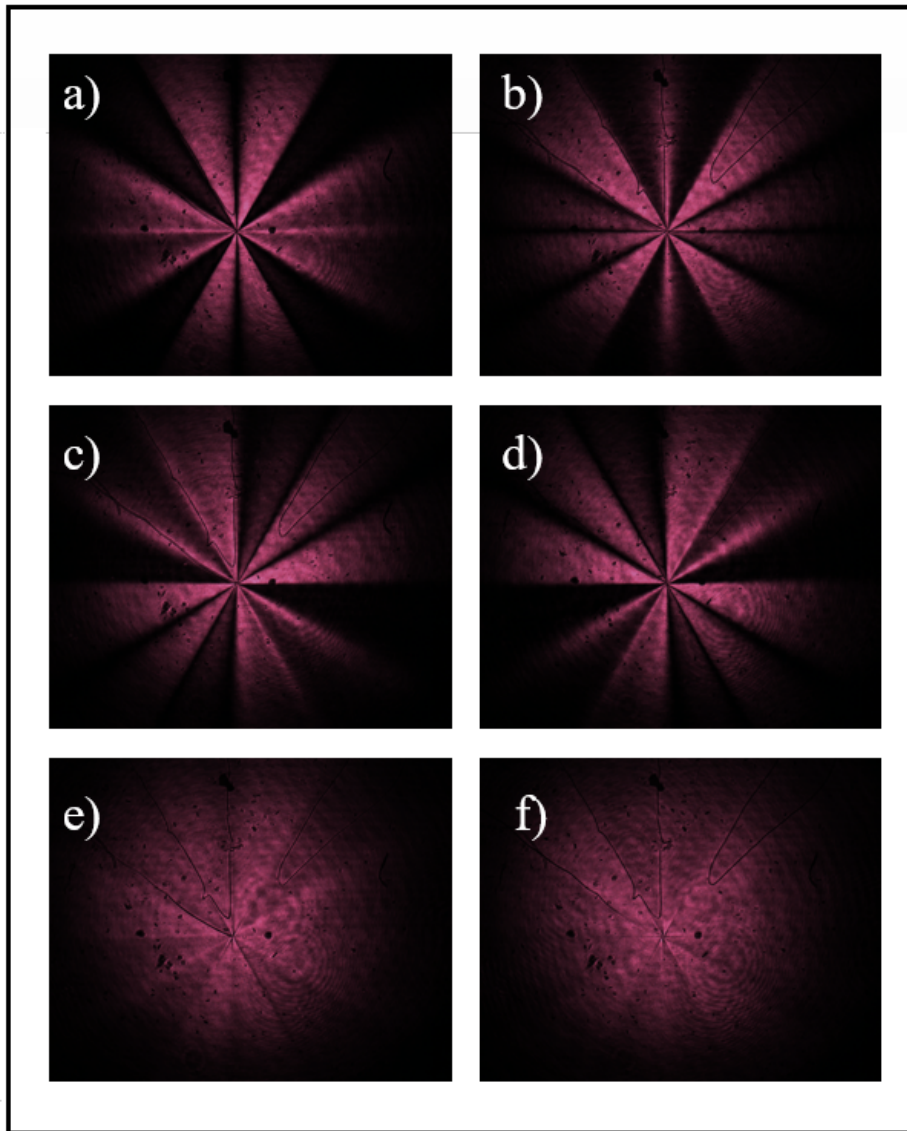
In conclusion, we have presented a direct method to generate a wide range of non uniform structured polarization distributions. The method was based on inseparable superposition of Free Form Helical modes with orthogonal right and left handed circular polarization. In fact, our approach was based on adding a phase modulation to a uniform helical mode. We proved the simplicity of our technique by applying the SVAPs in an optical setup meant for describing polarization singularity. The promising applications of such beams make our method a suitable one to be exploited.



**Figure 4.4:** A comparison between theoretical (left) and experimental results (right) for intensity profiles of the beam generated via the SVAPs for an input Gaussian beam with circular polarization. a) Primrose profile 1 with the selected curve  $\gamma_6(a = b, n_1 = 2/3; n_2 = n_3 = 2.3)$  [103], b) primrose profile 2 with the selected curve  $\gamma_6(a = b, n_1 = 3/10; n_2 = n_3 = 2.3)$  [103], c) primrose profile 3 with  $\gamma_6(a = b, n_1 = 1/6; n_2 = n_3 = 2.3)$  [103], and d) starfish SVAP with the selected curve  $\gamma_5(a = b, n_1 = 1/2; n_2 = n_3 = 4/3)$  [103].



**Figure 4.5:** Experimental setup for spatially-resolved polarimetric measurements. A telescope including the lenses  $L_1$  and  $L_2$  expands the light beam from a He-Ne laser source ( $\lambda = 632.8$  nm, maximum power output  $P_o = 5$  mW, beam waist  $w_0 = 0.5$  mm). The linear polarizer  $P_1$  and the  $QWP_1$  are used to make the input polarization circular. The latter is replaced with a half-waveplate  $HWP_1$  when the input polarization is linear horizontal or vertical. A pair of half-waveplates  $HWP_2$  and  $HWP_3$  have been inserted to precisely set the phase angle  $\alpha = 0$  in equation 4.6. Half-waveplate  $HWP_4$  is used for swapping left-/right-handed circular polarized output states, when needed. The SVAP, the lenses  $L_3$  and  $L_4$ , and the CCD camera are positioned in the  $4f$  configuration for near field measurements. A single lens is adopted for far field measurements. The half-waveplate  $HWP_3$ , the quarter-waveplate  $QWP_2$  and the linear polarizer  $P_2$  are used for measuring the local Stokes parameters over the wavefront [103].

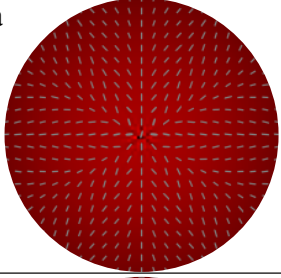
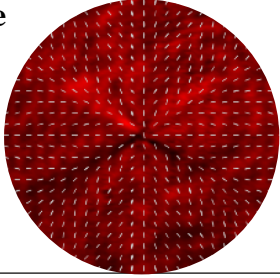
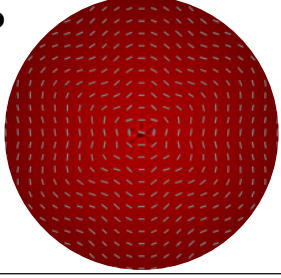
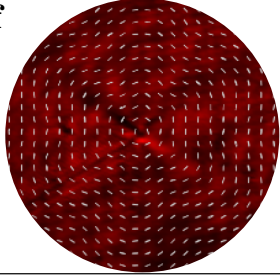
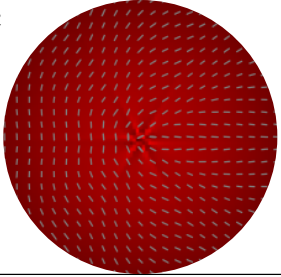
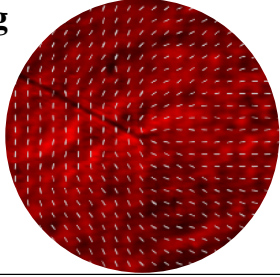
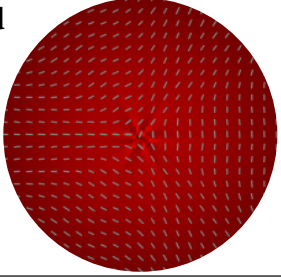
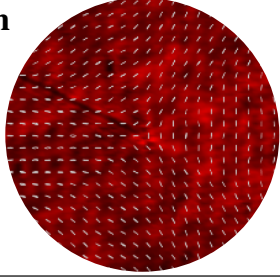


**Figure 4.6:** The intensity patterns of required components of electric field recorded by CCD camera to analyze polarization state of the beam after traveling through the primrose profile 2 SVAP. a) Horizontal, b) vertical, c) anti diagonal, d) diagonal, e) left handed circular, and f) right handed circular polarization components for linear vertical input polarization and tuned SVAP ( $\delta = \pi$ ). As we have linear input the profile of right and left handed polarization components are almost equal and uniform.

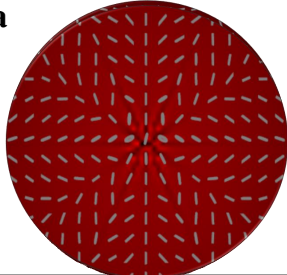
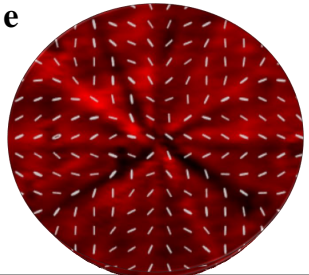
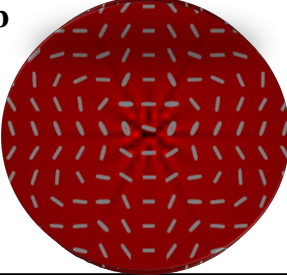
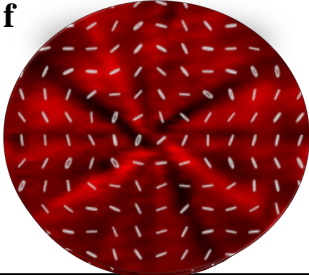
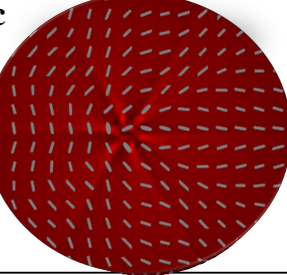
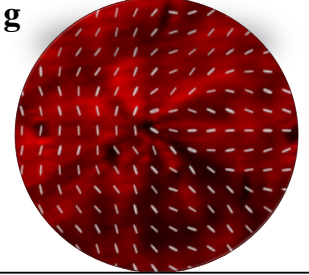
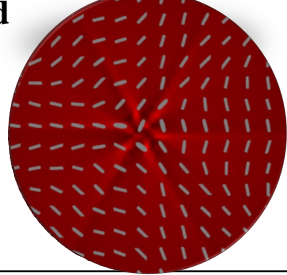
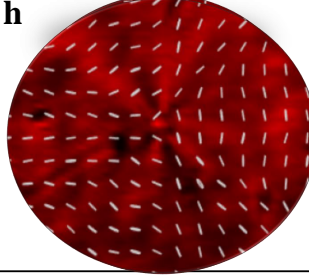


$\delta$	$ p_0\rangle$	HWP <sub>4</sub>	Theoretical predictions	Experimental results
$\pi$	$ H\rangle$	N	<b>a</b>	<b>e</b>
$\pi$	$ V\rangle$	N	<b>b</b>	<b>f</b>
$\frac{\pi}{2}$	$ L\rangle$ $ R\rangle$	N	<b>c</b>	<b>g</b>
$\frac{\pi}{2}$	$ L\rangle$ $ R\rangle$	Y	<b>d</b>	<b>h</b>

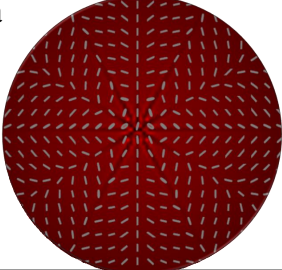
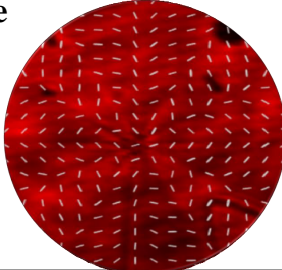
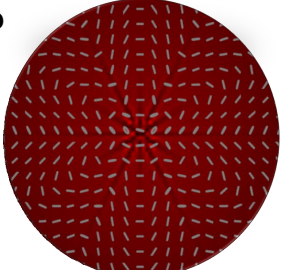
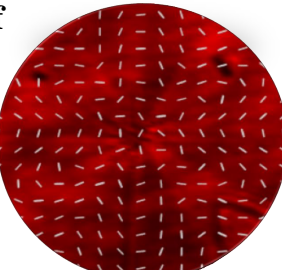
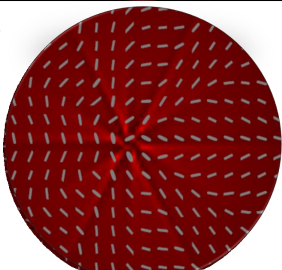
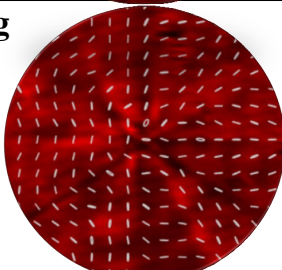
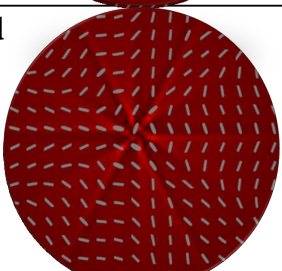
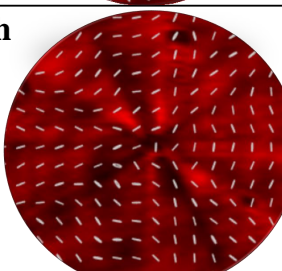
**Figure 4.7:** Near field polarization patterns and transverse intensity distribution of starfish Poincaré Beams. Theoretical predictions and experimental results for different retardation values  $\delta$  and different input polarization states  $|p_0\rangle$ . For each configuration, the presence/absence of HWP<sub>4</sub> is specified with the label Y/N respectively. Axial V-points occur in 1st and 2nd rows (**a**, **e**) and (**b**, **f**), corresponding to predominantly radial and azimuthal patterns respectively. Axial C-points occur in 3rd and 4th rows (**c**, **g**) and (**d**, **h**), corresponding to lemon-like and star-like patterns respectively. Adapted from ref. [103].

$\delta$	$ p_0\rangle$	HWP <sub>4</sub>	Theoretical predictions	Experimental results
$\pi$	$ H\rangle$	N	<b>a</b> 	<b>e</b> 
$\pi$	$ V\rangle$	N	<b>b</b> 	<b>f</b> 
$\frac{\pi}{2}$	$ L\rangle$ $ R\rangle$	N	<b>c</b> 	<b>g</b> 
$\frac{\pi}{2}$	$ L\rangle$ $ R\rangle$	Y	<b>d</b> 	<b>h</b> 

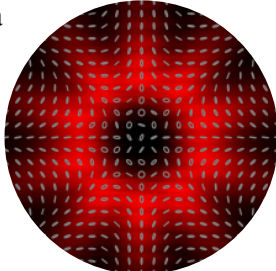
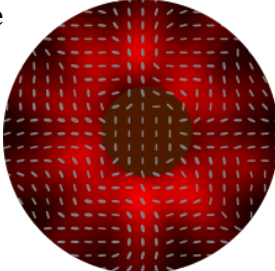
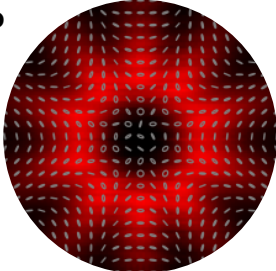
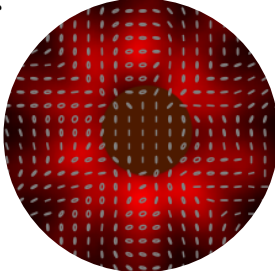
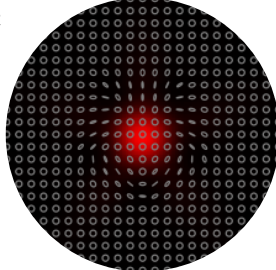
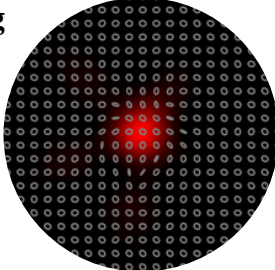
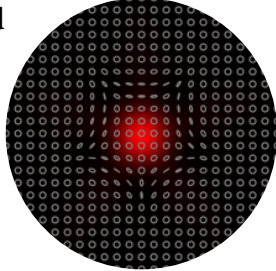
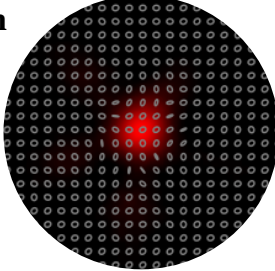
**Figure 4.8:** Near field polarization patterns and transverse intensity distribution of primrose Poincaré Beams. Theoretical predictions and experimental results for different retardation values  $\delta$  and different input polarization states  $|p_0\rangle$ . For each configuration, the presence/absence of HWP<sub>4</sub> is specified with the label Y/N respectively. Axial V-points occur in 1st and 2nd rows (**a**, **e**) and (**b**, **f**), corresponding to predominantly radial and azimuthal patterns respectively. Axial C-points occur in 3rd and 4th rows (**c**, **g**) and (**d**, **h**), corresponding to lemon-like and star-like patterns respectively. Adopted from ref. [103].

$\delta$	$ p_0\rangle$	HWP <sub>4</sub>	Theoretical predictions	Experimental results
$\pi$	$ H\rangle$	N	<b>a</b> 	<b>e</b> 
$\pi$	$ V\rangle$	N	<b>b</b> 	<b>f</b> 
$\frac{\pi}{2}$	$ L\rangle$ $ R\rangle$	N	<b>c</b> 	<b>g</b> 
$\frac{\pi}{2}$	$ L\rangle$ $ R\rangle$	Y	<b>d</b> 	<b>h</b> 

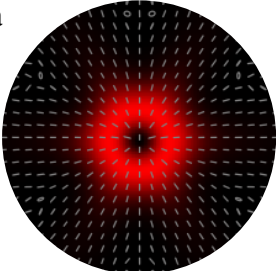
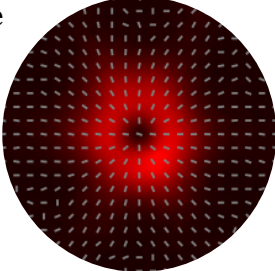
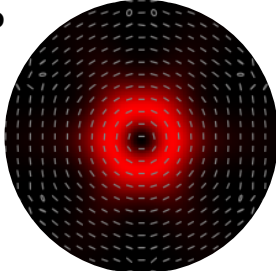
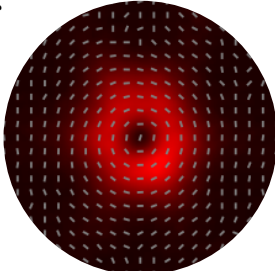
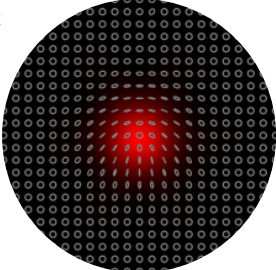
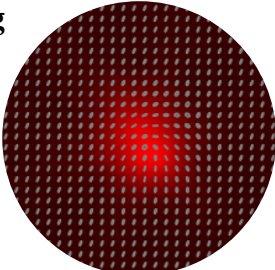
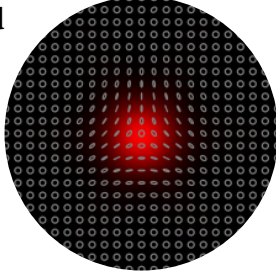
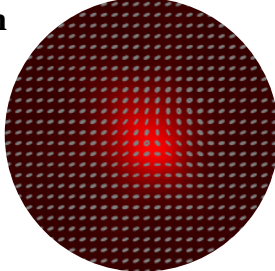
**Figure 4.9:** Near field polarization patterns and transverse intensity distribution of primrose Poincaré Beams profile 2. Theoretical predictions and experimental results for different retardation values  $\delta$  and different input polarization states  $|p_0\rangle$ . For each configuration, the presence/absence of HWP<sub>4</sub> is specified with the label Y/N respectively. Axial V-points occur in 1st and 2nd rows (**a**, **e**) and (**b**, **f**), corresponding to radial and azimuthal patterns respectively. Axial C-points occur in 3rd and 4th rows (**c**, **g**) and (**d**, **h**), corresponding to monstar and star patterns respectively. Interestingly, in this case, we generated monstar which is a rare configuration.

$\delta$	$ p_0\rangle$	HWP <sub>4</sub>	Theoretical predictions	Experimental results
$\pi$	$ H\rangle$	N	<b>a</b> 	<b>e</b> 
$\pi$	$ V\rangle$	N	<b>b</b> 	<b>f</b> 
$\frac{\pi}{2}$	$ L\rangle$ $ R\rangle$	N	<b>c</b> 	<b>g</b> 
$\frac{\pi}{2}$	$ L\rangle$ $ R\rangle$	Y	<b>d</b> 	<b>h</b> 

**Figure 4.10:** Near field polarization patterns and transverse intensity distribution of primrose Poincaré Beams profile 3. Theoretical predictions and experimental results for different retardation values  $\delta$  and different input polarization states  $|p_0\rangle$ . For each configuration, the presence/absence of HWP<sub>4</sub> is specified with the label Y/N respectively. Axial V-points occur in 1st and 2nd rows (**a**, **e**) and (**b**, **f**), corresponding to radial and azimuthal patterns respectively. Axial C-points occur in 3rd and 4th rows (**c**, **g**) and (**d**, **h**), corresponding to monstar and star patterns respectively. Interestingly, in this case, we generated monstar which is a rare configuration.

$\delta$	$ p_0\rangle$	HWP <sub>4</sub>	Theoretical predictions	Experimental results
$\pi$	$ H\rangle$	N	<b>a</b> 	<b>e</b> 
$\pi$	$ V\rangle$	N	<b>b</b> 	<b>f</b> 
$\frac{\pi}{2}$	$ L\rangle$ $ R\rangle$	N	<b>c</b> 	<b>g</b> 
$\frac{\pi}{2}$	$ L\rangle$ $ R\rangle$	Y	<b>d</b> 	<b>h</b> 

**Figure 4.11:** Far field polarization patterns and transverse intensity distribution of starfish Poincaré Beams. Theoretical predictions and experimental results for different retardation values  $\delta$  and different input polarization states  $|p_0\rangle$ . For each configuration, the presence/absence of HWP<sub>4</sub> is specified with the label Y/N respectively. Axial V-points occur in 1st and 2nd rows (**a**, **e**) and (**b**, **f**), corresponding to predominantly radial and azimuthal patterns respectively. Axial C-points occur in 3rd and 4th rows (**c**, **g**) and (**d**, **h**), corresponding to lemon-like and star-like patterns respectively. Adopted from ref. [103].

$\delta$	$ p_0\rangle$	HWP <sub>4</sub>	Theoretical predictions	Experimental results
$\pi$	$ H\rangle$	N	<b>a</b> 	<b>e</b> 
$\pi$	$ V\rangle$	N	<b>b</b> 	<b>f</b> 
$\frac{\pi}{2}$	$ L\rangle$ $ R\rangle$	N	<b>c</b> 	<b>g</b> 
$\frac{\pi}{2}$	$ L\rangle$ $ R\rangle$	Y	<b>d</b> 	<b>h</b> 

**Figure 4.12:** Far field polarization patterns and transverse intensity distribution of primrose Poincaré Beams. Theoretical predictions and experimental results for different retardation values  $\delta$  and different input polarization states  $|p_0\rangle$ . For each configuration, the presence/absence of HWP<sub>4</sub> is specified with the label Y/N respectively. Axial V-points occur in 1st and 2nd rows (**a**, **e**) and (**b**, **f**), corresponding to radial and azimuthal patterns respectively. Axial C-points occur in 3rd and 4th rows (**c**, **g**) and (**d**, **h**), corresponding to lemon and star patterns respectively. Adopted from ref. [103].

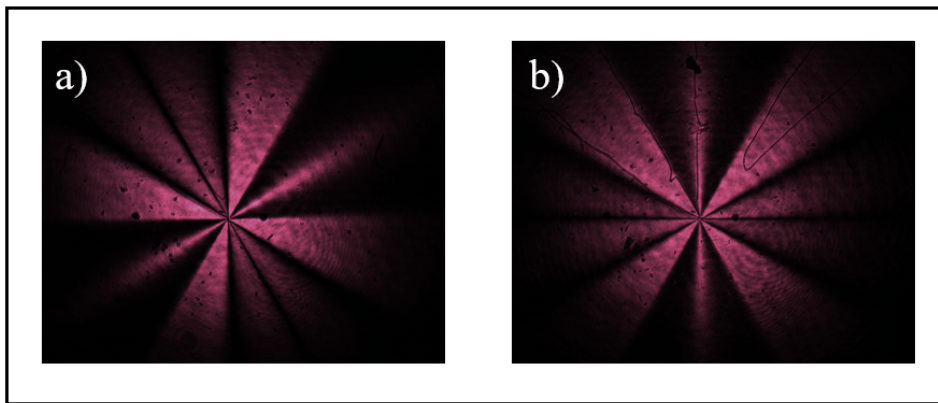


**Figure 4.13:** Experimental measurements for the intensity pattern projected on vertical polarization for azimuthal configuration (linear polarization input with  $\delta = \pi$ ). a) Without two HWPs for the correction, and b) with using two HWPs with proper relative angle. As it can be seen, the whole pattern is rotated when  $\alpha \neq 0$ .

# Conclusion

The capability of controlling the properties of electromagnetic fields leads to advances in industry and science. However, to take advantage of these properties, we need tools and techniques to control and monitor them. Among all, energy and angular momentum attract more attention in both classical and quantum physics. Each form of angular momentum corresponds to a certain degree of freedom and can be used in various applications ranging from light-matter interaction to telecommunications.

In this work, Spatially Varying Axes retardation wave-Plates(SVAPs), which are devices that generalize the q-plate concept have been our main tools to control the interaction of spin angular momentum (SAM) and orbital angular momentum (OAM), thus patterning the vector structure of light. Given the opportunities offered by these tools, we have then theoretically presented an effective way to improve the coupling efficiency in single-mode high contrast nanofibers by amplitude and polarization modification. We proved that we can achieve the highest possible efficiency using this technique. The result can have many applications in quantum and classical regimes. To achieve the goal, we used twisted light generated by a designed q-plate, which is a kind of SVAP, at the fiber facet to match the polarization structure of the input beam to the fundamental mode of the optical fiber  $HE_{11}$ . In addition, we have shown that there can be an optimized input amplitude for scalar mode matching. We have also shown that as the refractive index contrast increases, the polarization matching becomes the dominant effect. It is still interesting and beneficial to apply the same technique to couple light into higher order modes of multi-mode fibers. Moreover, this method can be used to couple waveguide modes



into another waveguide. The same idea can be used for a q-plate spaced from the fiber facet. However, a suitable q-plate must be designed and engineered in each case.

As a second work, we have investigated the use of SVAPs to generate polarization singularities. We have shown that we can generate different classes of polarization singularities with a simple optical setup consisting of a SVAP and a sequence of waveplates. The only parameters that could affect the experiment were the phase retardation of our SVAP and the polarization of the input beam. Thus, we were able to generate both C-point and V-point polarization singularities. All SVAPs used in this experiment were fabricated in our laboratory. The generated beams can be used in many promising applications in the fields of astronomy, microscopy, and biology. Moreover, we envision the possibility to design and develop new SVAPs to generate even more complex structured beams.

In general, the ability to control the angular momentum of light and the spin-orbit coupling using SVAPs and hence the possibility to pattern the vector structure of light at our will play an important role in advancing science and technology in the near future.

# Bibliography

## References

- [1] Alison M Yao and Miles J Padgett. “Orbital angular momentum: origins, behavior and applications”. In: *Advances in Optics and Photonics* 3.2 (2011), pp. 161–204.
- [2] Gabriel Molina-Terriza, Juan P Torres, and Lluís Torner. “Twisted photons”. In: *Nature physics* 3.5 (2007), pp. 305–310.
- [3] John David Jackson. “Classical electrodynamics john wiley & sons”. In: *Inc., New York* 13 (1999).
- [4] Stephen M Barnett. “Optical angular-momentum flux”. In: *Journal of Optics B: Quantum and Semiclassical Optics* 4.2 (2001), S7.
- [5] AT O’neil et al. “Intrinsic and extrinsic nature of the orbital angular momentum of a light beam”. In: *Physical review letters* 88.5 (2002), p. 053601.
- [6] John Henry Poynting. “The wave motion of a revolving shaft, and a suggestion as to the angular momentum in a beam of circularly polarised light”. In: *Proceedings of the Royal Society of London. Series A, Containing Papers of a Mathematical and Physical Character* 82.557 (1909), pp. 560–567.
- [7] Richard A Beth. “Mechanical detection and measurement of the angular momentum of light”. In: *Physical Review* 50.2 (1936), p. 115.

- 
- [8] Les Allen et al. “Orbital angular momentum of light and the transformation of Laguerre-Gaussian laser modes”. In: *Physical review A* 45.11 (1992), p. 8185.
- [9] Miles J Padgett. “Orbital angular momentum 25 years on”. In: *Optics express* 25.10 (2017), pp. 11265–11274.
- [10] P Couillet, L Gil, and F Rocca. “Optical vortices”. In: *Optics Communications* 73.5 (1989), pp. 403–408.
- [11] Ebrahim Karimi. “Generation and manipulation of laser beams carrying orbital angular momentum for classical and quantum information applications”. PhD thesis. Universita degli Studi di Napoli Federico II, 2009.
- [12] Sergei Slussarenko. “Novel tools for manipulating the photon orbital angular momentum and their application to classical and quantum optics”. PhD thesis. Universita degli Studi di Napoli Federico II, 2010.
- [13] Bahaa EA Saleh and Malvin Carl Teich. *Fundamentals of photonics*. John Wiley & sons, 2019.
- [14] L Allen, MJ Padgett, and M Babiker. “IV The orbital angular momentum of light”. In: *Progress in optics* 39 (1999), pp. 291–372.
- [15] MW Beijersbergen et al. “Helical-wavefront laser beams produced with a spiral phaseplate”. In: *Optics communications* 112.5-6 (1994), pp. 321–327.
- [16] Jingbo Sun et al. “Concealing with structured light”. In: *Scientific reports* 4.1 (2014), pp. 1–4.
- [17] V Yu Bazhenov, MV Vasnetsov, and MS Soskin. “Laser beams with screw dislocations in their wavefronts”. In: *Jetp Lett* 52.8 (1990), pp. 429–431.
- [18] Lorenzo Marrucci, Carlo Manzo, and Domenico Paparo. “Optical spin-to-orbital angular momentum conversion in inhomogeneous anisotropic media”. In: *Physical review letters* 96.16 (2006), p. 163905.

- 
- [19] Lorenzo Marrucci, C Manzo, and D Paparo. “Pancharatnam-Berry phase optical elements for wave front shaping in the visible domain: switchable helical mode generation”. In: *Applied Physics Letters* 88.22 (2006), p. 221102.
- [20] Bruno Piccirillo et al. “Photon spin-to-orbital angular momentum conversion via an electrically tunable q-plate”. In: *Applied Physics Letters* 97.24 (2010), p. 241104.
- [21] Jeff Hecht. *City of light: the story of fiber optics*. Oxford University Press on Demand, 2004.
- [22] AJOY AUTOR GHATAK et al. *An introduction to fiber optics*. Cambridge university press, 1998.
- [23] Hiroshi Murata. *Handbook of optical fibers and cables*. Vol. 1. CRC Press, 2020.
- [24] Katsunari Okamoto. *Fundamentals of optical waveguides*. Academic press, 2006.
- [25] Paulo Roriz et al. “Optical fiber temperature sensors and their biomedical applications”. In: *Sensors* 20.7 (2020), p. 2113.
- [26] Abraham Katzir. *Lasers and optical fibers in medicine*. Elsevier, 2012.
- [27] Alexis Mendez. “MEDICAL APPLICATIONS OF FIBER-OPTICS: Optical fiber sees growth as medical sensors”. In: *Laser Focus World* 1.01 (2011).
- [28] Max Epstein. “Fiber optics in medicine.” In: *Critical reviews in biomedical engineering* 7.2 (1982), pp. 79–120.
- [29] Alan Willner. *Optical Fiber Telecommunications*. Vol. 11. Academic Press, 2019.
- [30] B Poumellec and F Kherbouche. “The photorefractive Bragg gratings in the fibers for telecommunications”. In: *Journal de Physique III* 6.12 (1996), pp. 1595–1624.

- [31] Sergi Villalba and Joan R Casas. “Application of optical fiber distributed sensing to health monitoring of concrete structures”. In: *Mechanical Systems and Signal Processing* 39.1-2 (2013), pp. 441–451.
- [32] Alexis Méndez and Ted F Morse. *Specialty optical fibers handbook*. Elsevier, 2011.
- [33] Chai Yeh. *Handbook of fiber optics: Theory and applications*. Academic Press, 2013.
- [34] Allan W Snyder and John Love. *Optical waveguide theory*. Springer Science & Business Media, 2012.
- [35] Iman Soltani and Christopher W Macosko. “Influence of rheology and surface properties on morphology of nanofibers derived from islands-in-the-sea meltblown nonwovens”. In: *Polymer* 145 (2018), pp. 21–30.
- [36] Xianyan Wang et al. “Electrospun nanofibrous membranes for highly sensitive optical sensors”. In: *Nano letters* 2.11 (2002), pp. 1273–1275.
- [37] Kara Peters. “Polymer optical fiber sensors—a review”. In: *Smart materials and structures* 20.1 (2010), p. 013002.
- [38] Pablo Solano et al. “Optical nanofibers: a new platform for quantum optics”. In: *Advances In Atomic, Molecular, and Optical Physics* 66 (2017), pp. 439–505.
- [39] Rajesh Vasita and Dhirendra S Katti. “Nanofibers and their applications in tissue engineering”. In: *International Journal of nanomedicine* 1.1 (2006), p. 15.
- [40] Brigitte Rack et al. “Circulating tumor cells predict survival in early average-to-high risk breast cancer patients”. In: *Journal of the National Cancer Institute* 106.5 (2014), dju066.
- [41] Tarun Garg, Goutam Rath, and Amit K Goyal. “Biomaterials-based nanofiber scaffold: targeted and controlled carrier for cell and drug delivery”. In: *Journal of drug targeting* 23.3 (2015), pp. 202–221.

- [42] Morio Toyoshima. “Maximum fiber coupling efficiency and optimum beam size in the presence of random angular jitter for free-space laser systems and their applications”. In: *JOSA A* 23.9 (2006), pp. 2246–2250.
- [43] S Perumal Sankar, N Hariharan, and R Varatharajan. “A novel method to increase the coupling efficiency of laser to single mode fibre”. In: *Wireless Personal Communications* 87.2 (2016), pp. 419–430.
- [44] Arun Kumar and Ajoy K Ghatak. *Polarization of light with applications in optical fibers*. Vol. 246. SPIE press Bellingham, WA, 2011.
- [45] Jun-ichi Sakai and Tatsuya Kimura. “Birefringence and polarization characteristics of single-mode optical fibers under elastic deformations”. In: *IEEE Journal of Quantum Electronics* 17.6 (1981), pp. 1041–1051.
- [46] David McGloin, Neil B Simpson, and Miles J Padgett. “Transfer of orbital angular momentum from a stressed fiber-optic waveguide to a light beam”. In: *Applied optics* 37.3 (1998), pp. 469–472.
- [47] Henning Soller et al. “HG-LG mode conversion with stressed 3-mode fibers under polarization”. In: *Open J. Appl. Sci.* 2 (2012), pp. 224–227.
- [48] Nenad Bozinovic et al. “Control of orbital angular momentum of light with optical fibers”. In: *Optics letters* 37.13 (2012), pp. 2451–2453.
- [49] Henry P Lee. “Generation of light with orbital angular momentum in optical fiber via acousto-optic interaction”. In: *2006 IEEE Nanotechnology Materials and Devices Conference*. Vol. 1. IEEE. 2006, pp. 246–249.
- [50] Hongwei Zhang et al. “Generation of orbital angular momentum modes using fiber systems”. In: *Applied Sciences* 9.5 (2019), p. 1033.
- [51] Wending Zhang et al. “Cylindrical vector beam generation in fiber with mode selectivity and wavelength tunability over broadband by acoustic flexural wave”. In: *Optics express* 24.10 (2016), pp. 10376–10384.

- [52] JE Midwinter. “The prism-taper coupler for the excitation of single modes in optical transmission fibres”. In: *Optical and Quantum Electronics* 7.4 (1975), pp. 297–303.
- [53] M Kamel Amara and Nouredine Melikechi. “Enhancement of the coupling efficiency in optical fibers using a two-beam optical interference”. In: *Applied physics letters* 80.19 (2002), pp. 3494–3496.
- [54] Monique Thual et al. “Appropriate micro-lens to improve coupling between laser diodes and singlemode fibres”. In: *Electronics letters* 39.21 (2003), pp. 1504–1506.
- [55] G Eisenstein and D Vitello. “Chemically etched conical microlenses for coupling single-mode lasers into single-mode fibers”. In: *Applied Optics* 21.19 (1982), pp. 3470–3474.
- [56] Riccardo Marchetti et al. “High-efficiency grating-couplers: demonstration of a new design strategy”. In: *Scientific reports* 7.1 (2017), pp. 1–8.
- [57] Zhao Qinghua et al. *A Study of End-Fire Coupling of Single-Mode Fiber to TI: LiNbO3 Single-Mode Planar Waveguide*. Tech. rep. NATIONAL AIR INTELLIGENCE CENTER WRIGHT-PATTERSON AFB OH, 1995.
- [58] Sho Chonan, Shinya Kato, and Takao Aoki. “Efficient single-mode photon-coupling device utilizing a nanofiber tip”. In: *Scientific reports* 4.1 (2014), pp. 1–7.
- [59] Yuya Yonezu et al. “Efficient single-photon coupling from a nitrogen-vacancy center embedded in a diamond nanowire utilizing an optical nanofiber”. In: *Scientific reports* 7.1 (2017), pp. 1–9.
- [60] Wenfang Li, Jinjin Du, and Sile Nic Chormaic. “Tailoring a nanofiber for enhanced photon emission and coupling efficiency from single quantum emitters”. In: *Optics letters* 43.8 (2018), pp. 1674–1677.

- 
- [61] Luc B Jeunhomme. *Single-Mode Fiber Optics: Principles and Applications*. Routledge, 2019.
- [62] FE Idachaba, Dike U Ike, and H Orovwode. “Future trends in fiber optics communication”. In: (2014).
- [63] Sophocles J Orfanidis. “Electromagnetic waves and antennas”. In: (2002).
- [64] George B Arfken and Hans J Weber. *Mathematical methods for physicists*. 1999.
- [65] KT Gahagan and GA Jr Swartzlander. “Optical vortex trapping of particles”. In: *Optics Letters* 21.11 (1996), pp. 827–829.
- [66] NR Heckenberg et al. “Trapping microscopic particles with singular beams”. In: *International Conference on Singular Optics*. Vol. 3487. International Society for Optics and Photonics. 1998, pp. 46–53.
- [67] Alan E Willner et al. “Optical communications using orbital angular momentum beams”. In: *Advances in Optics and Photonics* 7.1 (2015), pp. 66–106.
- [68] Nenad Bozinovic et al. “Terabit-scale orbital angular momentum mode division multiplexing in fibers”. In: *science* 340.6140 (2013), pp. 1545–1548.
- [69] D Rozas and GA Swartzlander. “Observed rotational enhancement of nonlinear optical vortices”. In: *Optics letters* 25.2 (2000), pp. 126–128.
- [70] Yijiang Chen and Javid Atai. “Dynamics of optical-vortex solitons in perturbed nonlinear media”. In: *JOSA B* 11.10 (1994), pp. 2000–2003.
- [71] Vincenzo D’ambrosio et al. “Complete experimental toolbox for alignment-free quantum communication”. In: *Nature communications* 3.1 (2012), pp. 1–8.
- [72] Robert Fickler et al. “Quantum entanglement of complex photon polarization patterns in vector beams”. In: *Physical Review A* 89.6 (2014), p. 060301.



- 
- [73] John Frederick Nye. *Natural focusing and fine structure of light: caustics and wave dislocations*. CRC Press, 1999.
- [74] Paramasivam Senthilkumaran. “Singularities in Physics and Engineering”. In: *IOP Publishing* 10 (2018), pp. 978–.
- [75] BS Bhargava Ram, Paramasivam Senthilkumaran, and Anurag Sharma. “Polarization-based spatial filtering for directional and nondirectional edge enhancement using an S-waveplate”. In: *Applied optics* 56.11 (2017), pp. 3171–3178.
- [76] BS Bhargava Ram and Paramasivam Senthilkumaran. “Edge enhancement by negative Poincare–Hopf index filters”. In: *Optics letters* 43.8 (2018), pp. 1830–1833.
- [77] Priyanka Lochab, P Senthilkumaran, and Kedar Khare. “Designer vector beams maintaining a robust intensity profile on propagation through turbulence”. In: *Physical Review A* 98.2 (2018), p. 023831.
- [78] Musheng Chen, Sujuan Huang, and Wei Shao. “Tight focusing of radially polarized circular Airy vortex beams”. In: *Optics Communications* 402 (2017), pp. 672–677.
- [79] B Piccirillo et al. “Electrically tunable vector vortex coronagraphs based on liquid-crystal geometric phase waveplates”. In: *Molecular Crystals and Liquid Crystals* 684.1 (2019), pp. 15–23.
- [80] D Mawet et al. “The vector vortex coronagraph: laboratory results and first light at Palomar observatory”. In: *The Astrophysical Journal* 709.1 (2009), p. 53.
- [81] Bruno Piccirillo, Ester Piedipalumbo, and Enrico Santamato. “Geometric-Phase Waveplates for Free-Form Dark Hollow Beams”. In: *Frontiers in Physics* 8 (2020), p. 94.
- [82] Filippo Cardano et al. “Polarization pattern of vector vortex beams generated by q-plates with different topological charges”. In: *Appl. Opt.*

- 51.10 (Apr. 2012), pp. C1–C6. DOI: [10.1364/AO.51.0000C1](https://doi.org/10.1364/AO.51.0000C1). URL: <http://ao.osa.org/abstract.cfm?URI=ao-51-10-C1>.
- [83] Filippo Cardano et al. “Generation and dynamics of optical beams with polarization singularities”. In: *Opt. Express* 21.7 (Apr. 2013), pp. 8815–8820. DOI: [10.1364/OE.21.008815](https://doi.org/10.1364/OE.21.008815). URL: <http://www.opticsexpress.org/abstract.cfm?URI=oe-21-7-8815>.
- [84] Bruno Piccirillo et al. “The orbital angular momentum of light: Genesis and evolution of the concept and of the associated photonic technology”. In: *La Rivista del Nuovo Cimento* 36.11 (Nov. 2013), pp. 501–555. DOI: [10.1393/ncr/i2013-10094-y](https://doi.org/10.1393/ncr/i2013-10094-y). URL: <https://en.sif.it/journals/sif/ncr/econtents/2013/036/11/article/0>.
- [85] Ben A. Cvorch et al. “Monstar polarization singularities with elliptically-symmetric q-plates”. In: *Opt. Express* 25.13 (June 2017), pp. 14935–14943. DOI: [10.1364/OE.25.014935](https://doi.org/10.1364/OE.25.014935). URL: <http://www.opticsexpress.org/abstract.cfm?URI=oe-25-13-14935>.
- [86] N Justin Marshall. “A unique colour and polarization vision system in mantis shrimps”. In: *Nature* 333.6173 (1988), pp. 557–560.
- [87] Rudiger Wehner. “Astronavigation in insects”. In: *Annual review of entomology* 29.1 (1984), pp. 277–298.
- [88] Thomas W Cronin et al. “Polarization vision and its role in biological signaling”. In: *Integrative and Comparative Biology* 43.4 (2003), pp. 549–558.
- [89] Maki Koike-Tani et al. “Polarized light microscopy in reproductive and developmental biology”. In: *Molecular reproduction and development* 82.7-8 (2015), pp. 548–562.
- [90] Mark R Dennis, Kevin O’Holleran, and Miles J Padgett. “Singular optics: optical vortices and polarization singularities”. In: *Progress in optics* 53 (2009), pp. 293–363.
- [91] Dennis H Goldstein. *Polarized light*. CRC press, 2017.

- 
- [92] David S Kliger and James W Lewis. *Polarized light in optics and spectroscopy*. Elsevier, 2012.
- [93] MS Soskin et al. “Topological charge and angular momentum of light beams carrying optical vortices”. In: *Physical Review A* 56.5 (1997), p. 4064.
- [94] IV Basistiy et al. “Optics of light beams with screw dislocations”. In: *Optics communications* 103.5-6 (1993), pp. 422–428.
- [95] MV Berry and JH Hannay. “Umbilic points on Gaussian random surfaces”. In: *Journal of Physics A: Mathematical and General* 10.11 (1977), p. 1809.
- [96] Sushanta Kumar Pal, P Senthilkumaran, et al. “C-point and V-point singularity lattice formation and index sign conversion methods”. In: *Optics Communications* 393 (2017), pp. 156–168.
- [97] Enrique J Galvez et al. “Poincaré-beam patterns produced by non-separable superpositions of Laguerre–Gauss and polarization modes of light”. In: *Applied optics* 51.15 (2012), pp. 2925–2934.
- [98] Steve C Tidwell, Dennis H Ford, and Wayne D Kimura. “Generating radially polarized beams interferometrically”. In: *Applied Optics* 29.15 (1990), pp. 2234–2239.
- [99] Darrell J Armstrong, Mark C Phillips, and Arlee V Smith. “Generation of radially polarized beams with an image-rotating resonator”. In: *Applied Optics* 42.18 (2003), pp. 3550–3554.
- [100] Tobias Moser et al. “Intracavity generation of radially polarized CO 2 laser beams based on a simple binary dielectric diffraction grating”. In: *Applied optics* 45.33 (2006), pp. 8517–8522.
- [101] Lorenzo Marrucci. “The q-plate and its future”. In: *Journal of Nanophotonics* 7.1 (2013), p. 078598.

- 
- [102] Filippo Cardano. “Engineering spin and orbital angular momentum interactions in a light beam: quantum and classical applications”. PhD thesis. Università degli Studi di Napoli Federico II, 2015.
- [103] Pegah Darvehi et al. “Increasing the topological diversity of light with modulated Poincaré beams”. In: *Journal of Optics* 23.5 (2021), p. 054002.
- [104] Johan Gielis. “A generic geometric transformation that unifies a wide range of natural and abstract shapes”. In: *American journal of botany* 90.3 (2003), pp. 333–338.